

Electronic Thesis and Dissertation Repository

6-24-2020 9:30 AM

Airborne Observations of Thermal Anisotropy from Urban Residential Neighbourhoods in Salt Lake City, Utah

Samantha J. Claessens, *The University of Western Ontario*

Supervisor: Voogt, James A., *The University of Western Ontario*

A thesis submitted in partial fulfillment of the requirements for the Master of Science degree in Geography

© Samantha J. Claessens 2020

Follow this and additional works at: <https://ir.lib.uwo.ca/etd>



Part of the [Environmental Monitoring Commons](#), [Physical and Environmental Geography Commons](#), and the [Remote Sensing Commons](#)

Recommended Citation

Claessens, Samantha J., "Airborne Observations of Thermal Anisotropy from Urban Residential Neighbourhoods in Salt Lake City, Utah" (2020). *Electronic Thesis and Dissertation Repository*. 7091. <https://ir.lib.uwo.ca/etd/7091>

This Dissertation/Thesis is brought to you for free and open access by Scholarship@Western. It has been accepted for inclusion in Electronic Thesis and Dissertation Repository by an authorized administrator of Scholarship@Western. For more information, please contact wlsadmin@uwo.ca.

Abstract

Urban surface temperatures are important variables in urban climatological processes. This thesis examines the directional variability of remotely sensed urban surface temperatures (thermal anisotropy or Λ) for three vegetated residential neighbourhoods in Salt Lake City, Utah, USA. Airborne thermal remote sensing using a thermal imager sampled the directional brightness temperature (DBT) at three times within a day for each site. Results indicate that temporal variability over a 20 – 30-minute flight was not negligible. Average DBT were then extracted from atmospherically corrected images and plotted on polar plots. For low density residential neighbourhoods Λ is increased with increasing tree-canopy coverage (λ_{tree}) due to the increased temperature contrast. The Λ_{Max} for the sites with large λ_{tree} were $\sim 8^{\circ}\text{C}$ compared to $\sim 6^{\circ}\text{C}$ for the site with sparse λ_{tree} . These results indicate Λ for low density residential neighbourhoods is significant and must be considered when discussing land surface temperatures for similar sites.

Keywords

urban, climate, thermal anisotropy, surface temperature, remote sensing, Salt Lake City

Summary for Lay Audience

Land surface temperatures are an important variable for many climatological and hydrological processes. The urban surface, however, is a rough 3-dimensional surface that is comprised of many different surface materials that can be sunlit or shaded. A remote sensing instrument observing this surface can only observe a subset of these surfaces, and as the sensor is moved around the site, it will continue to see a different combination of surfaces and consequently report different averaged surface temperatures. This variability in observed directional surface temperatures is the thermal anisotropy. This thesis examines the thermal anisotropy for residential neighbourhoods in three typical North American neighbourhoods with varying amounts of tree canopy coverage located in Salt Lake City, UT, USA. To sample the thermal anisotropy, airborne thermal remote sensing using a thermal imager was used. Flights were conducted at three times a day for each site. Thermal imagery were corrected for atmospheric effects using MODTRAN6 and atmospheric profile data compiled from a microwave radiometer and radiosondes launched as part of this project. Average temperatures were calculated for each view direction and angle combination for each flight and plotted to illustrate the directional variability of the observed average surface temperature. The temporal variability of surface temperature over a 20 – 30-minute flight was not negligible, and this thesis presents a method of correcting for this variability to minimize impacts on the derived anisotropy. Results indicate that the maximum daytime thermal anisotropy (Δ) of these neighbourhoods' ranges between 6 – 8°C, with the smallest anisotropy observed for the site with lowest tree-canopy coverage. The other two sites had similar tree-canopy coverage and slight differences in building coverage but very similar Δ . This indicates that large amounts of tree canopy coverage create larger thermal anisotropy in low density residential neighbourhoods. It was found that this is likely due to the randomly located cooling effect of the tree canopies causing cooler and larger shaded regions in contrast with the hot surfaces such as sunlit roofs and roads. The large anisotropy of these spatially extensive neighbourhoods is potentially important to the application of satellite-based thermal remote sensing of urban areas.

Co-Authorship Statement

This data used in this thesis was collected as part of a larger observation campaign and as such was produced with the following authorship:

- Samantha J. Claessens: Created flight plans, monitored the instruments in the helicopter traverses and collected in-site data on building and tree height, performed atmospheric corrections, created the methodology used in analysis, performed SUMVeg model iterations, performed analysis with respect to airborne and ground measurements and produced results, text and figures unless otherwise referenced.
- James A. Voogt: Project conceptualization, contribution to development of methodology, edited text and figure presentation.
- Scott Krayenhoff: Contributed in-site ground measurements and LEMS data as well as TUF3D model data.
- Brian Bailey: Contributed in-site ground measurements and LEMS data
- Rainer J. Hilland: Operated the thermal imager, contributed the lens distortion program (Appendix A) and performed the lens vignetting tests (Appendix A).
- Michael A. Allen: Provided ground measurements from vehicle traverses and wall measurements.
- Austine Stastny: Provided ground measurements from vehicle traverses and wall measurements.

Acknowledgments

First, I'd like to thank my supervisor Dr. James Voogt for his guidance and patience through this project. I've learned so much over the past few years so thank you so much for the opportunity.

Thank you to my examination committee Dr. Jinfei Wang, Dr. Jed Long, and Dr. Robert Sica for taking the time to evaluate this thesis.

Thank you to our wonderful lab supervisor Erika Hill, without you we never would have made it to Salt Lake City in the first place! And thank you to the UFEAST research team: Dr. Scott Krayenhoff, Dr. Brian Bailey, Austin Stastny, Michael Allen, and Rainer Hilland for your help with organizing and collecting the data for this project.

I'd also like to thank Lara, Tim and the rest of the geograts for the advice, moral support and afternoons at the grad club. Thank you, Matt, for your help and support and for just being a great friend while I struggled along.

And last, a big thank you to Josh and my parents for the moral support and encouragement through this whole process.

Table of Contents

Abstract.....	ii
Summary for Lay Audience.....	iii
Co-Authorship Statement.....	iv
Acknowledgments.....	v
List of Tables	ix
List of Figures.....	xii
List of Abbreviations and Symbols.....	xxi
Chapter 1	1
1 Introduction.....	1
1.1 Urban Surface Temperatures	1
1.2 Observations of Urban Thermal Anisotropy.....	3
1.3 Thermal Anisotropy of Vegetated Urban Areas	6
1.4 Rationale and Objectives	9
1.5 Thesis Structure	10
Chapter 2.....	11
2 Methods.....	11
2.1 Site Selection and Description.....	11
2.1.1 Geography and Climate of the Salt Lake Metropolitan Area	11
2.1.2 Site Selection	13
2.2 Traverse Methods and Instrumentation	17
2.2.1 Airborne Instrumentation.....	17
2.2.2 Ground-based Instrumentation.....	22
2.3 Data Processing.....	24
2.3.1 Pre-processing.....	24
2.3.2 Atmospheric Corrections	24

2.3.3	Zonal Statistics.....	37
2.4	Summary	44
Chapter 3	45
3	Results and Analysis	45
3.1	Environmental Conditions	45
3.1.1	Incoming Solar Radiation	45
3.1.2	In-canyon Air Temperature.....	47
3.1.3	Wind Speed.....	48
3.2	Descriptive Analysis	50
3.3	Analysis of Temporal Change	52
3.3.1	Temporal Change and Polar Plots.....	53
3.3.2	Model Results	57
3.3.3	Comparison of Repeated Flight Lines	60
3.4	Effective Anisotropy.....	64
3.4.1	Polar plots	64
3.4.2	FLIR T650 vs Heitronics KT15.82 Radiation Pyrometer.....	75
3.4.3	Off-nadir versus Nadir Temperatures	78
3.4.4	Assessment of Remotely Sensed Wall Temperatures.....	82
3.5	Variability within Polar Plots.....	87
3.5.1	Flight Line Comparison and Spatial Variability.....	87
Chapter 4	92
4	Discussion and Conclusion	92
4.1	Urban Anisotropy.....	92
4.2	Land Surface Temperature.....	98
4.3	Critique and Evaluation of the Sampling Method	100
4.4	Summary and Conclusions	106

4.5 Future Work	107
References	110
A Instrument Characteristics and Lab Tests	114
A.1 FLIR T650 Lens errors.....	114
A.1.1 Lens Vignetting.....	114
A.1.2 Optical Lens Distortion.....	115
A.2 Equipment tests	117
A.2.1 Standardization of FLIR T650 and Apogee SIF-1H1	117
A.3 Optimization of FLIR T650 and Heitronics KT15.82 FOV Overlap.....	120
Appendix B	123
B MODTRAN Sensitivity Tests	123
B.1 Surface Temperature	123
B.2 Off-nadir Angle	125
B.3 Sensor Altitude	126
B.4 Humidity.....	128
Appendix C	130
C Supplemental Figures.....	130

List of Tables

Table 2.1 Average site geometries.....	14
Table 2.2 FLIR T650 specifications (FLIR, 2016).....	19
Table 2.3 Heitronics KT15.82 specifications (Heitronics, 2004).....	20
Table 2.4 Flight dates and times. Flight numbers indicate the site acronym and time of flight in local apparent solar time (LAST).	22
Table 2.5 Solar elevation (β) and azimuth (Ω) angles for each flight.....	22
Table 2.6 Truck traverse instrumentation	23
Table 2.7 LEMS instruments.....	24
Table 2.8 Step or bin sizes for MODTRAN input variables.....	28
Table 2.9 Sensitivity test of overlap between atmospheric correction areas and subset IFOV. Correction 1 is the atmospheric correction for the longest path length, Correction 2 is the correction for the center of the FOV, and Correction 3 is the correction for the shortest path length for the sample FOV_{subset} . The bolded scenarios represent the percentage of overlap for each actual FOV_{subset} extracted from each image.	42
Table 3.1 Magnitude of maximum temporal correction applied to each flight. No value indicates a correction was not applied to that flight.	64
Table 3.2 Measures of effective thermal anisotropy for each of the flights. All values in the chart are in ($^{\circ}C$).....	69
Table 3.3 Hot spot characteristics for each polar plot. The solid angle is based on the area subtended by the hot spot on a unit circle.....	69
Table 3.4 Comparison of the FLIR T650 and Heitronics KT15.82 generated polar plots. All values in the chart are in ($^{\circ}C$).	77

Table 3.5 Percent of total wall length obscured from sensor view by a tree canopy or large shrub. Values were calculated from digitized tree-canopy and building plan areas..... 82

Table 3.6 Spatial variability of λ_{tree} and λ_p for the three sites comparing the northeastern, northwestern, southeastern, and southwestern sections of the sites..... 89

Table 4.1 Summary table of site conditions for the sites discussed in Figure 4.1 (Voogt and Oke, 1998; Lagouarde et al., 2004; Lagouarde et al., 2010)..... 97

Table 4.2 Results of differing azimuth and zenith configurations on effective anisotropy for the morning (WS8), solar noon (WS12), and late afternoon (WS17) flights. Bolded rows indicate the results from the complete combination of azimuth and zenith angles and ΔT indicates the difference of the test from these original datasets. 105

Table A.1 Instrument specifications (Heitronics, 2004, FLIR, and Apogee, 2020). 117

Table A.2 Optimization of thermal imager FLIR T650 and Heitronics KT15.82 instrument comparison. FOV1 is the lab tested IFOV_{KT15.82} representing where the Heitronics KT.82 and FLIR T650 overlap. FOV2 – 5 are similarly sized circles moved 50 pixels to the left, right, above, and below the original IFOV_{KT15.82}. FOV6 –increased the size of the IFOV by 5° for location of best match (highest percentage). Percentages represent the percent of polar plot points (ONA and view azimuth pairs) that are considered similar with $p < 0.05$. Each polar plot point is represented by 10 – 80 thermal images. 122

Table B.1 Differences in atmospheric corrections for different bin sizes of ONA. Bin range is expressed as the full range of ONA with the angle as the median of the bin range. Maximum absolute differences in correction are shown for each bin and are expressed as the largest absolute difference in correction between the upper or lower boundary of the bin and the median value. This test is based on a mid-latitude summer atmospheric profile at a given true brightness temperature and sensor altitude. The largest ONA used in the analysis of these observations is 55° ONA, which was sampled at approximately 0.3 km above ground level. The target angles of 45°, 25°, and nadir (5°) are also examined. 126

Table B.2 Differences in atmospheric corrections for different bin sizes of sensor altitude. Bin range is expressed as the full range of altitudes with the angle as the median of the bin

range. Maximum absolute differences in correction are shown for each bin and are expressed as the largest absolute difference in correction between the upper or lower boundary of the bin and the median value. This test is based on a mid-latitude summer atmospheric profile at a given true brightness temperature and sensor ONA. The flights typically ranged from 400 to 800 m above the ground with the transition from a target angle of 45° ONA to 25° ONA occurring at approximately 0.5 km above ground level for most flights..... 127

List of Figures

Figure 1.1 Conceptual image of a remote sensing instrument observing a built surface. The field of view (FOV usually measured as a planar angle through the line-of-sight) of a sensor is controlled by the lens parameters of the sensor (lens diameter (mm) and focal length (mm)) and the radiation source area is the area on the ground (m^2) observed by the sensor which is dependent on the FOV as well as the sensor’s orientation. From Oke et al., (2017)..... 2

Figure 1.2 Model calculated thermal anisotropy (Λ , measured as maximum DBT– minimum DBT) for varying building plan fraction (λ_p) and vegetation cover (λ_v) for June 21 at a 47.6° latitude and a solar zenith angle θ_s of 24.15° . Figure (a) tree height to building height (H_T/BH) is 0.5, (b) tree height to building height is 1.0, and (c) tree height to building height is 1.5. From Dyce and Voogt, (2018). 7

Figure 1.3 Conceptual diagram of a tree canopy shading neighbourhoods with different building density..... 9

Figure 2.1 Map of Salt Lake City Metropolitan area..... 12

Figure 2.2 Climate normal for the period 1981 – 2010 for Salt Lake City. The bar graph represents monthly average precipitation and the line graph represents monthly average maximum and minimum air temperature. Data source: NOAA National Centers for Environmental Information..... 13

Figure 2.3 Map of the Liberty Wells neighbourhood (left) and GoPro image of the site (right). The blue outline on the map indicates the perimeter of the study site. The scissor lift indicated on the map was used to collect atmospheric data above the canopy layer..... 15

Figure 2.4 Map of the White Sands neighbourhood (left) and GoPro image of the site (right). The blue outline on the map indicates the perimeter of the study site. The scissor lift indicated on the map was used to collect atmospheric data above the canopy layer..... 16

Figure 2.5 Map of the Western Springs neighbourhood (left) and GoPro image of the site (right). The blue outline on the map indicates the perimeter of the study site. A scissor lift was not deployed for this site..... 17

Figure 2.6 Photos of (a) the instruments affixed to the operator mount: A is the Heitronics KT15.82 infrared radiometer, B is the FLIR T650 thermal imager, C is the Aaronia GPS Logger, and D is the Go PRO Hero 5 and (b) the operator mount as utilized from the helicopter..... 18

Figure 2.7 Flight plan conceptual diagram. 21

Figure 2.8 Truck mount and instruments. Label A shows the aspirated radiation shield that contains the humidity and air temperature sensors and B indicates the road-facing infrared radiometer. The FLIR T450 thermal imager is not shown but was positioned to view out the driver side rear window. The truck platform also includes incident shortwave, longwave, and PAR radiation sensors, a GoPro camera and a horizontally oriented infrared radiometer. 23

Figure 2.9 Spectral response curves for (a) FLIR T650sc and (b) Heitronics KT15.82 (FLIR, 2016 and Heitronics, 2004)..... 26

Figure 2.10 Relationship between surface temperature and channel radiance in a no-atmosphere simulation for the (a) FLIR T650 thermal imager and (b) Heitronics KT15.82 infrared pyrometer. 27

Figure 2.11 Relationship between MODTRAN input surface temperature and pixel brightness temperature. These plots are sample plots with a sensor orientation of 45° ONA and 1800 m above sea level for (a) FLIR T650 and (b) Heitronics KT15.82. The curve of best fit for each plot is expressed by a 2nd order polynomial for both instruments. Atmospheric correction polynomials are provided as supplemental material..... 28

Figure 2.12 Radiosonde (a) air temperature and (b) dew point profiles for 19 July 2018..... 32

Figure 2.13 Atmospheric profiles for (a) air temperature and (b) dew point. 32

Figure 2.14 Comparison of ground measured surface temperatures to atmospherically corrected DBTs for (a) LW12, (b) LW15, (c) LW17, (d) WhS8, (e) LW12, (f) LW17, (g) WS8, (h) WS10, and (i) WS12. Error bars represent the standard deviation across all sample points. Points represent the mean temperature of sampled points from multiple images. The 1:1 line is indicated. 34

Figure 2.15 Atmospheric corrections for LW12 at an altitude of 1900 m..... 36

Figure 2.16 Thermal image with the five different atmospheric correction zones indicated by red boxes. The uppermost rectangle has the longest path length and thus the correction polynomial yields the largest corrections; the bottom most rectangle has the shortest path length and leads to smaller correction magnitudes (see e.g. Figure 2.16). The observer is East facing at a 45° ONA..... 37

Figure 2.17 Sample thermal image with increasing FOV_{subset}..... 38

Figure 2.18 Boxplot comparison of different FOV_{subset}. Bottom and top of the box represents the first (Q1) and third quartile (Q3) respectively and therefore the range of the box represents the interquartile range (IQR). The line within the box representing the median (Q2). Whiskers represent the minimum and maximum datapoints excluding outliers. Outliers are indicated by points plotted outside of the box and whisker range. 39

Figure 2.19 45° ONA thermal image with 15° FOV_{subset} superimposed on the image. 40

Figure 2.20 Diagram of overlap between atmospheric correction polynomials (grey rectangles) and subset FOV (red circles). Three atmospheric correction areas overlap each subset FOV..... 41

Figure 2.21 Method analysis for LW12 with the observer viewing (a) North, (b) South, (c) East, and (d) West. Points represent averaged DBTs with similar measured angles. The symbols indicate the center angle of the images as measured by the Aaronia GPS Logger and the error bars represent standard deviation between images. 43

Figure 3.1 (a) Incoming solar radiation (K_{\downarrow}) for each study day and (b) the difference in K_{\downarrow} between each study day. Time is in local apparent solar time in hours. K_{\downarrow} values were obtained from the MesoWest University of Utah Mountain (MTMET) station..... 47

Figure 3.2 Air temperature for each study day. Time is in local apparent solar time in hours. Air temperature values were obtained from the MesoWest Salt Lake City Municipal Airport (KU42) station. 48

Figure 3.3 Surface level wind speed for each study day. Time is in local apparent solar time in hours. Wind speed values were obtained from the MesoWest Salt Lake City Municipal Airport (KU42) station..... 50

Figure 3.4 GoPro (a and c) and thermal image (b and d) of the Liberty Wells neighbourhood from a 25° ONA and a (a – b) western and (c – d) eastern view azimuth. 51

Figure 3.5 TUF3D modelled surface temperatures for the White Sands site. WhS8, WhS12, and WhS17 flight times are noted on the graph by the grey bars. Noise in roof surface temperatures are most likely a result of convection..... 53

Figure 3.6 Polar plot of uncorrected directional brightness temperatures for WS17. Temperatures are generated from TUF3D to demonstrate the blurring effect of sampling different angles and view directions at different times. (a) model generated DBT for a single point in time and (b) DBT sampled at different times for different ONAs through the traverse..... 54

Figure 3.7 Solar position for the duration of each flight for (a) Liberty Wells, (b) White Sands, and (c) Western Springs. 55

Figure 3.8 Atmospherically corrected (but temporally uncorrected) polar plots for (a) LW12, (b) LW15, (c) LW17, (d) WhS8, (e) WhS12, (f) WhS17, (g) WS8. (h) WS10, and (i) WS12. 56

Figure 3.9 Modelled changes in directional brightness temperature, $t_1 - t_4$ from the start of the traverse to the end of the traverse for (a) LW12, (b) LW15, (c) LW17, d) WhS8, e) WhS12, (f) WhS17, and $t_1 - t_2$ for (g) WS8, (h) WS10, and (i) WS12. The polar plots were created by calculating at-sensor DBT for 15° FOV using SUMVeg coupled with the urban energy balance model TUF3D to calculate surface component temperatures. Solar position is denoted with a yellow sun symbol..... 60

Figure 3.10 Results from the repeated flight legs for each of Flights (a) LW12, (b) LW15, (c) LW17, (d) WhS8, (e) WhS12, (f) WhS17, (g) WS8, (h) WS10, and (i) WS12. In each plot, directional brightness temperatures are plotted for the flight leg segment at the beginning of

the airborne traverse, at the end of the traverse (repeated flight line) and the correction applied to the repeated section. Box and whiskers configured as in Figure 2.18.	62
Figure 3.11 Sample polar plot depicting the data points as white circles. Observational data were collected for 15° - 55° ONA in 10° bins and 0° - 315° azimuth angles in 45° bins as well as partial coverage of 5° and 65° ONA.....	65
Figure 3.12 Polar plots of temporally corrected observed DBT for a) LW12, (b) LW15, (c) LW17, (d) WhS8, (e) WhS12, (f) WhS17, (g) WS8, (h) WS10, and (i) WS12. The solar position is noted with a yellow sun symbol and the maximum effective anisotropy (Λ_{Max}) is noted for each flight.	66
Figure 3.13 Complete polar plots of (a) LW12, (b) LW15, (c) LW17, (d) WhS8, (e) WhS12, (f) WhS17, (g) WS8, (h) WS10m and (i) WS12. The polar plots include observational data points as well as interpolated nadir points. The solar position is noted with a yellow sun symbol and the maximum effective anisotropy (Λ_{Max}) is noted for each flight.	68
Figure 3.14 Polar plots produced for the FLIR T650 and Heitronics KT15.82 instruments and their differences for (top row) LW12 and bottom row (WhS12). (a) and (d) are FLIR T650, (b) and (e) are Heitronics KT15.82 LW12, (c) and (f) are differences expressed as KT15.82-FLIR T650. Solar position is denoted with a black S.	76
Figure 3.15 Difference in DBT between two overlapping test projected IFOV _{KT15.82} extracted from FLIR imagery. Time is displayed in decimal minutes from the start of the flight line.....	78
Figure 3.16 Difference of off-nadir and nadir temperatures for a) morning flights (WhS8 and WS8) and LW15 along the principal solar plane, b) morning flights and LW15 along the perpendicular solar plane, c) solar noon flights (LW12, WhS12, and WS12) along the principal solar plane, d) solar noon flights along the perpendicular solar plane, e) late afternoon flights (LW17 and WhS17) along the principal solar plane, and f) later afternoon flights along the perpendicular solar plane.	81
Figure 3.17 Sample houses from a) Liberty Wells, b) White Sands and c) Western Springs.	83

Figure 3.18 Opposing wall temperature differences. Temperature differences are expressed as absolute values. The data represented in this plot are a combination of three sampling times for different sites and wall orientations rather than a true time series. 85

Figure 3.19 Polar plots of area averaged temperature standard deviation for (a) LW12, (b) WhS12, and (c) WS12. 88

Figure 3.20 Comparison of DBT from select view azimuths and off-nadir angles for two flight lines separated by 5 minutes. (a) LW12 at a 25° ONA, (b) LW12 at a 45° ONA, (c) WhS12 at a 25° ONA, (d) WhS12 at a 45° ONA, (e) WS12 at a 25° ONA, and (f) WS12 at a 45° ONA. The boxes and whiskers are configured as in Figure 2.18. 90

Figure 4.1 Comparison of Λ_{Max} (constrained to a max ONA of 45°) by tree-canopy plan fraction (λ_{tree}) and building plan fraction (λ_{p}) for 9 mid-latitude neighbourhoods at mid-day: Marseille city center (CC) and Saint Barnabé in France (Lagouarde et al., 2004), Toulouse city center in France (Lagouarde et al., 2010), Vancouver city center (CC), Vancouver light industrial (LI), and Vancouver Residential (R) in Canada (Voogt and Oke, 1998) as well as LW12, WhS12, and WS12. Circle colour indicates the magnitude of thermal anisotropy as indicated by the colour bar. 96

Figure 4.2 Polar plot showing the MODIS viewing angle distributions for Salt Lake City between 8 July and 21 July 2018. 100

Figure 4.3 Polar plots using limited number of data points. The white dots indicate the data points used to create each plot. (a) Complete dataset, (b) test 1, (c) test 2, (d) test 3, (e) test 4, and (f) test 5. 104

Figure A.1 Thermal vignetting of FLIR T650sc thermal images for multiple surface temperatures from the middle of the image to each corner. From Hilland (2018). 115

Figure A.2 Thermal image (left) and photo (right) of the checkerboard used to perform the lens distortion calculations. From Hilland (2018). 116

Figure A.3 Comparison between the Heitronics KT15.81 and FLIR T650sc plate temperature results. The dashed black line represents the 1:1 line. The correlation coefficient for this data is 0.99..... 118

Figure A.4 Comparison between the Apogee SIF-1H1 and FLIR T650sc plate temperature results. The dashed black line represents the 1:1 line. The correlation coefficient for this data is 0.85..... 119

Figure A.5 Sample thermal image from LW12 showing (left) the center points of FOV1 – 5 with FOV1 being the lab determined IFOV_{KT15.82} and (right) FOV6 and FOV7 showing the increase and reduction of FOV3 (the location of best match). 121

Figure B.1 Comparison of atmospheric correction polynomials for increasing step size to a baseline step size of 1°C. The sensor was oriented at a 45° ONA and 0.6 km above ground level. MODTRAN calculated brightness temperature was plotted against input surface temperature (first at 1°C and then at 5°C, 10°C, and 15°C intervals) and a curve of best fit was applied to create correction polynomials for each step size. These were then applied to a range of pixel temperatures and compared to the smallest step size of 1°C, as the smallest step size is expected to produce the most accurate curve. 124

Figure B.2 Change in atmospheric corrections with increasing relative humidity (RH) for the atmospheric profile of 15 July 2018 at solar noon (Flight WhS12). Temperatures used are true brightness temperatures for surfaces such as shaded, irrigated grass (20°C), shaded road or roof (35°C), sunlit road (55°C), and sunlit roof (70°C). 129

Figure C.1 Sunlit roof temperatures extracted from atmospherically corrected helicopter thermal images taken 5-minutes apart for the duration of each flight for (a) LW12, (b)LW15, (c) LW17, (d)WhS8, (e)WhS12, (f)WhS17, (g)WS8, (h)WS10, and (i)WS12. Time uses decimal hours and is in local apparent solar time. Note that the duration of WS8, WS10, and WS12 are about half the length of the other flights. Box and whisker meanings are the same as Figure 2.18..... 130

Figure C.2 Sunlit roof temperatures extracted from atmospherically corrected helicopter thermal images taken 5-minutes apart for the duration of each flight for (a) LW12, (b)LW15,

(c) LW17, (d)WhS8, (e)WhS12, (f)WhS17, (g)WS8, (h)WS10, and (i)WS12. Time uses decimal hours and is in local apparent solar time. Note that the duration of WS8, WS10, and WS12 are about half the length of the other flights. Box and whisker meanings are the same as Figure 2.18..... 131

Figure C.3 Wall temperatures extracted from truck thermal images taken 5-minutes apart for the duration of each flight for (a) LW12, (b)LW15, (c) LW17, (d)WhS8, (e)WhS12, (f)WhS17, (g)WS8, (h)WS10, and (i)WS12. Error bars indicate the standard deviation over the 5-minute averaged temperature. Time is in decimal hours and uses local apparent solar time. Note that the duration of WS8, WS10, and WS12 are about half the length of the other flights. Straight lines between points are used to help visualization and are not indicative of the variability in data between data points..... 132

Figure C.4 Modelled LW12 (a) DBT for start of the traverse (t_1) and the temporal changes in these DBT for (b) $t_1 - t_2$, (c) $t_1 - t_3$, and (d) $t_1 - t_4$ where t_i is the modelled DBT in 15-minute time steps from t_1 to a total of 45-minutes after the start of the traverse (t_4). The location of the sun is indicated by a sun symbol on the polar plot. 133

Figure C.5 Modelled LW15 (a) DBT for start of the traverse (t_1) and the temporal changes in these DBT for (b) $t_1 - t_2$, (c) $t_1 - t_3$, and (d) $t_1 - t_4$ where t_i is the modelled DBT in 15-minute time steps from t_1 to a total of 45-minutes after the start of the traverse (t_4). The location of the sun is indicated by a sun symbol on the polar plot. 134

Figure C.6 Modelled LW17 (a) DBT for start of the traverse (t_1) and the temporal changes in these DBT for (b) $t_1 - t_2$, (c) $t_1 - t_3$, and (d) $t_1 - t_4$ where t_i is the modelled DBT in 15-minute time steps from t_1 to a total of 45-minutes after the start of the traverse (t_4). The location of the sun is indicated by a sun symbol on the polar plot. 135

Figure C.7 Modelled WhS8 (a) DBT for start of the traverse (t_1) and the temporal changes in these DBT for (b) $t_1 - t_2$, (c) $t_1 - t_3$, and (d) $t_1 - t_4$ where t_i is the modelled DBT in 15-minute time steps from t_1 to a total of 45-minutes after the start of the traverse (t_4). The location of the sun is indicated by a sun symbol on the polar plot. 136

Figure C.8 Modelled WhS12 (a) DBT for start of the traverse (t_1) and the temporal changes in these DBT for (b) $t_1 - t_2$, (c) $t_1 - t_3$, and (d) $t_1 - t_4$ where t_i is the modelled DBT in 15-

minute time steps from t_1 to a total of 45-minutes after the start of the traverse (t_4). The location of the sun is indicated by a sun symbol on the polar plot.	137
Figure C.9 Modelled WhS17 (a) DBT for start of the traverse (t_1) and the temporal changes in these DBT for (b) $t_1 - t_2$, (c) $t_1 - t_3$, and (d) $t_1 - t_4$ where t_i is the modelled DBT in 15-minute time steps from t_1 to a total of 45-minutes after the start of the traverse (t_4). The location of the sun is indicated by a sun symbol on the polar plot.	138
Figure C.10 Modelled WS8 (a) DBT for start of the traverse (t_1) and the temporal changes in these DBT for (b) $t_1 - t_2$ where t_2 is the modelled DBT 15-minutes after the start of the traverse. The location of the sun is indicated by a sun symbol on the polar plot.	139
Figure C.11 Modelled WS10 (a) DBT for start of the traverse (t_1) and the temporal changes in these DBT for (b) $t_1 - t_2$ where t_2 is the modelled DBT 15-minutes after the start of the traverse. The location of the sun is indicated by a sun symbol on the polar plot.	139
Figure C.12 Modelled WS12 (a) DBT for start of the traverse (t_1) and the temporal changes in these DBT for (b) $t_1 - t_2$ where t_2 is the modelled DBT 15-minutes after the start of the traverse. The location of the sun is indicated by a sun symbol on the polar plot.	140
Figure C.13 Polar plots using limited number of data points for WhS8. (a) Complete dataset, (b) test 1, (c) test 2, (d) test 3, (e) test 4, and (f) test 5. The number and location of points used for each test are the same as Figure 4.2.	141
Figure C.14 Polar plots using limited number of data points for WhS12. (a) Complete dataset, (b) test 1, (c) test 2, (d) test 3, (e) test 4, and (f) test 5. The number and location of points used for each test are the same as Figure 4.2. Curriculum Vitae	142

List of Abbreviations and Symbols

Abbreviation	Meaning
CSV	Comma-Separated Value
FOV	Field of View
FOV _{subset}	Subset Field of View
GPS	Global Positioning System
IQR	Interquartile Range
IRR	Infrared Radiometer
LCZ	Localized Climate Zone
LAST	Local Apparent Solar Time
NETD	Noise Equivalent Temperature Difference
ONA	Off-Nadir Angle
Q1	First Quartile
Q2	Second Quartile
Q3	Third Quartile
SLC	Salt Lake City
SUM	Surface-Sensor-Sun Model
SUMVeg	Surface-Sensor-Sun Model with Vegetation
TIFF	Tagged Image File Format
TUF3D	Temperatures of Urban Facets in 3D

List of Abbreviations and Symbols

Symbol	Definition	Unit
β	Solar Elevation	°
ε	Emissivity	Unitless (0 - 1)
θ	Sensor Angle from Normal	°
λ	Wavelength	μm
λ_p	Building Plan Fraction	%
λ_{tree}	Tree Canopy Plan Fraction	%
Λ	Anisotropy	°C
Λ_{95-5}	Difference in 95th and 5th percentiles of Directional Brightness Temperatures	°C
Λ_{Max}	Maximum Effective Anisotropy	°C
τ	Atmospheric Transmissivity	Unitless (0 - 1)
Ω	Solar Azimuth	°
$\Omega_{\text{hot spot}}$	Solid Angle of Hot Spot	sr
PAR	Photosynthetically Active Radiation	$\mu\text{m m}^{-2} \text{s}^{-2}$
DBT	Directional Brightness Temperature	°C
RH	Relative Humidity	%
T_{air}	Air Temperature	°C
$T_{B,5}$	5th Percentile of Directional Brightness Temperatures	°C
$T_{B,95}$	95th Percentile of Directional Brightness Temperatures	°C
$T_{B,\text{max}}$	Maximum Directional Brightness Temperature	°C
$T_{B,\text{min}}$	Minimum Directional Brightness Temperature	°C
T_{Road}	Road Brightness Temperature	°C
T_{roof}	Roof Brightness Temperature	°C
T_{wall}	Wall Temperature	°C
W	Radiant Flux	W

Chapter 1

1 Introduction

1.1 Urban Surface Temperatures

Urban environments will continue to grow and expand as the world's population continues to rise. These environments are typically characterized by higher surface and air temperatures compared to their rural surroundings due to the geometry and material properties of the structures within cities. Urban surface and air temperatures are very important in understanding applications like human thermal comfort, building energy use, and modification of micro- and mesoscale meteorological events.

Surface temperature data can be obtained through observations or physically based energy balance models. These models, while cost-effective, require substantial computer resources as well as significant data inputs to characterize the details of the urban surface and of the forcing meteorological conditions. Observations of surface temperatures can be acquired in two main ways: *in situ* measurements and through remote sensing. *In situ* measurements of surface temperature are made by sensors like thermocouples attached to surfaces. Except for very select applications, the use of *in situ* measurements is not feasible for monitoring urban surface temperatures due to the wide variability of surface types and orientations. Remotely sensed surface temperature observations use radiometric based sensors. These can be mounted at a fixed location on the ground or use mobile sensing techniques to give a broader view of the study area from ground, airborne or satellite-based platforms. With the increase in high resolution satellite data availability, remote sensing of urban surface temperatures has become more prevalent.

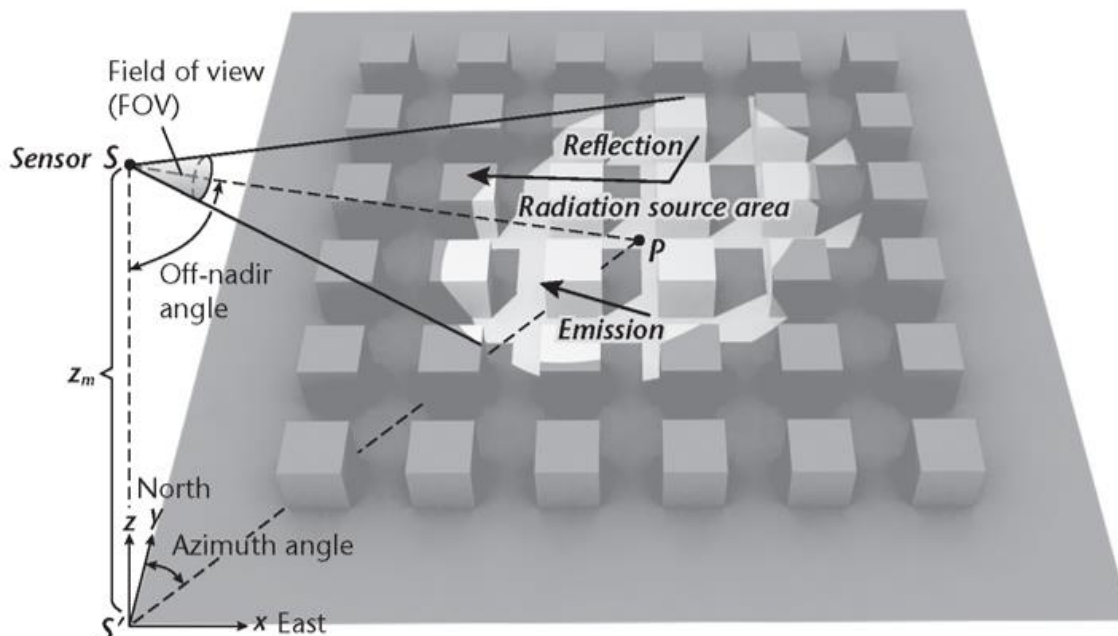


Figure 1.1 Conceptual image of a remote sensing instrument observing a built surface. The field of view (FOV usually measured as a planar angle through the line-of-sight) of a sensor is controlled by the lens parameters of the sensor (lens diameter (mm) and focal length (mm)) and the radiation source area is the area on the ground (m^2) observed by the sensor which is dependent on the FOV as well as the sensor's orientation. From Oke et al., (2017).

The urban surface, however, is a three-dimensional structure composed of many different individual surface facets, each with individual material properties and solar loading. The radiative source area of a remote sensing instrument will only contain a subset of these horizontal and vertical surface facets, and as the sensor is moved around the site, the combination of surfaces observed will change (see Figure 1.1). This contributes to a difference in the observed directional brightness temperature (DBT) measured from the radiation source area of the instrument with view direction, or anisotropy. The range of directional brightness temperatures for an urban site generated by the three-dimensional urban form is referred to as the effective thermal anisotropy (Voogt and Oke, 1998), and is often expressed as:

$$\Delta_{Max} = T_{B,max} - T_{B,min} \quad (1-1)$$

where Λ_{Max} is the maximum thermal anisotropy observed for a site, $T_{B,max}$ is the maximum directional brightness temperature typically observed opposite the solar position for a particular sample time, and $T_{B,min}$ is the minimum directional anisotropy typically observed at large off-nadir angles where maximum shading is observed.

1.2 Observations of Urban Thermal Anisotropy

Anisotropy can be observed in non-lambertian surfaces when the scale of the radiative source area is smaller than the surface being observed. Effective anisotropy, however, is the effect of the structure, rather than an individual surface facet, and is observed when the radiative source area is larger than the 3D structure. At the neighbourhood scale, the surface structure starts to include inhomogeneous structures such as parks which affect the effective anisotropy. This can be observed by ground-based or airborne sampling. At the city scale, different LCZ (localized climate zones) and topography start to influence the effective anisotropy. This is observable with either airborne or satellite scale sampling.

Ground-based Observations

Stationary measurements of spatially and directionally varying surface temperature over agricultural crops have used tower-mounted sensors to measure the directional dependence of temperature of different crop types (Kimes et al., 1986). This is a fine approach for relatively low height crops but has limited applicability in many urban areas because the heights of buildings and trees would necessitate unrealistically tall towers to avoid creating a sampling bias with small radiative source areas associated with the sensor field of view (FOV). This approach was used in a residential urban neighbourhood without significant tree-canopy coverage by Adderley et al. (2015) who found a maximum thermal anisotropy of 3.5K.

Airborne

Airborne sensors can give a broader view of the study area. Lagouarde et al (2004) suggests these provide the best option for surveying the effect of vegetation on thermal anisotropy. Airborne studies of the directional dependence of temperature in densely built areas of cities have been conducted with varying success (Voogt and Oke, 1997; Voogt and Oke, 1998; Lagouarde et al., 2004; and Sugawara and Takamura, 2006). To get an accurate depiction of DBT, multiple view angles (both azimuth angles and sensor off-nadir angles) must be used.

In Iino and Hoyano (1996), Nichol (1998), Voogt and Oke (1998), and Lagouarde et al. (2004) the directional variation in observed DBT measured from an airborne thermal sensor was found to be as large as 10 K over densely built, downtown urban areas with low vegetation coverage. Voogt and Oke (1998) and Lagouarde et al., (2004) included a residential site in their studies and found the thermal anisotropy to be approximately 4K less than the thermal anisotropy of the densely built sites. Each of these studies, however, only looked at one residential neighbourhood.

The challenge to any observational study attempting to characterize the full hemispherical distribution of DBT is to make as many directional measurements in a short enough time frame to minimize changes in solar angle and surface temperatures. Since the urban surface is made of a wide array of different materials, they will heat and cool at different rates which adds a temporal change to anisotropy rather than just a directional component. Voogt and Oke (1997 & 1998) used one thermal infrared camera (TIR) and simply sampled 5 viewing angles — viewing straight down at the ground (nadir) and 45° off-nadir — in the cardinal compass directions. Sugawara and Takamura (2006) employed a similar method but used multiple thermal sensors to achieve more viewing angles. This produces a more complete result than that reported by Voogt & Oke (1998), however utilizing multiple high-resolution sensors comes with a larger expense. Lagouarde et al., (2004) were able to capture more viewing directions by using a wider lens angle and flying at a higher altitude compared to previous studies. This allowed for a very large field of view and radiative source area. In image processing, they took every

pixel representing a specific viewing angle at the same solar angle and integrated over them, creating one temperature for that particular solar angle and view direction (Lagouarde et al., 2004). This approach has the benefit of representing the area from every azimuth angle and a very large portion of off-nadir angles, however, it is computationally intensive and only produces a single temperature value per view angle.

Satellite

Like ground-based and airborne measurements, the use of thermal satellite imagery to assess urban surface temperature is potentially biased due to viewing angle because the sensor “sees” only a portion of the three-dimensional urban surface (Roth et al. 1989). This is of particular concern when observing surface temperatures for rough surfaces such as forests or urban environments. Satellite-based sensors may have either a very narrow range of viewing directions close to nadir, such that they are highly biased to horizontal, unobstructed surfaces (e.g. Landsat); they may view the surface from either a specific off-nadir viewing angle (geostationary satellites) or for a larger range of off-nadir viewing angles but limited azimuthal viewing angles (polar orbiting and cross-track scanning sensors such as MODIS). In all cases the result is a directionally dependent surface temperature, which neglects to give a complete representation of the urban surface temperature (Roth et al., 1989).

Guillevic et al., (2013) and Hu et al., (2016) examined ways to use satellite-based sensors to estimate thermal anisotropy. Guillevic et al. (2013), using MODIS images, observed anisotropy of up to 12 K for two different view angles for a woodland with sparse tree canopies. Geostationary satellite SEVIRI images, with a resolution of 3 km, from a fixed view direction showed the temperature difference between the SEVIRI images and the two MODIS view directions was 8 K (Guillevic et al., 2013). Hu et al., (2016) observed a maximum thermal anisotropy of 9 K for the densely built downtown regions of New York City and Chicago by calculating the thermal anisotropy using 10 years of May-September MODIS imagery and grouping the mean directional temperature values in intervals of every 5 off-nadir angle. This method uses nearby water land surface temperatures to reduce the directional atmospheric attenuation and is therefore heavily

dependent on a large body of water to be relatively near the site to act as a comparator. These temperature differences from different scales and view directions show that the spatial resolution of the satellite thermal imagery still contains important directionally dependent temperature information and demonstrate that the satellite imagery is biased.

1.3 Thermal Anisotropy of Vegetated Urban Areas

Aerial studies of directional dependence of remotely sensed surface temperature over vegetated surfaces were conducted prior to studies in urban environments (e.g. Kimes et al., 1980, Kimes et al., 1986, Luvall, 1990, Kustas 1990, and Lagouarde et al., 2000). Lagouarde et al. (2000) found a 3.8 K difference in surface temperature of a forest when viewed from multiple view direction angles. In the vegetation studies, a large contributor to variations in observed DBT was the difference in temperature between the vegetation and the ground because of the difference in moisture content and heat capacity (Kimes et al., 1980). A similar trend may be expected in urban environments but with perhaps a larger temperature difference due to the heat capacity of urban surface materials. The ground in highly urbanized settings is impervious and dry and may have different radiative properties than soil, causing it to be warmer whereas the temperature of the urban vegetation canopy should be similar to that in a non-urban setting. Residential areas often retain some pervious non-urban cover, however there is less vegetation cover than rural areas and an increase in building cover. These differences may act to increase the thermal anisotropy expected for vegetated urban environments.

Neighbourhoods with significant tree canopy coverage are most often found in residential neighbourhoods. Very few observations of the thermal anisotropy of vegetated urban neighbourhoods exist. From the studies described in Section 1.2, only two urban neighbourhoods with significant tree canopy cover were studied, and that for the Vancouver residential study site reported by Voogt and Oke (1998) had relatively small trees, so there is a lack of information on the extent to which urban tree canopy cover, which is a major component of the three-dimensional urban surface structure, especially in less built residential areas, influences thermal anisotropy.

To better understand how trees affect thermal anisotropy in urban neighbourhoods Dyce and Voogt (2018) developed a sensor view model that, when combined with surface temperature input data, could represent the thermal anisotropy for vegetated urban neighbourhoods. They found (Figure 1.3) the maximum thermal anisotropy in their simulations for neighbourhoods with a plan area coverage of 30% buildings or less and a plan area of 15 – 30% tree canopy with tree height 1.5 times taller than the surrounding buildings. These conditions are typical of open low-rise and sparsely built local climate zones (LCZ) which characterize many North American residential suburb neighbourhoods.

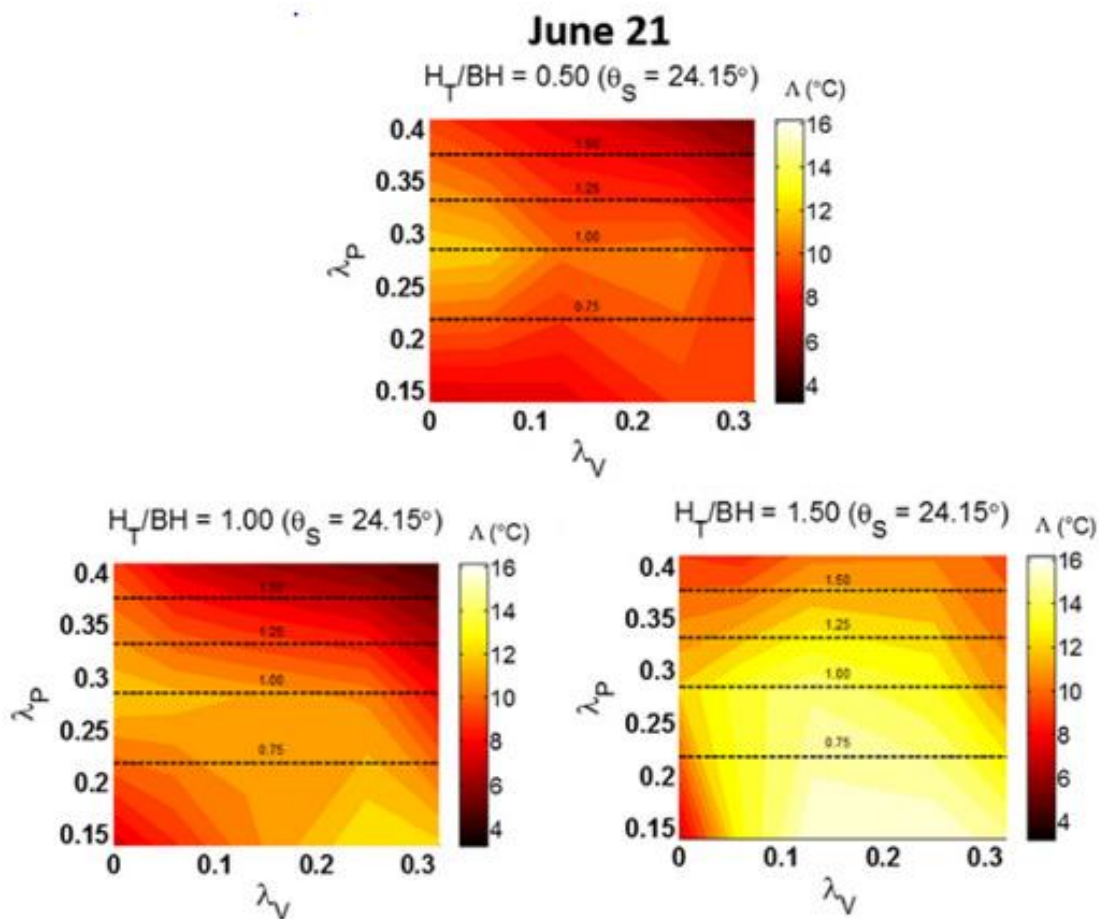


Figure 1.2 Model calculated thermal anisotropy (Λ , measured as maximum DBT–minimum DBT) for varying building plan fraction (λ_P) and vegetation cover (λ_V) for June 21 at a 47.6° latitude and a solar zenith angle θ_S of 24.15° . Figure (a) tree height to building height (H_T/BH) is 0.5, (b) tree height to building height is 1.0, and (c) tree height to building height is 1.5. From Dyce and Voogt, (2018).

The Local Climate Zone classification (Stewart and Oke, 2012), is a way of classifying urban areas based on criteria such as sky view factor, building height to width ratio, building plan fraction, pervious and impervious surface fraction, etc. Both open low-rise (LCZ 6) and sparsely built (LCZ 9) neighbourhoods have small, widely spaced buildings with $< 50\%$ impervious landcover. Open low-rise neighbourhoods are characterized by 1 – 3 storey buildings and a slightly reduced sky view factor (0.6 – 0.9) from street level. The building plan fraction ranges from 20 – 40%, the impervious surface fraction ranges from 20 – 50% and the pervious surface fraction from 30 – 60%. Sparsely built neighbourhoods have similarly sized buildings as open-low-rise, but with less building cover (10 – 20% building plan fraction) and $< 20\%$ impervious surface fraction. The sky view factor for these neighbourhoods is > 0.8 (Stewart and Oke, 2012).

The model results from Dyce & Voogt (2018) shown in Figure 1.2 showed that as the tree cover fraction decreases beyond 15% or increases above 30%, the anisotropy will decrease, with the lowest anisotropy predicted to occur for areas with no trees. As building plan fraction increases above 30%, the expected anisotropy decreases with the largest decreases expected for regions with less than 5% or greater than 25% tree cover. Tree height to building height ratio also impacts expected anisotropy because, as this ratio decreases more of the impervious vertical facets are observed by the sensor and can possibly reduce the overall temperature contrast. The largest anisotropy is expected to be observed at solar noon when the temperature contrast between sunlit surfaces and shaded surfaces is largest. Anisotropy is predicted to be similar for the same solar zenith angles in the morning and afternoon. This increase in anisotropy for vegetated open low-rise and sparsely built neighbourhoods is most likely due to the shading cast by tree canopies in very low-density environments.

Figure 1.3 shows a conceptual diagram of how trees influence the temperature of other surfaces and how these are viewed by a remote sensor. In more densely built neighbourhoods (Figure 1.3a) trees add more shade, reducing the temperature contrast in narrow street canyons by limiting the amount of directly sunlit surfaces, particularly sunlit walls and thereby reducing the thermal anisotropy. In more sparsely built

neighbourhoods (Figure 1.3b), the shade created by the tree canopies increases the temperature contrast and therefore increases the thermal anisotropy.

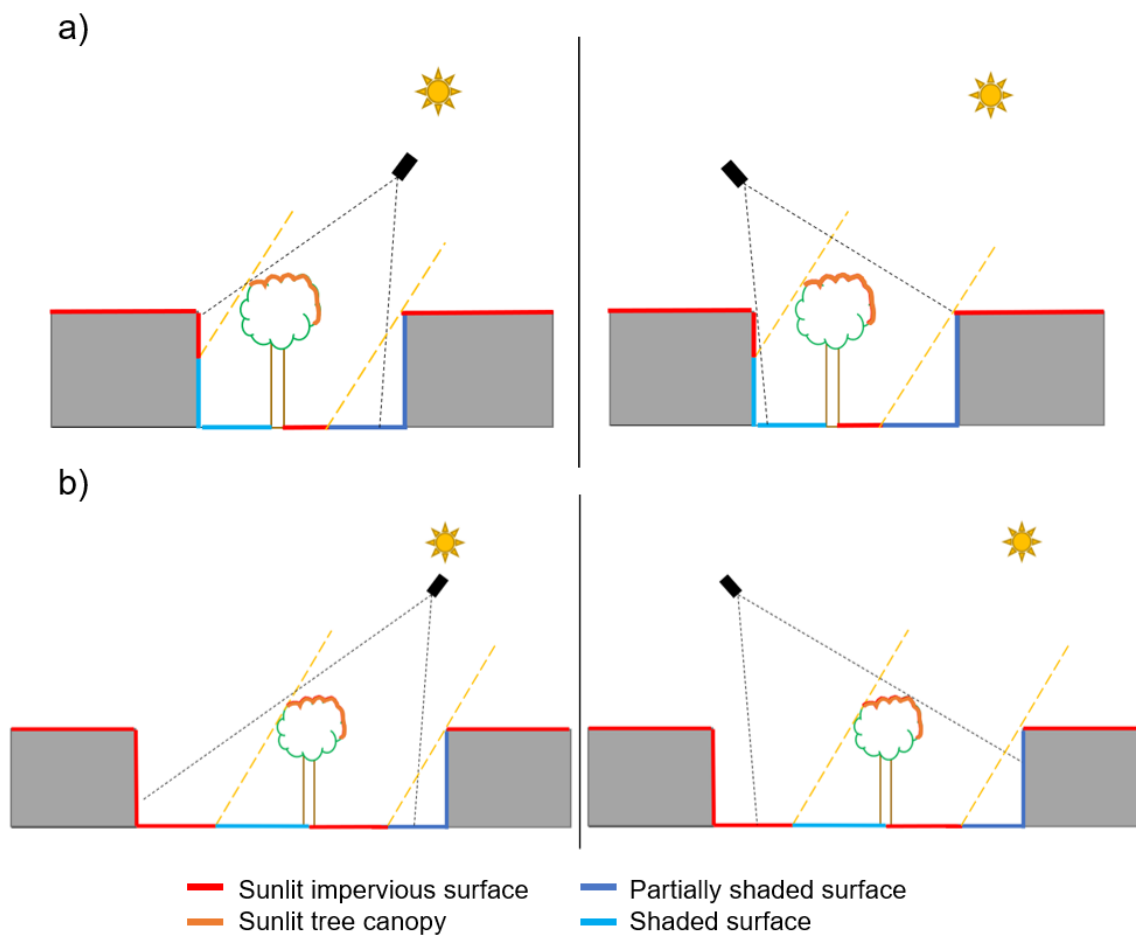


Figure 1.3 Conceptual diagram of a tree canopy shading neighbourhoods with different building density.

1.4 Rationale and Objectives

The directional dependence of remotely observed surface temperature over vegetated surfaces has been studied extensively, however there are only a few studies that look at this effect in the urban environment. Vegetated residential neighbourhoods make up a

large portion of a city's landcover and the results of previous work, both in modelling (Dyce & Voogt 2018) and the limited observations available (Lagouarde et al. 2004; Voogt & Oke 1998), suggest these neighbourhoods can create potentially significant anisotropy. Previous studies were limited in the extent to which the full anisotropy of such neighbourhoods was observed (i.e. the sampling of different view directions) and in the range of tree canopy coverage that is represented. The primary objective of this thesis is to characterize observed thermal effective anisotropy by analyzing a dataset of thermal images obtained over different urban vegetated neighbourhoods under summer season daytime conditions that favour the generation of strong anisotropy. Additionally, we pose a series of research questions based on the dataset obtained.

1. What is the temporal and spatial variation of thermal effective anisotropy in these neighbourhoods and how does this compare to past case studies of urban anisotropy?
2. What is a reasonable time period for sampling the urban surface temperature in order to characterize the effective thermal anisotropy at a particular time?
3. How do the tree canopy plan fractions affect the observed anisotropy within open low-rise / sparsely built neighbourhoods?

1.5 Thesis Structure

This chapter is followed by three further chapters and three appendices. Chapter 2 describes the study sites and methods. Chapter 3 describes the analysis and results of the observations. Finally, Chapter 4 provides a discussion of the work as well as a conclusion to the thesis. Appendix A provides further description and lab testing of some of the instruments involved in the observations. Appendix B provides the results of MODTRAN sensitivity tests related to the atmospheric corrections and Appendix C provides some additional figures supporting Chapter 3.

Chapter 2

2 Methods

2.1 Site Selection and Description

2.1.1 Geography and Climate of the Salt Lake Metropolitan Area

The Salt Lake City metropolitan area, located in the southwestern United States in northern Utah, is centered around Salt Lake City (SLC). It is situated in a valley surrounded by the Wasatch Mountains to the east, the Oquirrh Mountains to the west, and the Traveler Mountains to the south (Figure 2.1). Salt Lake City is at an average elevation of 1288m above sea level. The city is located on the western slope of the Wasatch Mountains and extends into the valley. The highest point within the city is at an elevation of 2868m and the lowest point within the city boundaries is located at 1280m above sea level (NOAA/National Centers for Environmental Information, 2018). The prevailing winds during the summer months are from the South-Southeast.

SLC has four distinct seasons with the summer season generally hot and dry (Figure 2.2) with the warmest, driest month being July (NOAA, 2018). The maximum temperature normal for the month of July is 33.7°C and the minimum temperature normal is 18.2°C. The total precipitation normal for July is 15.49 mm. The Salt Lake City metropolitan area is representative of typical open low-rise and sparsely built neighbourhoods found across North America. The street pattern follows a regular grid pattern, with streets oriented in the cardinal directions. This urban layout provides a good match for current urban energy balance and sensor view model capabilities.

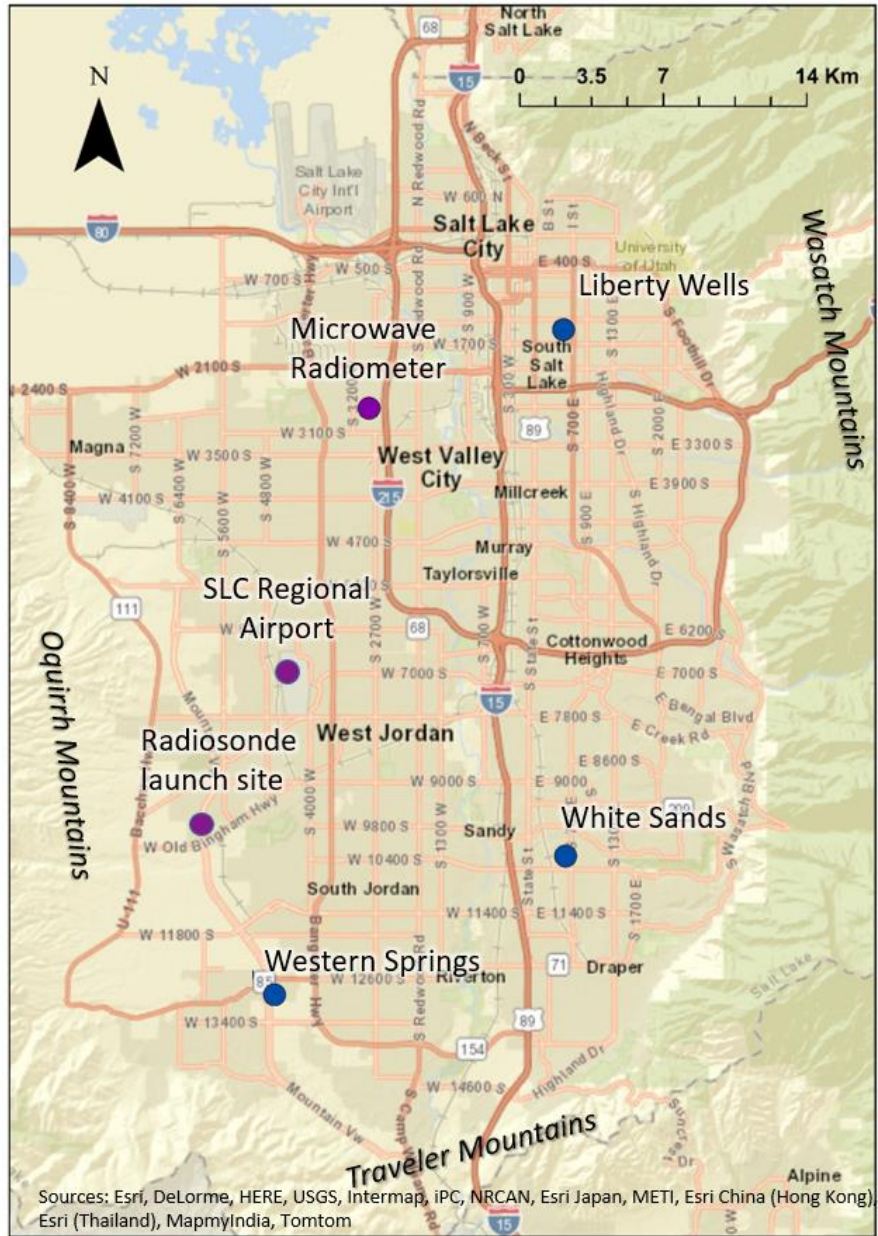


Figure 2.1 Map of Salt Lake City Metropolitan area.

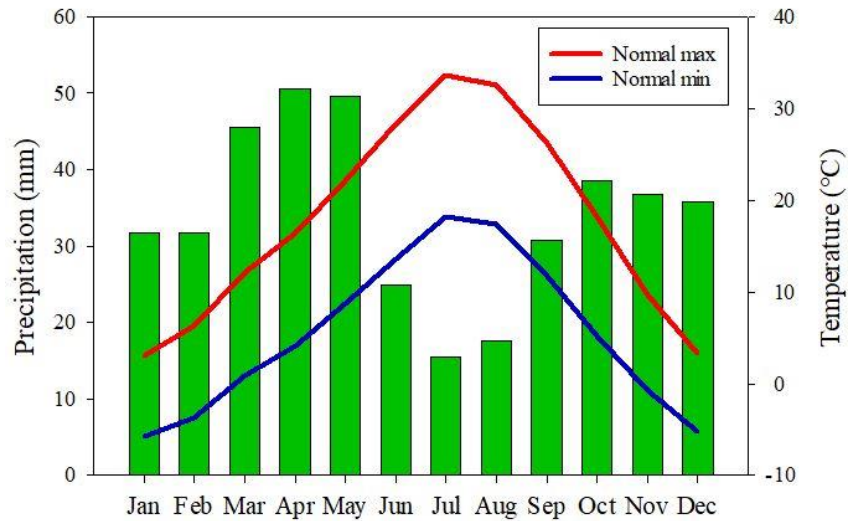


Figure 2.2 Climate normal for the period 1981 – 2010 for Salt Lake City. The bar graph represents monthly average precipitation and the line graph represents monthly average maximum and minimum air temperature. Data source: NOAA National Centers for Environmental Information.

2.1.2 Site Selection

Sites within the Salt Lake City metropolitan area were selected based on building cover (λ_p), tree cover (λ_{tree}), and tree-to-building height ratio (H_{Tree}/BH) as previous work (Dyce and Voogt, 2018) suggested that the combination of these surface cover parameters contributes to changes in anisotropy. Sites were selected with different tree cover to generate differing anisotropy observations of sites typically found in a North American residential neighbourhood. Ideal sites would be characterized by spatially homogenous surface cover and be relatively flat as topography also generates anisotropy. An ideal site was 500 m x 500 m to allow for spatial variations in surface cover and at the same time limit the time needed to sample sufficient view directions and off-nadir angles to characterize the hemispherical anisotropy of the site. Ideally, sites would have well irrigated lawns to ensure the maximum temperature differences between built and vegetated surface cover. Building and tree cover were evaluated for potential sites by digitizing sample regions extracted from Google Earth imagery and calculating the fraction of area covered by buildings and tree canopies. Tree-to-building height was

assessed qualitatively through Google Earth to assess if the trees were on-average larger, smaller, or of similar height to the buildings. For more exact measurements, in-site measurements of sample buildings and trees were estimated using angle measurements from inclinometers. Table 2.1 shows a summary of the site geometries.

Table 2.1 Average site geometries.

	Liberty Wells	White Sands	Western Springs
λ_p (%)	19 - 25	15 - 17	22 - 24
λ_{tree} (%)	19 - 22	17 - 23	2 - 8
H_T/BH	1.5	1.5	1
Building spacing (m)	5 - 10	6 - 8	3 - 5
Front yard (m)	14 - 16	12 - 14	5 - 13
Backyard (m)	8 - 12	10 - 12	10 - 13
Street Width (m)	9 - 12	7 - 8	7 - 11

Liberty Wells

Liberty Wells (40°44'18.14"N, 111°52'32.36"W) is a neighbourhood in the northwest part of Salt Lake City close to the Wasatch Mountain range. The study area is outlined in blue on the map provided in Figure 2.3. It has an average elevation of 1300 m above sea level which varies by +/- 2m across the site, with the lowest areas in the northwest part of the site and the highest elevation found in the southeast. This site consists of single storey or storey and a half houses with detached garages. The study site is located just south of a large park. The area in the park closest to the study site contains a large pond with large grasses along the shore as well as large, mature trees bordering the park and surrounding the pond. Thermal images containing the park were removed to better represent a more general neighbourhood. The pond in the park was useful in acting as a calibration source area for atmospheric corrections performed as the thermal properties of water make it appear cool and highly visible to a thermal imager. The prevailing winds for this site

under warm, clear summer conditions are from the south-southeast, meaning the park did not influence the thermal characteristics of the study site.

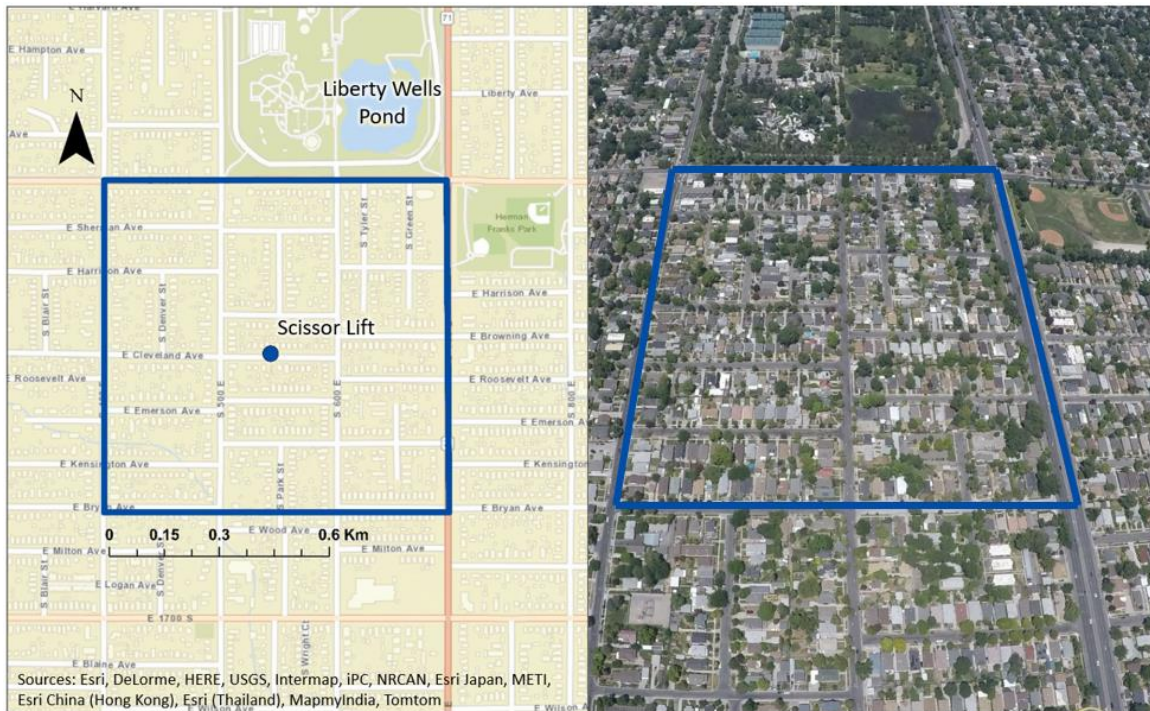


Figure 2.3 Map of the Liberty Wells neighbourhood (left) and GoPro image of the site (right). The blue outline on the map indicates the perimeter of the study site. The scissor lift indicated on the map was used to collect atmospheric data above the canopy layer.

White Sands

White Sands (40°33'48.42"N, 111°52'28.22"W) is a neighbourhood in Sandy, Utah to the south of Salt Lake City with an elevation of 1375 m above sea level that varies from 1376 – 1373m in the north-south directions and from 1370 – 1381 m in the east-west direction when assessing Google Earth elevation profiles. The study area is indicated by the blue square on the map in Figure 2.4. Table 2.1 shows that White Sands has a lower building cover fraction than Liberty Wells and is mostly comprised of single storey or raised ranch style houses. A large sports park is located to the north of White Sands with

large, well irrigated grass areas and some larger, mature trees along the perimeter of the park.

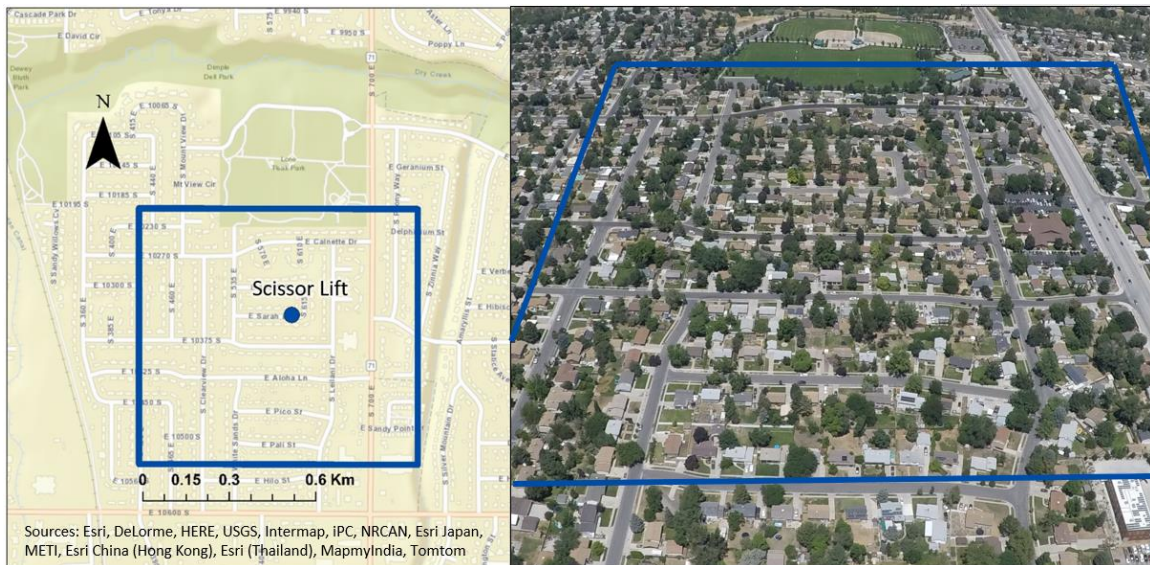


Figure 2.4 Map of the White Sands neighbourhood (left) and GoPro image of the site (right). The blue outline on the map indicates the perimeter of the study site. The scissor lift indicated on the map was used to collect atmospheric data above the canopy layer.

Western Springs

Western Springs (40°31'2.56"N, 112°0'8.7"W) is located in the southwestern portion of the valley, just north of the Traveler Mountains. It has an average elevation of 1447 m above sea level with a range of elevation from 1443 m to 1451 m from east to west. The site is a relatively new development with young trees. The site contains a mix of one- and two-storey houses and is surrounded by a highway to the west and undeveloped land all around the site. As Table 2.1 indicates, the trees in the Western Springs neighbourhood are much smaller than the other two sites, with a building-to-tree height ratio of approximately 1. The study site is shown in Figure 2.5.



Figure 2.5 Map of the Western Springs neighbourhood (left) and GoPro image of the site (right). The blue outline on the map indicates the perimeter of the study site. A scissor lift was not deployed for this site.

2.2 Traverse Methods and Instrumentation

2.2.1 Airborne Instrumentation

The airborne sampling used four instruments. All four instruments were affixed to a white platform equipped with a radiation shield that was worn, using a shoulder-harness system, by a human operator who manually oriented the system to view the ground at a select off-nadir angle. A moveable mount was used as opposed to a fixed mount so that multiple off-nadir angles could be sampled within the same flight. Figure 2.6 shows the mounted instruments.



Figure 2.6 Photos of (a) the instruments affixed to the operator mount: A is the Heitronics KT15.82 infrared radiometer, B is the FLIR T650 thermal imager, C is the Aaronia GPS Logger, and D is the Go PRO Hero 5 and (b) the operator mount as utilized from the helicopter.

Two different thermal sensors were used during each traverse, the FLIR T650sc and a Heitronics KT15.82 Radiation Pyrometer. These instruments were mounted to the helicopter instrument mount such that the FOV of both instruments overlapped. Analysis of this overlap can be found in Appendix A. The FLIR thermal imager (Table 2.2) provided a 640 x 480 array of temperatures over the 45 x 34° FOV set to sample at 2 Hz. Flight lines were setup such that a pixel represented approximately 1m² or less on the ground. These images can be analyzed pixel by pixel, or by averaging over a select area on the images. The Heitronics instrument is a non-imaging instrument that provides a single temperature for the entire FOV and provides a second independent sample of DBT. This instrument provides an independent measurement that can allow verification of sensor view models such as SUM (Soux et al., 2004) or SUMveg (Dyce and Voogt, 2018) that use data from the FLIR imagery as inputs. Previous model evaluations have been limited by validating the model output with the data used to initiate the model (Voogt, 2008). Instrument specifications of the Heitronics instrument are found in Table

2.3. The field of view (FOV) of this instrument was given as a relationship between distance from target and view diameter. To calculate an approximate FOV for this instrument equation 2.1 was used, where d is the diameter of the lens (20 mm) and f is the focal length (95 mm).

$$FOV(^{\circ}) = 2 \left(\tan^{-1} \left(\frac{d}{2f} \right) \right) \quad (2.1)$$

The response time of this instrument is selectable and was set to 100 ms to provide accurate data from a moving platform. The radiative source area of the instrument was approximately 0.05 km².

Table 2.2 FLIR T650 specifications (FLIR, 2016).

Parameter	
Detector Type	Uncooled Microbolometer
Spectral Range	7.5 - 14 μ m
Temperature range	-40 $^{\circ}$ C to 70 $^{\circ}$ C
Accuracy	± 1 $^{\circ}$ C
Resolution	640 x 480 px
FOV	45 $^{\circ}$ x 34 $^{\circ}$
Focal Length	13.1 mm
Frame Rate	30 Hz
Time Constant	< 8ms
NETD *	< 20 mK

* Noise equivalent temperature difference, or how sensitive the imager is to detecting small differences in radiation within the FOV

Table 2.3 Heitronics KT15.82 specifications (Heitronics, 2004).

Parameter	
Spectral Range	8 - 14 μm
Calibration Range	-30 $^{\circ}\text{C}$ to 70 $^{\circ}\text{C}$
Accuracy	± 0.5 $^{\circ}\text{C}$
Focal Length	50 mm
FOV	$\approx 12^{\circ}$
Response Time	100 ms
Voltage Range	0 to 10V

A GoPro Hero 5 was added to the imager mount to provide photographs of the imaged areas. This permits identification of surface cover and structures independent of the thermal imager. An Aaronia GPS Logger that records GPS data as well as the tilt, roll, and height of the logger was attached to the helicopter thermal imager mount. This allows the orientation of the thermal imager to be determined independently. The Aaronia GPS Logger attached to the imager mount was oriented so as to allow the tilt with respect to the horizon of the thermal sensors and GoPro to be recorded. The GPS Logger data were live streamed to a computer in the helicopter allowing the orientation of the thermal sensors to be monitored in real time.

Airborne Traverse Design

For each study site, an airborne flight plan was constructed to sample the directional radiometric temperature in 8 view directions for 2 off-nadir angles (25° and 45°) as well as from nadir. The plan was designed to provide sufficient spatial sampling to characterize the spatial variability of the directional radiometric temperature for the study site and still be completed in 30 minutes or less, to minimize changes in surface temperature over time. The flight route of the helicopter was planned as a square pattern around each study site, flown in the counterclockwise direction with the imager mount pointed in, toward the site. Three separate flight heights of 300 m, 450 m, and 600 m above ground level were flown, one for each target angle. This combination of flight

height and sensor off-nadir angle yield images that are approximately 0.3 km^2 with a pixel resolution of approximately 1 m^2 . Four loops were made around the sites at each height; two loops were made with flight lines oriented in the cardinal directions and two with the square pattern rotated by 45° to allow sampling of the inter-cardinal directions (see Figure 2.7 for conceptual diagram). This ensured full coverage of the site for each of the N, S, E, W and NE, NW, SE, and SW view directions within the time limits of the flight. An additional loop was made around each site at the end of the traverse resampling at the same height, off-nadir angle (ONA) and view directions as the initial flight loop at the beginning of the traverse. This repeated flight line was used to analyze changes in DBT over the duration of the flight. The helicopter flew with a groundspeed of approximately 50 knots which allowed for approximately 97% overlap of images at that sample rate. Three flights were flown per site over the course of three days (see Table 2.4). Traverse times were chosen such that target solar zenith angles of 50° , 20° , and 70° could be sampled. Table 2.5 shows the actual angles sampled for each flight.

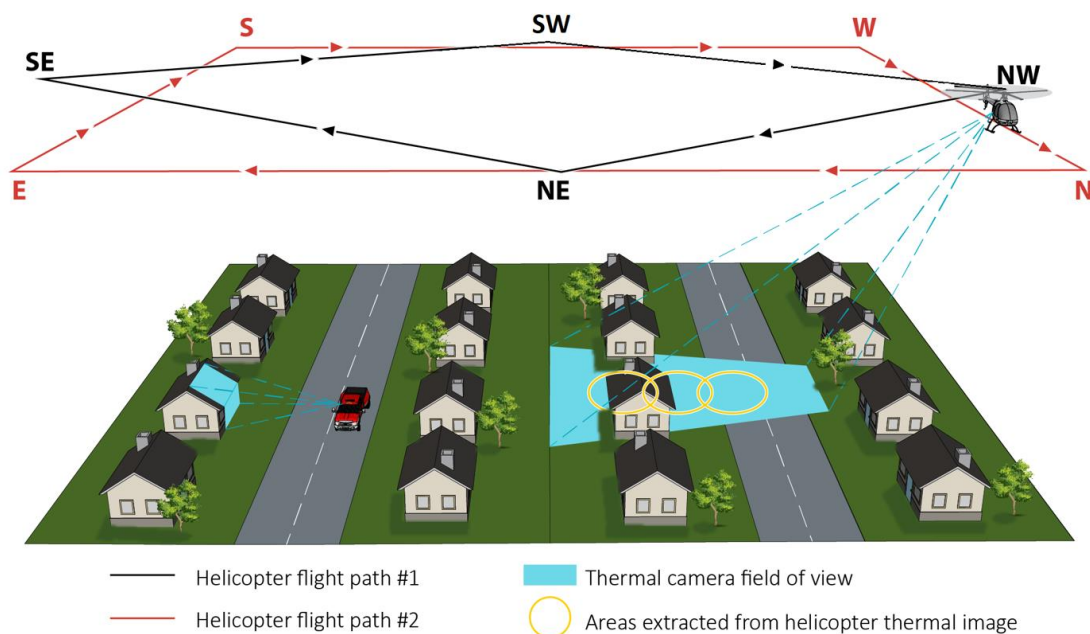


Figure 2.7 Flight plan conceptual diagram.

Table 2.4 Flight dates and times. Flight numbers indicate the site acronym and time of flight in local apparent solar time (LAST).

Site	Flight Number	Start Time (LAST)	End Time (LAST)	Duration
Liberty Wells	LW12	12:06:00	12:41:59	00:35:59
	LW15	14:53:52	15:29:21	00:35:29
	LW17	16:59:47	17:46:54	00:47:07
White Sands	WhS8	08:00:48	08:38:20	00:37:32
	WhS12	11:58:10	12:32:18	00:34:08
	WhS17	17:00:54	17:41:13	00:40:19
Western Springs	WS8	08:18:57	08:39:13	00:20:16
	WS10	10:33:48	10:52:00	00:18:12
	WS12	11:58:19	12:16:30	00:18:11

Table 2.5 Solar elevation (β) and azimuth (Ω) angles for each flight.

Site	β - Start of Traverse	β - End of Traverse	$\Delta\beta$	$ \Omega$ - Start of Traverse	Ω - End of Traverse	$\Delta\Omega$
LW12	71.06	69.42	1.64	174.81	206.36	31.55
LW15	49.49	42.9	6.59	255.41	262.55	7.14
LW17	25.84	17.1	8.74	277.42	284.45	7.03
WhS8	35.75	42.82	7.07	91.44	98.07	6.63
WhS12	70.63	69.73	0.9	176.2	199.62	23.42
WhS17	25.42	17.93	7.49	277.12	283.18	6.06
WS8	38.71	42.51	3.8	95.21	98.92	3.71
WS10	62.33	64.83	2.5	129.54	137.29	7.75
WS12	69.94	69.8	0.14	176.19	188.55	12.36

2.2.2 Ground-based Instrumentation

Simultaneously to the aerial traverses, ground-based measurements were acquired. A pickup truck was outfitted with a rack where instruments were mounted to provide in-canyon data to accompany the aerial dataset (shown in Figure 2.8). An infrared radiometer sampled road temperatures while a relative humidity sensor and fine wire thermistor sampled in-canyon air temperature and humidity. A thermal imager was also placed in the truck and positioned in such a way that it could sample wall temperatures on

one side of the truck. Table 2.6 provides details on the truck instrumentation. Surface temperature observations were used to validate the atmospheric corrections discussed in section 2.3.3. In-canyon fixed stations provided by the University of Utah (LEMS stations) were setup within the Liberty Wells and White Sands sites to collect data on incoming solar radiation ($K\downarrow$), air temperature, and surface temperatures (see Table 2.7).



Figure 2.8 Truck mount and instruments. Label A shows the aspirated radiation shield that contains the humidity and air temperature sensors and B indicates the road-facing infrared radiometer. The FLIR T450 thermal imager is not shown but was positioned to view out the driver side rear window. The truck platform also includes incident shortwave, longwave, and PAR radiation sensors, a GoPro camera and a horizontally oriented infrared radiometer.

Table 2.6 Truck traverse instrumentation

Manufacturer	Instrument	Variable
Apogee	SIF-1H1 Infrared Radiometer	T_{Road} ($^{\circ}\text{C}$)
	ST-200 Fine wire Thermistor	T_{air} ($^{\circ}\text{C}$)
Campbell Scientific	HC-S3 Probe	T_{air} ($^{\circ}\text{C}$), RH(%)
FLIR	T450sc Thermal Imager	T_{wall} ($^{\circ}\text{C}$)

Table 2.7 LEMS instruments.

Manufacturer	Instrument	Variable
Li-Cor	Li-200R	K_{\downarrow} (Wm^{-2})
Sensirion	Adafruit SHT31	T_{air} ($^{\circ}C$)
ACROBOTIC	MLX90614	T_{Ground} ($^{\circ}C$)

2.3 Data Processing

2.3.1 Pre-processing

The airborne thermal imagery was recorded using software provided by the manufacturer to a sequence file format (.seq) on a laptop computer. The sequence file records images that can then be played back as a video using proprietary software. These recordings were then exported frame-by-frame into CSV files. These files represent the pixels from the thermal imagery as an array of observed brightness temperatures in $^{\circ}C$. Corrections were performed for lens distortion using Matlab (see Appendix A) and then the images were converted into raster tiff files before further processing.

Images showing areas outside of the study areas or large fields and bodies of water were removed from the dataset. In some cases, portions of images were removed in later stages of data processing that contained field or water.

2.3.2 Atmospheric Corrections

Remotely sensed temperatures must take into account the effect of the absorptivity and transmissivity of thermal radiation by the atmosphere on the observed surface temperatures. Thermal sensors are typically designed to operate over a spectral range within the atmospheric window region – limiting but not eliminating atmospheric interference in the sensed temperature. This atmospheric affect is dependent on the path length through the atmosphere between the sensor and the source which is dictated by the

height of the sensor (h) and the angle of the sensor from normal (θ) as well as the wavelength (λ). Atmospheric corrections are performed on remotely sensed temperatures due to this influence using a single-channel method expressed by Byrnes and Schott (1986) as,

$$W(h, \theta, \lambda) = \tau(h, \theta, \lambda) \cdot \varepsilon(\lambda) \cdot W_G + \tau(h, \theta, \lambda) \cdot (1 - \varepsilon(\lambda)) \cdot W_{sky} + W_a \quad (2.2)$$

where $\tau(h, \theta, \lambda)$ is the atmospheric-path transmission to the sensor for a given sensor height and angle from the normal, ε is the emissivity of the surface, W_G is the upwelling radiance from the ground, W_{sky} is the incoming radiance to the surface from the hemispherical sky, and W_a is the radiance emitted from the atmosphere between the sensor and the ground. A single pixel can contain multiple surfaces with emissivities in the range of 0.8 – 0.99. Using an emissivity of 1 simplifies the atmospheric correction process and as anisotropy is calculated as the difference in directional temperatures over the same area, an emissivity of 1 can be used. A temperature associated with an emissivity of 1 was termed by Norman et al. (1995) as a DBT. Equation 2.2 then becomes,

$$W(h, \theta, \lambda) = \tau(h, \theta, \lambda) \cdot W_G + W_a \quad (2.3).$$

Sensors are responsive over a specific spectral band so equation 2.3 must be integrated over the spectral curve of the specific instrument.

$$W(h, \theta) = \int_{\lambda_1}^{\lambda_2} W(\lambda, h, \theta) d\lambda \quad (2.4)$$

A single channel method using version 6 of the MODTRAN (Berk et al., 1987), moderate resolution atmospheric transmission program, a radiative transfer program, was used to generate corrections for the thermal data used. To perform the corrections, MODTRAN 6 was run with the combination of input variables (surface temperature, off-nadir angle, and height) that corresponded to the flight configuration. To determine the magnitude of correction, a “no-atmosphere” lookup was created for both the FLIR thermal imager and Heitronics KT15.82 infrared pyrometer by integrating the Planck function over the spectral response curve of each instrument (Figure 2.9) for a range of surface

temperatures. This “no-atmosphere” lookup table establishes the relationship between surface temperature and observed radiation without atmospheric effects. The “no-atmosphere” lookup is shown in Figure 2.10.

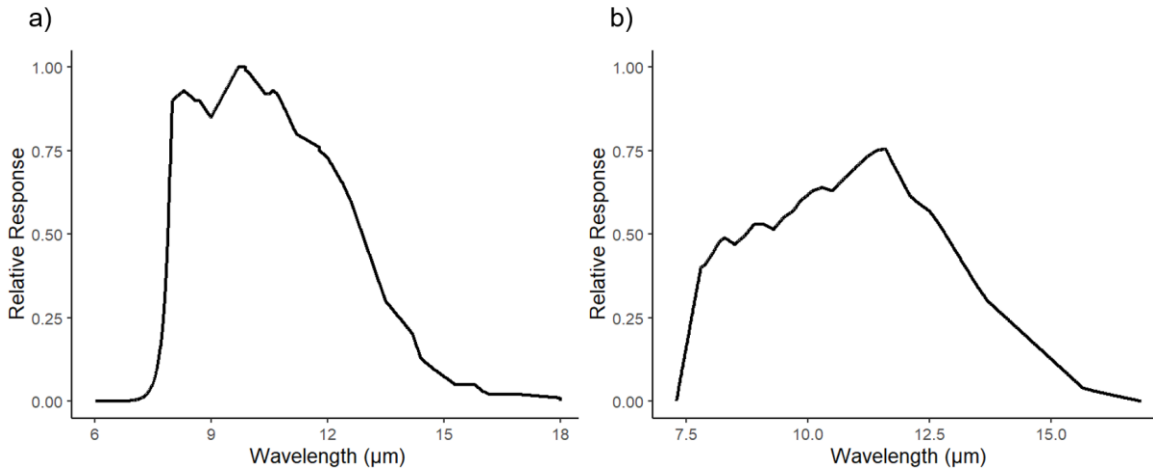


Figure 2.9 Spectral response curves for (a) FLIR T650sc and (b) Heitronics KT15.82 (FLIR, 2016 and Heitronics, 2004).

The integrated radiance was determined for each temperature and then plotted, and a third order polynomial was created for the FLIR thermal imager,

$$T_{Surf(FLIR)} = 6.00 \times 10^{-5} R^3 - 0.017 R^2 + 2.60 R + 212 \quad (2.5)$$

where T_{Surf} is the input surface temperature and R is the sensor detected radiance. This relationship between surface temperature and radiance produces a root mean squared error of 1.0. A second order polynomial was created for the Heitronics KT15.82 infrared pyrometer,

$$T_{Surf(KT15.82)} = -0.011 R^2 + 2.68 R + 221 \quad (2.6)$$

with a root mean squared error of 1. These polynomials express the relationship between the pixel temperature and integrated radiance for each sensor. They are used in conjunction with MODTRAN generated differences between remotely sensed

temperature and MODTRAN input surface temperatures to generate the correction polynomials used to atmospherically correct the images. Figure 2.11 shows the relationship between MODTRAN input surface temperature and pixel temperature for a sample MODTRAN iteration of 45° ONA and 1800 m altitude. The atmospheric correction polynomials are in the form:

$$DBT_{(z,ONA)} = a_{(z,ONA)}T_{obs(z,ONA)}^2 + b_{(z,ONA)}T_{obs(z,ONA)} + c_{(z,ONA)} \quad (2.7)$$

where DBT is the atmospherically corrected brightness temperature in °C, T_{obs} is the observed pixel temperature in °C, z is the height above ground level in m, and ONA is the off-nadir angle in (°). The correction coefficients are derived from the curve of best fit to the relationship between MODTRAN input temperature and pixel temperature and are calculated for every sensor ONA and altitude pair. The correction coefficients can be found in the supplementary material.

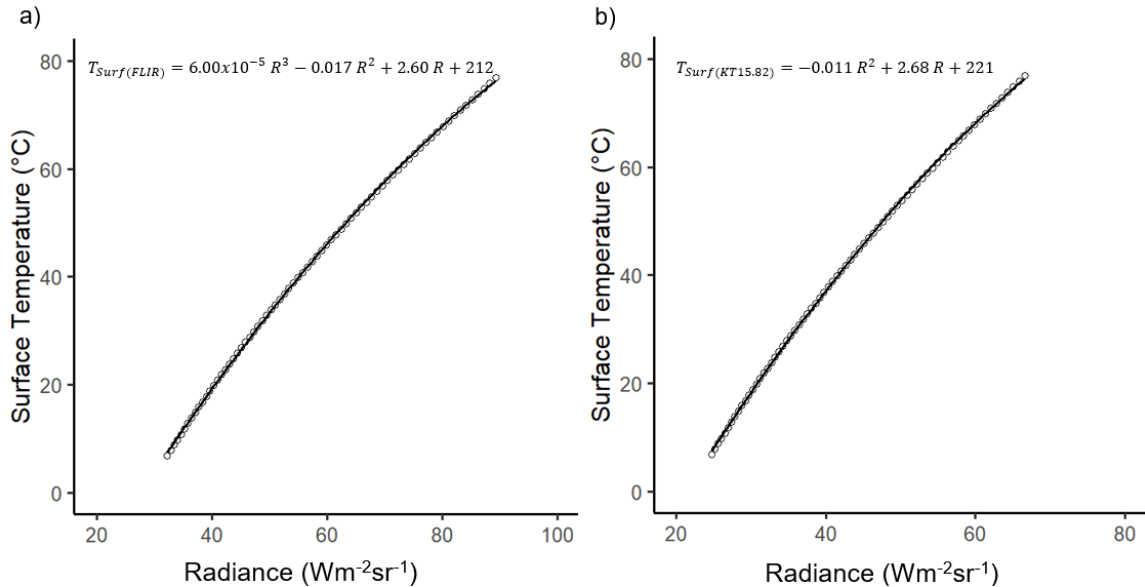


Figure 2.10 Relationship between surface temperature and channel radiance in a no-atmosphere simulation for the (a) FLIR T650 thermal imager and (b) Heitronics KT15.82 infrared pyrometer.

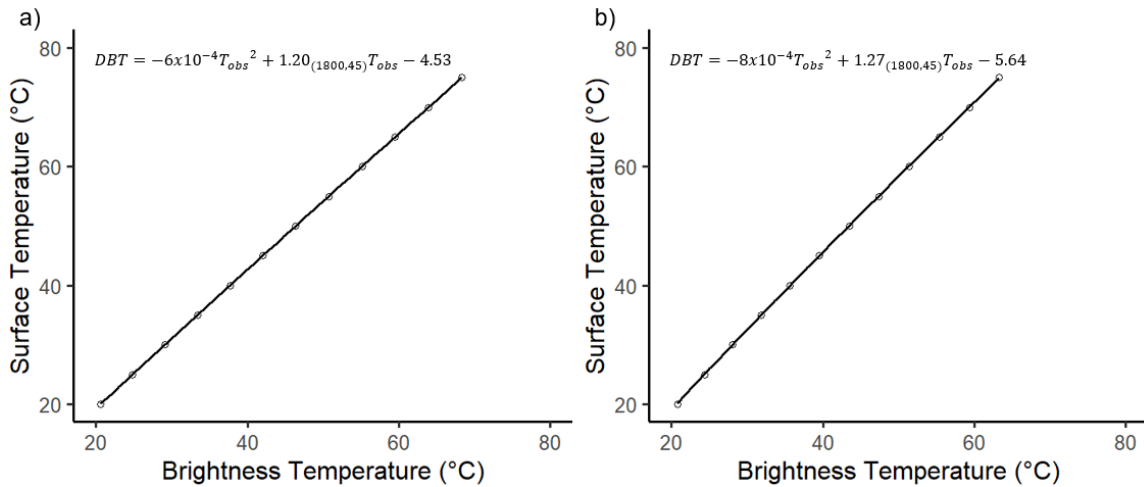


Figure 2.11 Relationship between MODTRAN input surface temperature and pixel brightness temperature. These plots are sample plots with a sensor orientation of 45° ONA and 1800 m above sea level for (a) FLIR T650 and (b) Heitronics KT15.82. The curve of best fit for each plot is expressed by a 2nd order polynomial for both instruments. Atmospheric correction polynomials are provided as supplemental material.

Table 2.8 shows a summary of MODTRAN input parameter step and bin sizes as determined by sensitivity tests found in Appendix B. MODTRAN calculated an at-sensor radiance associated with each true brightness temperature. These radiances were converted to at-sensor brightness temperatures and plotted against the true brightness temperature to determine a correction coefficient. The step size was chosen to create the best curve of best fit while minimizing MODTRAN iterations. ONA and sensor altitudes were continuous datasets that were binned based on sensitivity tests.

Table 2.8 Step or bin sizes for MODTRAN input variables.

Variable	Input step/bin size
True Brightness Temperature	5°C
Off-nadir angle	10°
Altitude	0.05 km

Atmospheric Profiles

MODTRAN 6 allows for user specified atmospheric profiles with up to 50 atmospheric layers that include the variables altitude (km), pressure (mbar), air temperature (K), water content (relative humidity (%), water vapour content (g/m^3), or dew point(K)), carbon dioxide, carbon monoxide, methane, and nitrous oxide. Values for the last four variables were extracted from the mid-latitude summer atmospheric profile provided by MODTRAN and linearly interpolated for our atmospheric profiles. The urban aerosol model was used for each MODTRAN iteration with visibility set to match observations made at MesoWest stations near each study site. Trace gas scaling factors were adjusted to match modern pollution levels as suggested by A. Berk et al., (2014). Uncertainty in the atmospheric corrections due to fluctuations in trace gases such as ozone, carbon dioxide, carbon monoxide and methane was found to be 0.2°C when comparing Salt Lake City minimum and maximum pollution levels observed during July 2018 as provided by the University of Utah's atmospheric monitoring stations. To obtain profiles of air pressure, air temperature, and air moisture content for use in MODTRAN, data from multiple sources were used.

Instrument systems

Radiosonde data as well as microwave radiometer data were available to generate atmospheric profiles for each study day. Radiosondes were launched to coincide with most helicopter flights as part of the project and measured altitude, temperature, relative humidity, wind speed and direction, and the position of the radiosonde. The radiosondes were launched from a field in the western region of the Salt Lake City valley at 1330 MDT 12 July 2018, 0900 MDT and 1330 MDT 15 July 2018, and at 1200 MDT and 1330 MDT 19 July 2018. The radiosondes were launched from an altitude of 1600 m, which was approximately 200 – 300 m higher than the study sites.

Data from a microwave radiometer provided by the University of Utah's Department of Atmospheric Sciences as part of the Above Surface Network database were also used.

The microwave radiometer was a Radiometrics MP-3000A passive atmospheric profiler. The microwave radiometer provided air temperature, relative humidity, vapour density, precipitation detector and a cloud base measurement approximately every minute.

In-canyon measurements of air temperature and relative humidity provided by the truck traverses were compared to the atmospheric profiling datasets. The microwave radiometer was located between a residential area and a commercial complex, so it is most likely to best represent the bottom-most layers of the atmosphere in Liberty Wells and White Sands whereas the radiosondes were launched in a field in the western part of the valley.

Profile Creation

The atmospheric profiles used for the atmospheric corrections of the 12 July 2018 and 15 July 2018 flights were created using temperature and moisture profiles generated by the MP-3000A microwave radiometer. The microwave radiometer provided temporally continuous data which allowed for different profiles to be created for each flight. The location of the microwave radiometer was also best suited for measurements of atmospheric variables within the city, as the radiosondes were all launched from less built areas. The SLC radiosondes were launched from the Salt Lake City International Airport and the radiosonde launched as part of this project was typically launched over a dry agricultural field. This means that the source area for the atmospheric profile data at or below the canopy layer will be based off different surface cover than the study sites. The atmospheric profiles used for the 19 July 2018 flights, however, were created using the data provided by the radiosondes launched for this project. Western Springs is a newer development surrounded by undeveloped land and is located much further away from the microwave radiometer (and closer to the radiosonde launch site), making the project radiosonde profile more suitable for this study site.

Profiles generated from the microwave radiometer data were created by averaging the atmospheric variables over every time step for the duration of each flight. The microwave

radiometer recorded data at 50 m intervals of altitude, which provided 15 atmospheric layers between the maximum helicopter altitude (~2000 m above sea level) and the ground. Kadygrov et al. (2015) found that the vertical resolution of ground-based microwave radiometers deteriorates with altitude, with a vertical resolution of 25 m at 100 m above ground level and 300 m at 500 m above ground level. The atmospheric profiles used for the atmospheric corrections in this project were constrained to ~600 m above the MWR altitude. Radiosonde launches made as part of this project as well as balloon launches provided by the SLC International Airport and ground-level meteorological data provided by the MesoWest network of weather stations were used to verify the profiles. The radiosonde recorded data every second, which provided 264 layers for the morning flight for the Western Springs site and 150 layers for the solar noon flight. The radiosonde data provides more atmospheric layers than the MODTRAN software will allow, creating the need to condense the profiles. The profiles exhibited very smooth cooling trends without any inversions or moist areas, making it easy to create a profile with fewer layers of equally spaced height increments. Appendix B provides an assessment of the sensitivity of these profiles to changes in relative humidity. The 1030 LAST radiosonde dataset was used to correct both WS8 and WS10. Figure 2.12 shows the radiosonde data to the height of the maximum helicopter flight altitude for the Western Springs neighbourhood and Figures 2.13 show the profiles used for the MODTRAN results.

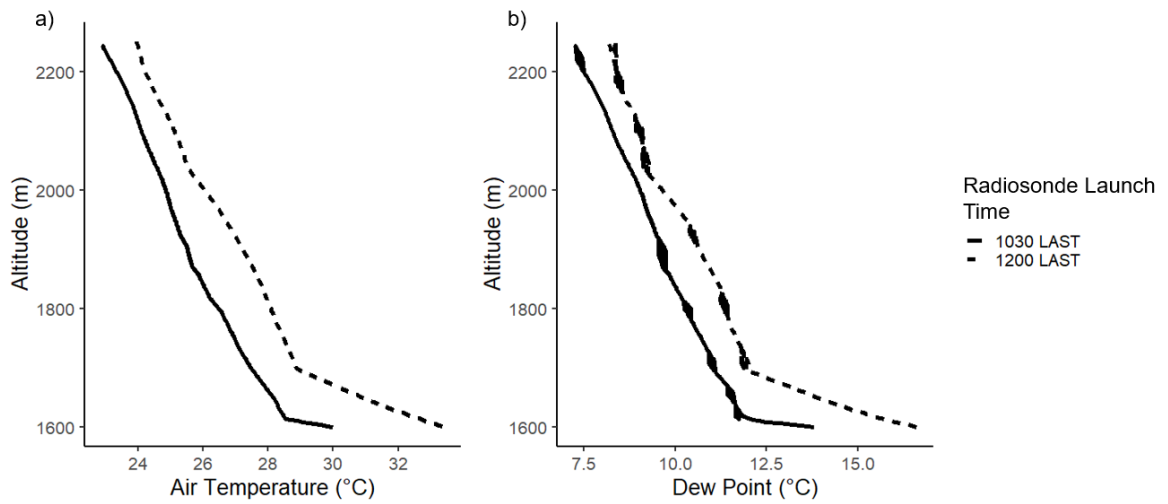


Figure 2.12 Radiosonde (a) air temperature and (b) dew point profiles for 19 July 2018.

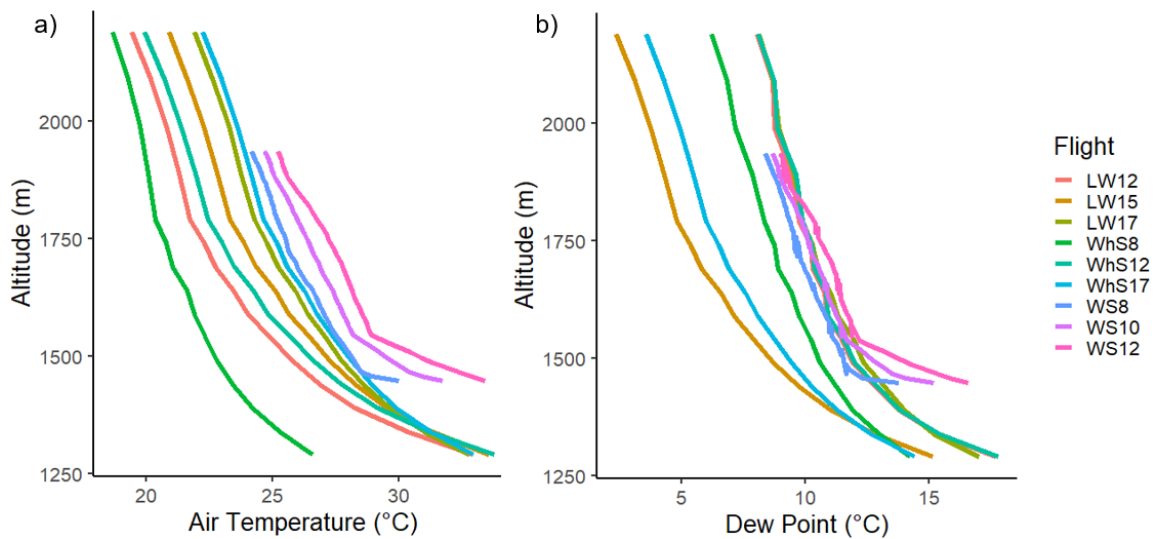


Figure 2.13 Atmospheric profiles for (a) air temperature and (b) dew point.

Comparison to Ground Measurements

Ground-based measurements from water, sunlit grass and road surfaces were used to evaluate the atmospheric corrections. These surfaces provide a range of temperatures that are associated with different atmospheric correction magnitudes. Water measurements were taken using a handheld OMEGASCOPE OS71 infrared thermometer, sunlit grass temperatures from a stationary infrared radiometer mounted as part of one of the LEMS stations, and road temperatures taken from the road-facing infrared radiometer on the traverse vehicle were used to validate atmospheric corrections. Mean surface temperatures were compared with mean pixel temperatures of the target surfaces located on the thermal image. The OMEGASCOPE instrument has an accuracy of $\pm 2^{\circ}\text{C}$ or $\pm 2\%$ of reading (OMEGA, 2020), the ACROBOTIC MLX90614 infrared radiometer sampling sunlit grass temperatures has an accuracy of $\pm 0.5^{\circ}\text{C}$ (Melexis, 2013), and the Apogee SIF-1H1 infrared radiometer sampling the road surface temperatures has an accuracy of $\pm 0.2^{\circ}\text{C}$ (Apogee, 2020). No corrections are made for surface emissivity as all comparisons are based on brightness temperature. The wavelength response of the various instruments used are similar.

Figure 2.14 show the comparison between ground measurements and atmospherically corrected brightness temperatures. The plots show that:

1. most of the mean corrected pixel values are within one standard deviation of the ground sampled values with the exceptions being the water measurements taken during LW17 and the sunlit grass measurements taken during WhS8;
2. the mean corrected pixel values of each off-nadir angle sampled are within one standard deviation of the other off-nadir angles sampled;

Due to the scale of the thermal images (with 1 pixel equal to $\sim 1\text{ m}^2$) it was difficult to sample the exact locations being sampled by the ground-based instruments. Instead, samples were taken from many similar sunlit surfaces across the image and an average was calculated to be compared to an average ground-based measurement. The samples taken from the thermal images were taken from pixels that were very clearly sunlit, and

so, might have been hotter than the actual location being sampled which wasn't as clear to spot. Variability in road temperature was very large ($\sim 2 - 5^{\circ}\text{C}$) and could account for the deviation from the 1:1 line for sunlit and shaded road surfaces.

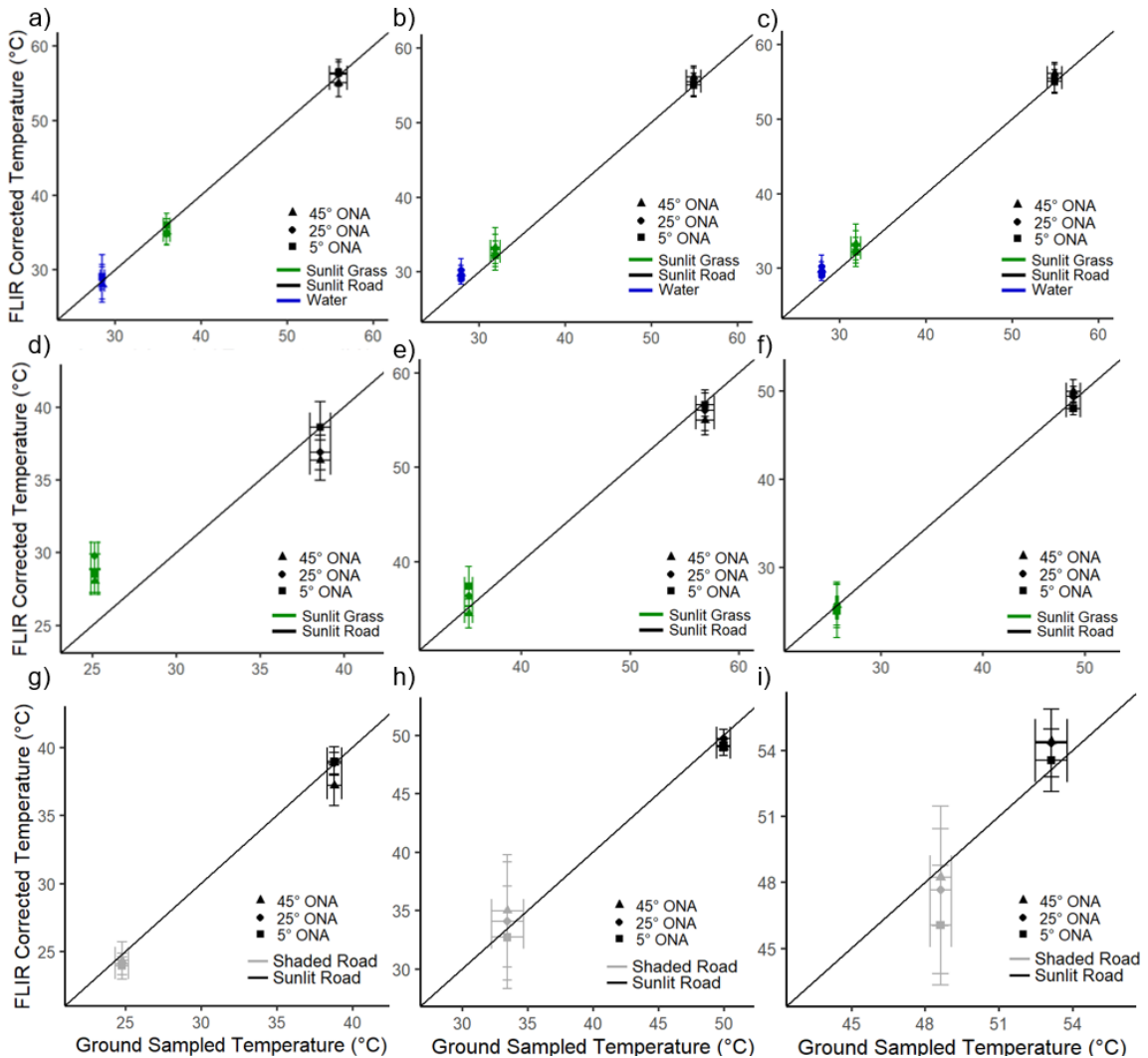


Figure 2.14 Comparison of ground measured surface temperatures to atmospherically corrected DBTs for (a) LW12, (b) LW15, (c) LW17, (d) WhS8, (e) LW12, (f) LW17, (g) WS8, (h) WS10, and (i) WS12. Error bars represent the standard deviation across all sample points. Points represent the mean temperature of sampled points from multiple images. The 1:1 line is indicated.

Atmospherically corrected brightness temperatures extracted from the images tend to be warmer than ground measurements for sunlit surfaces. Sampled road surfaces from the thermal images were taken from the middle of roads to ensure the pixel was not partly shaded or included as part of a lawn. The ground-based road-facing infrared radiometer mounted on the truck had a wide FOV that includes some sampling towards the side of the road. This may impart a possible cool bias, especially if the instrument FOV captures some non-road surfaces.

Application of Atmospheric Corrections

A separate correction polynomial was created for every observer height and off-nadir angle combination. The integrated radiances for 20 - 75°C MODTRAN input surface temperatures in 5°C steps were converted to remotely sensed temperature values using the “no-atmosphere” lookup table described earlier. The remotely sensed temperatures were plotted against the input surface temperatures to generate correction polynomials. The thermal imager recorded pixel temperatures in °C, so by plotting the remotely sensed temperature against the input surface temperature, the pixel temperature could be substituted into the correction polynomials to correct to the brightness temperature of each pixel. An example of corrections required for a particular flight and altitude are shown in Figure 2.15.

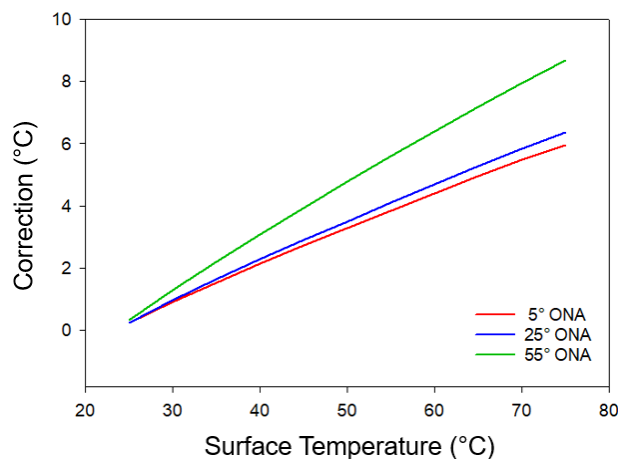


Figure 2.15 Atmospheric corrections for LW12 at an altitude of 1900 m.

The imager lens used in the airborne sampling has a very large field of view (FOV), meaning that the path lengths differ significantly across the FOV. Bins of 10° off-nadir angle were selected as reasonable step sizes for the corrections, so images that were captured in portrait view require five different correction polynomials. The horizontal FOV of 34° yields a maximum change in path length equivalent to 17° ONA from nadir. Changes in atmospheric corrections are very small ($>1^\circ\text{C}$) for small ONA (see Figure 2.16) due to small changes in path length at these angles and so a single atmospheric correction was applied horizontally across each thermal image. To apply different corrections to the same image, five rectangular shape files were created in ArcGIS using the relative coordinate system of the images (see Figure 2.16). Each raster was then clipped to the shape files and a separate polynomial correction was applied to each clipped raster. The corrected rasters were then merged back together.



Figure 2.16 Thermal image with the five different atmospheric correction zones indicated by red boxes. The uppermost rectangle has the longest path length and thus the correction polynomial yields the largest corrections; the bottom most rectangle has the shortest path length and leads to smaller correction magnitudes (see e.g. Figure 2.16). The observer is East facing at a 45° ONA.

2.3.3 Zonal Statistics

The source area for each image is sufficiently large that it contains many iterations of the primary surface structure that determine the variability and anisotropy of urban surface temperature; namely the inter-building spacing and vegetation distribution. This allows for the image to be subdivided into smaller zones that still provide a good spatial sampling of the surface, representing multiple surface components. By imaging the off-nadir flight lines in portrait view, the upper and lower portions of the image can represent different view angles. Each off-nadir image was then subdivided into three new off-nadir angles. The middle portion of the image represented the angle measured by the Aaronia tilt sensor. The upper and lower portions of the image can then be used to represent ONA $\pm 11.25^\circ$ from that measured from the tilt sensor.

Sensitivity Test of FOV_{subset} size

Circular areas (FOV_{subset}) were extracted from the middle, top and bottom halves of the images. To determine an appropriate area for these FOV_{subset} , a sensitivity test was performed using one set of flight data and 5° , 10° , 15° , and 20° FOV_{subset} . Figure 2.17 shows an example of the FOV_{subset} superimposed over a sample thermal image. The range of FOV_{subset} sizes was determined by taking the smallest FOV_{subset} that still contains at least one full iteration of the built surface and the largest FOV_{subset} was determined by taking the largest area possible while staying away from the edges of the image due to avoid the vignette effect discussed in Appendix A.



Figure 2.17 Sample thermal image with increasing FOV_{subset} .

The results of the test are shown in Figure 2.18 where the box plot represents the average mean temperature of each FOV_{subset} for the specified ONA and view azimuth angle. The 5° FOV_{subset} , which only contained one full iteration of the surface cover, shows the largest range and IQR as which was to be expected. The IQR decreases as the FOV is

increased, however the overall range and IQR does not change by more than 0.5°C between the 15° and 20° $\text{FOV}_{\text{subset}}$. A $\text{FOV}_{\text{subset}}$ of 15° was chosen to minimize the variability generated by a very small $\text{FOV}_{\text{subset}}$ while still restricting the $\text{FOV}_{\text{subset}}$ to a size like other infrared radiometer instruments and to minimize overlap between the three subset areas. This 15° $\text{FOV}_{\text{subset}}$ contains several houses and trees to capture the anisotropy created by all possible surface types.

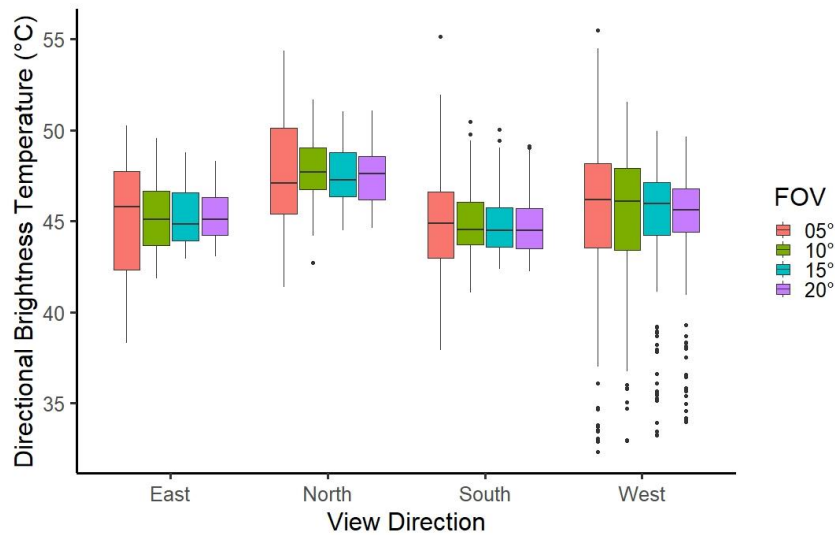


Figure 2.18 Boxplot comparison of different $\text{FOV}_{\text{subset}}$. Bottom and top of the box represents the first (Q1) and third quartile (Q3) respectively and therefore the range of the box represents the interquartile range (IQR). The line within the box representing the median (Q2). Whiskers represent the minimum and maximum datapoints excluding outliers. Outliers are indicated by points plotted outside of the box and whisker range.

Using circular shape files with a 15° $\text{FOV}_{\text{subset}}$, the mean temperature of each new off-nadir angle was extracted from the images. These zonal averages were then combined for each view direction and off-nadir angle and averaged to generate a single temperature for each azimuth and off-nadir angle pair. Figure 2.19 shows a thermal image with the three 15° $\text{FOV}_{\text{subset}}$ added. Every image was sorted by its ONA and view azimuth. The mean temperature within the $\text{FOV}_{\text{subset}}$ of each image was calculated and then the mean of these

FOV_{subset} was calculated to determine one temperature per ONA and view azimuth that would then be plotted on the polar plots.



Figure 2.19 45° ONA thermal image with 15° FOV_{subset} superimposed on the image.

Sensitivity Test of FOV_{subset} and Atmospheric Correction Region Overlap

The method of applying multiple atmospheric corrections and extracting multiple smaller FOV_{subset} from each image created areas of overlap where more than one atmospheric correction polynomial was applied to each FOV_{subset} . Figure 2.20 illustrates the overlap being discussed.

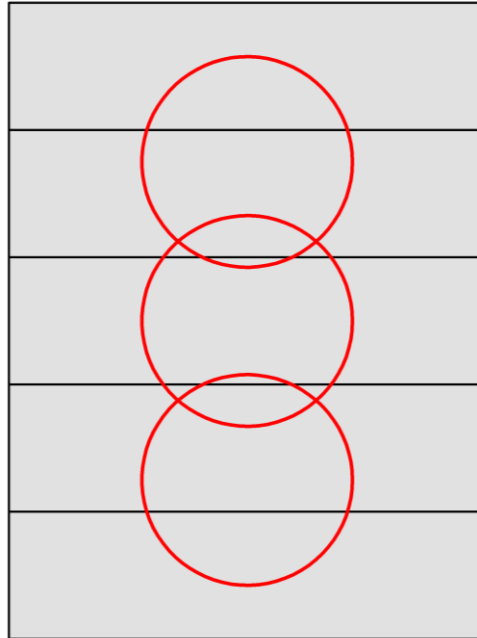


Figure 2.20 Diagram of overlap between atmospheric correction polynomials (grey rectangles) and subset FOV (red circles). Three atmospheric correction areas overlap each subset FOV.

From Figure 2.20, three atmospheric corrections are applied to each FOV_{subset} with the three different corrections being unevenly applied to the FOV_{subset} . Tests were performed to determine the effect of different atmospheric corrections being unevenly applied to FOV_{subset} on the extracted average temperature. To do this a sample image with a 45° ONA and sensor height of 1800 m was used. A 15° FOV_{subset} was superimposed onto the thermal image and the overlap of atmospheric corrections for this FOV_{subset} were adjusted. The three atmospheric corrections being moved are referred to as Correction 1 (with the shortest path length), Correction 2 (the mid-point of the image), and Correction 3 (with the longest path length). Table 2.9 summarizes the results of the test. The bolded scenarios represent the three different correction overlaps for each of the actual FOV_{subset} extracted from each image. The largest difference of 1.28°C was found to be between 100% overlap of Correction 1 and 100% overlap of Correction 3 as the two correction polynomials represent the largest change in path length over the vertical range of the FOV_{subset} . The FOV_{subset} decreases as the percentage overlap of Correction 1 is decreased

and subsequently Correction 3 is increased. The largest difference between the actual overlap of correction polynomials (the bolded scenarios in Table 2.9) between FOV_{subset} is $0.36^{\circ}C$, which is within the accuracy range of the thermal imager and considered acceptable.

Table 2.9 Sensitivity test of overlap between atmospheric correction areas and subset IFOV. Correction 1 is the atmospheric correction for the longest path length, Correction 2 is the correction for the center of the FOV, and Correction 3 is the correction for the shortest path length for the sample FOV_{subset} . The bolded scenarios represent the percentage of overlap for each actual FOV_{subset} extracted from each image.

	Correction 1	Correction 2	Correction 3	Average Brightness Temperature ($^{\circ}C$)
	100	0	0	42.15
	0	100	0	41.32
	0	0	100	40.87
Overlap	40	60	0	41.61
with	35	60	5	41.55
FOV_{subset}	30	60	10	41.50
(%)	20	60	20	41.38
	10	60	40	41.25
	5	60	35	41.19
	0	60	30	41.12

Evaluation of Method

The method utilized in this thesis involved subdividing a single thermal image into three zones, each representing a new view angle dependent on the measured angle of the original image. The original target off-nadir angles for the sensor platform were 25° and 45° so after using this method, the intention was to have coverage of 13.75° , 25° , 33.75° , 36.25° , 45° , and 56.25° off-nadir angles. Due to the movement of the helicopter and a moveable camera mount, our dataset of measured angles ranged from 5° - 55° off-nadir before using this method, so with the method our coverage of off-nadir angles became 3.75° , 5° , 14.25° , 15° , 23.75° , 25° , 26.25° , 33.75° , 35° , 36.25° , 43.75° , 45° , 46.25° , 55° ,

and 56.25°. Figure 2.21 shows the implementation of this method, with the new area averaged temperatures from the upper or lower portion of an image following the same trend of decreasing with increasing off-nadir angle as the directional temperatures extracted from the middle of the images were the tilt of the instrument was measured. The spatial variability of the site becomes more apparent as the thermal imager views larger off-nadir angles, contributing to the increase in the difference of DBT. Averaging over similar angles (with a difference $< 2^\circ$) reduced this variability.

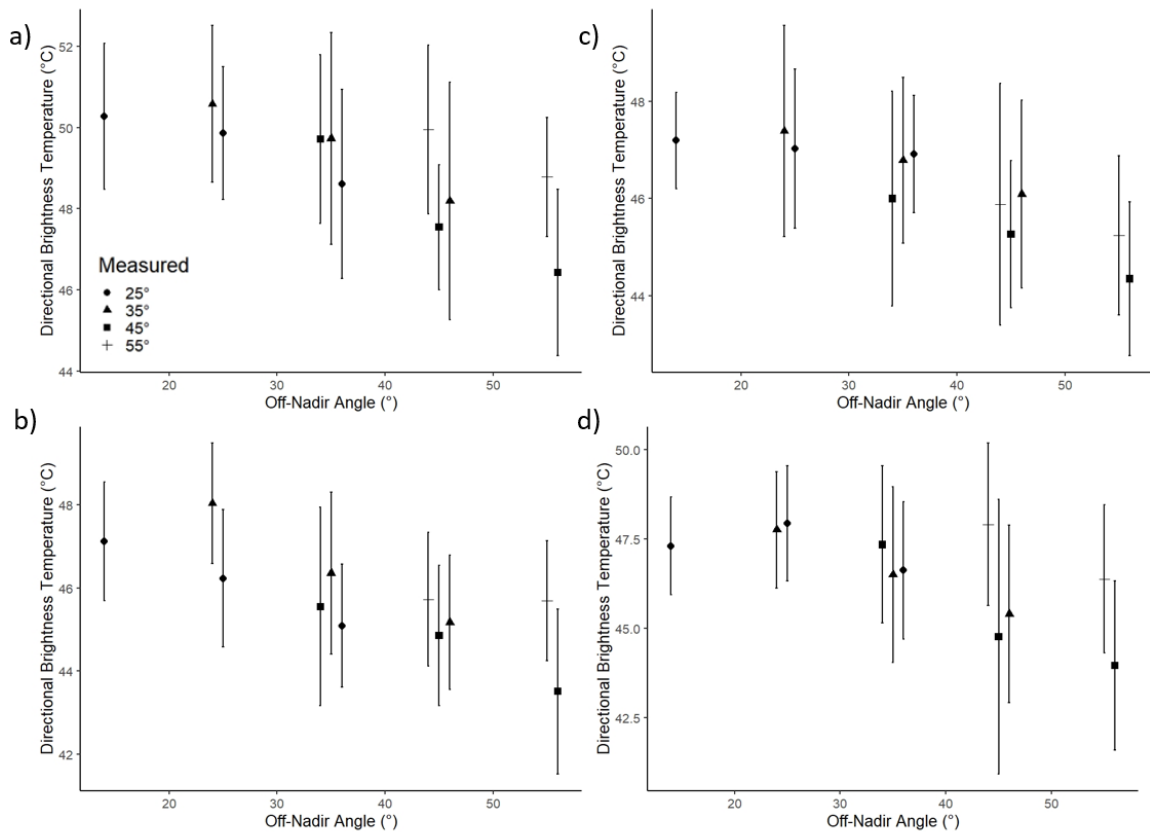


Figure 2.21 Method analysis for LW12 with the observer viewing (a) North, (b) South, (c) East, and (d) West. Points represent averaged DBTs with similar measured angles. The symbols indicate the center angle of the images as measured by the Aeronia GPS Logger and the error bars represent standard deviation between images.

2.4 Summary

Thermal images were taken every 0.5s for 5° - 65° off-nadir and 8 (Liberty Wells and White Sands) or 16 (Western Springs) view azimuths for 3 sites over 3 days. The thermal images were first atmospherically corrected and then a subset of three circular 15° FOV were extracted from each image to create 3 ONA samples from 1 thermal image. The average DBT of each 15° FOV was calculated and sorted by ONA and view azimuth. These new DBT were then averaged to create a single DBT for each ONA and view azimuth point which were then plotted on polar plots to represent the directional variability of DBT.

Chapter 3

3 Results and Analysis

This chapter will analyze the results of the dataset outlined in the previous chapter. First, the incoming solar radiation and air temperature of each site will be discussed followed by a descriptive analysis of thermal imagery. Next, the change in surface temperatures due to the flight lengths is examined by modelling the change over time of DBT for each flight and comparing data from the start and end of each traverse. Correction polynomials are then generated for necessary flights to correct for temporally changing surface temperatures. Atmospherically and temporally corrected polar plots are presented next along with an examination of the effective anisotropy and shapes of these plots. A comparison of polar plots created using the FLIR thermal imager and Heitronics KT15.82 infrared pyrometer is examined followed by a comparison of off-nadir and nadir temperatures. Differences in opposing wall temperatures are then examined as a source for variations in anisotropy and finally, an assessment of the spatial variability of each site is discussed.

3.1 Environmental Conditions

3.1.1 Incoming Solar Radiation

Three sites were observed over three different days during the observation campaign. The environmental conditions on these days provide boundary conditions for the expected thermal anisotropy.

Solar radiation forms an important forcing for thermal anisotropy because it is a major determinant of the maximum surface temperatures and so is a control on the maximum DBT ($T_{B,max}$). During the morning traverse time the difference between White Sands and Western Springs was 15 Wm^{-2} (3% of the morning solar radiation values). There was some scattered convective cloud in the morning for the Liberty Wells site which, by the time of LW12, were dissipating. It is not expected that this morning cloud would have impacted our solar noon thermal anisotropy because the scattered cloud cover allowed for

some surface warming and data obtained from our observation site during the 12 July sampling day suggests the clouds had dissipated by 1130 LAST over our area of interest. Figure 3.1 shows some cloud cover still occurring at solar noon however this is because the MesoWest station used to generate this was located near the mountains and was observing some orographic clouds that were not present in the valley at this point. The time series of solar radiation is similar to that for the other two sites for the rest of the day. The three incident solar radiation time series are very similar during each of the similarly timed flights, with the average difference between each of the three sites being between 5 - 15 Wm^{-2} (1.5 % of the solar radiation value). The downward spike observed for all three sites at approximately 1330 LAST is likely caused by an obstruction near the pyranometer as it is observed briefly for all three sites at the same time of day. Figure 3.1b shows the difference in incoming solar radiation between each study day during the three similar flight times. The difference between 12 July and the other two flights at solar noon is large because of the orographic clouds still present over the University of Utah Mountain station, however in-site observations from a LEMS station placed on a scissor lift within the site show a mean difference of 15 Wm^{-2} between 12 July and 15 July. The scissor lift LEMS station was not deployed for 19 July, however the similar trend in the difference in incoming solar radiation observed in Figure 3.1b suggests a similar difference would have been observed. The morning and afternoon flight times show reasonable differences between 0 – 22 Wm^{-2} with the largest differences observed during the morning time period. These conditions are very similar and give confidence that the solar forcing conditions were similar during observation periods, allowing comparison of anisotropy between sites.

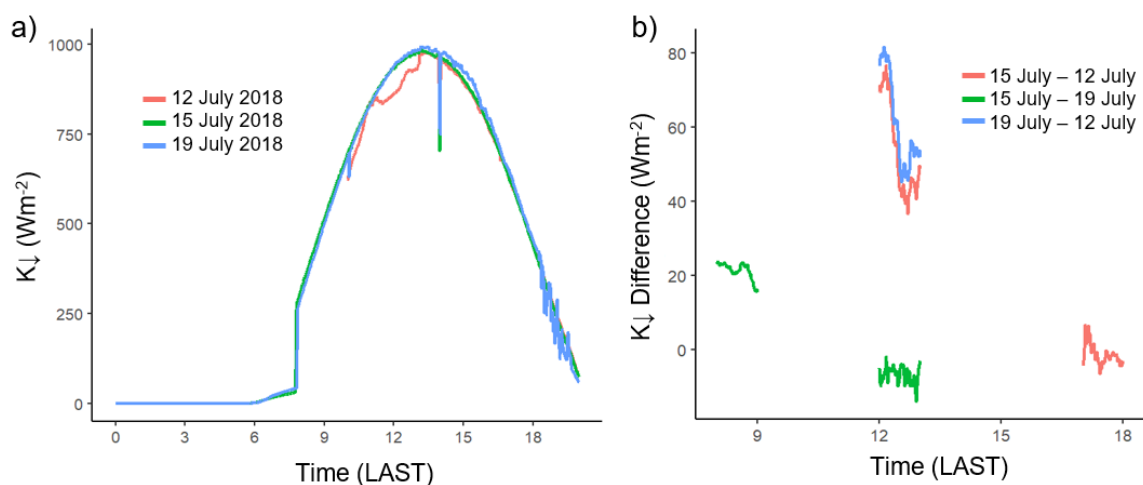


Figure 3.1 (a) Incoming solar radiation (K_{\downarrow}) for each study day and (b) the difference in K_{\downarrow} between each study day. Time is in local apparent solar time in hours. K_{\downarrow} values were obtained from the MesoWest University of Utah Mountain (MTMET) station.

3.1.2 In-canyon Air Temperature

Air temperature provides a boundary condition for thermal anisotropy because it exerts a strong influence on the most shaded surface temperatures, and hence the minimum directional temperature, which is important to the overall range of thermal anisotropy (Krayenhoff & Voogt 2016). The diurnal air temperature evolution lags behind the surface temperature of exposed horizontal surface facets. The diurnal evolution of air temperature (shown in Figure 3.2) for each of the study days follows the expected pattern of heating and cooling, with the peak temperature for each day approaching 35°C . The air temperature for Western Springs was $\sim 2^{\circ}\text{C}$ warmer than that of the other two study days during all three of the Western Springs flights. The air temperatures for Liberty Wells and White Sands were more similar with a difference in air temperature of $\sim 0.1^{\circ}\text{C}$ during the morning which increased to a difference of $\sim 1.5^{\circ}\text{C}$ at solar noon. By the afternoon flights the air temperature had reached its peak and the difference between the Liberty Wells and White Sands study days was 1°C .

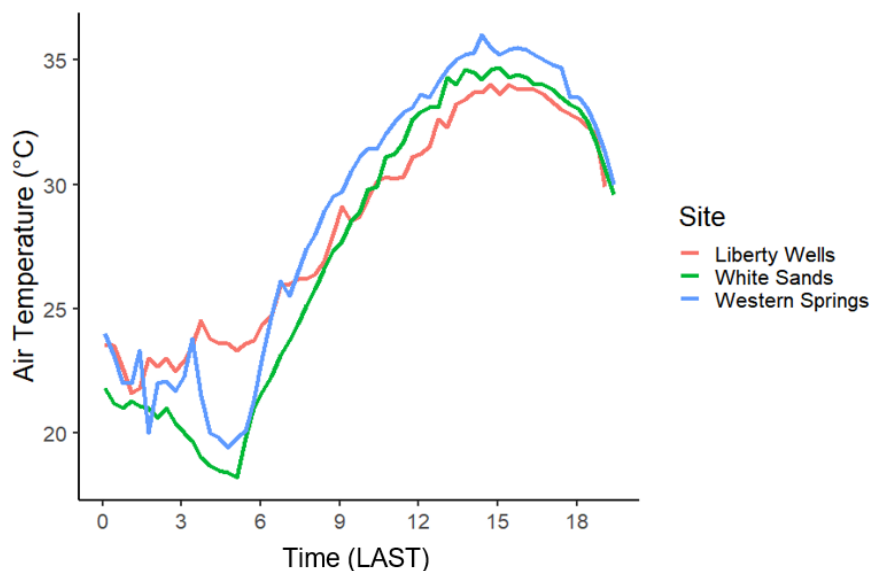


Figure 3.2 Air temperature for each study day. Time is in local apparent solar time in hours. Air temperature values were obtained from the MesoWest Salt Lake City Municipal Airport (KU42) station.

3.1.3 Wind Speed

Surface level (10 m) wind speed is an important control on surface temperature. Strong wind speeds have the potential to cool hot surfaces, reducing the thermal anisotropy. Figure 3.3 shows a comparison of wind speeds as reported by the Salt Lake City Municipal Airport located in the middle of the Salt Lake City valley for all three study days.

The overnight and early morning wind speeds are a strong control on surface temperatures for morning sampling, and it can be seen from Figure 3.3 that the wind speeds are $\sim 3 \text{ ms}^{-1}$ before sunrise for the White Sands study day but are calmer for the Western Springs study day. This suggests that conditions could have led to the warming surfaces in White Sands to be slightly cooler than they would have been if they had been sampled on the same day as the Western Springs site.

From Figure 3.3, the wind speeds stayed between $4 - 6 \text{ ms}^{-1}$ after sunrise on the Liberty Wells study day except for between solar noon and 1600 LAST where the wind speed was reduced to between $0 - 2 \text{ ms}^{-1}$. The wind speeds for the White Sands study day followed a similar pattern with wind speeds slightly reduced in the morning compared to Liberty Wells ($\sim 2 - 4 \text{ ms}^{-1}$ or $\sim 2 \text{ ms}^{-1}$ slower than the Liberty Wells study day) and a decrease around solar noon to 0 ms^{-1} . In contrast, the winds were significantly calmer during the morning of the Western Springs sampling. The air temperature was also slightly larger than the other two study days at solar noon, possibly due to the calmer surface winds. This implies there is a possibility that the maximum surface temperatures for the Western Springs site could be slightly warmer at solar noon than the other two study days.

The difference in wind speeds in the afternoon between Liberty Wells and White Sands was $\sim 0.5 - 1.5 \text{ ms}^{-1}$. LW17 and WhS17 were the only afternoon flights flown and this similar wind speed indicates the conditions were similar during the flights.

Wind speed measurements obtained at the airport are representative of wind speeds in an open area at a height of 10 m above ground level which means the actual winds in each study area could be slower due to the more aerodynamically rough urban form. Wind speeds observed in-site for the 12 July and 15 July study days were approximately 2 m/s slower on 12 July and 2 – 3 m/s slower on 15 July with wind gusts reaching maximum values observed in Figure 3.3. The overall pattern, however, is similar with calmer winds observed in the morning and slightly stronger winds observed in the afternoon.

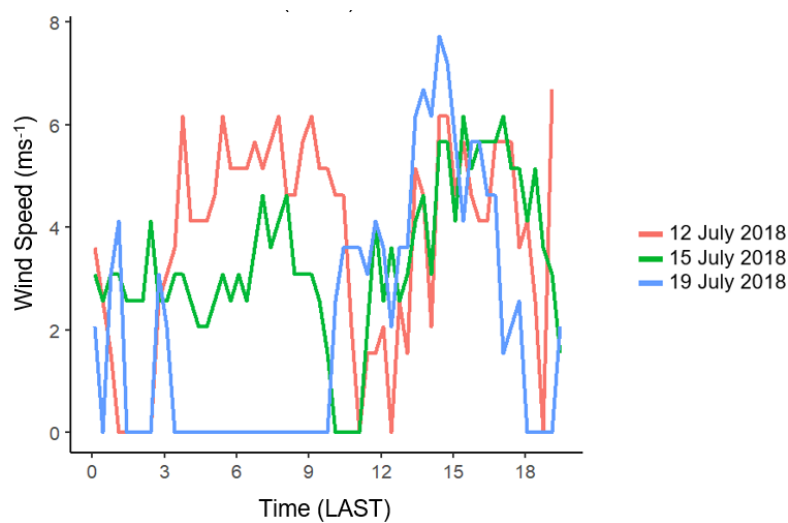


Figure 3.3 Surface level wind speed for each study day. Time is in local apparent solar time in hours. Wind speed values were obtained from the MesoWest Salt Lake City Municipal Airport (KU42) station.

3.2 Descriptive Analysis

Figure 3.4 shows an example of two thermal images and coupled GoPro images of Liberty Wells during the late afternoon traverse with atmospheric corrections but no emissivity corrections. Figure 3.4b was taken at approximately 1730 LAST at a 25° ONA with the imager pointing west. From this image certain details of the study site can be seen. The temperature scale of this image ranges from 3.0 °C to 60.3°C with roofs and roads clearly showing up at the hottest end of the scale. Tree canopies are near air temperature, 34.8 – 35.9°C for this flight, and so contrast very clearly against warm surfaces like the roofs or roads, but also against lawns where irrigation and shading by trees or buildings keep surface temperatures cooler. Clear shading patterns can be seen from trees and buildings. Most of the shading observed in this image is cast by tree canopies, reducing the overall temperature of the image by cooling hot surfaces, particularly road temperatures. Due to the layout of the neighbourhood, the buildings cast shade on the already cool lawns but trees, in particular trees planted along the roads,

cause a lot of cooling by shading these otherwise hot surfaces. In this image, roofs are the hottest at around 60 - 70°C for the sun-facing side, however due to the roof pitch, there is significant self-shading causing the shaded roof temperature to be significantly cooler at around 35°C. Road temperatures range between 40 - 55°C, with smaller roads appearing hotter than the larger roads, most likely due to the surface properties of the different asphalt or concrete roads, as the GoPro image in Figure 3.4a shows, the roads are a different colour in the visible spectrum as well.



Figure 3.4 GoPro (a and c) and thermal image (b and d) of the Liberty Wells neighbourhood from a 25° ONA and a (a – b) western and (c – d) eastern view azimuth.

The DBT of a surface is dependent on both the orientation of the surface and sensor as well as the material properties of the surface being observed. This is clearly demonstrated in the lower portion of this thermal image where a group of houses have roofs that appear very cool, between 3 – 25°C which is a significant difference compared to most of the roof temperatures. This highlights the importance of having multispectral data available when analyzing surface materials. The roofs in question are made of a white, reflective material that reflects significantly more incoming solar radiation than a standard black roof, thus lowering the amount of absorbed solar radiation and causing the roof to be cooler. Another feature that is not apparent in the thermal image but becomes clearer in the visible spectrum is the size and intensity of the shadows being cast by the trees or buildings. This flight occurred in the late afternoon when the shadows were lengthening, meaning the farthest part of the shadow is more recent and hasn't had as much time to block the surface from the sun. Figure 3.4d shows the same radiation source area and ONA but from the opposite view azimuth (east). This image has a temperature scale of 4.1 – 64.3°C. The temperature scale is larger for this image since more sunlit surfaces are observed.

3.3 Analysis of Temporal Change

Daytime surface temperatures are largely determined by absorbed solar radiation as determined by surface radiative and thermal properties and by convection. The solar angle changes throughout the day, which not only changes the amount of radiation received by each surface facet but also the amount of shade being cast. Temperatures of different surface facets, such as roofs and walls, change at different rates and reach different maximum daily temperatures due to the material properties of the facet as well as the amount of solar radiation received. Figure 3.5 shows modelled surface temperatures generated by the urban energy balance model TUF3D (Krayenhoff and Voogt, 2007) for the White Sands site. It shows the large diurnal variability of component temperatures, especially of horizontal surfaces such as roofs. Even over relatively short periods of time, especially in the early to mid-morning and mid-afternoon time periods,

changes in surface temperature can be significant. This poses a potential problem for constructing a polar plot of DBT that represent the same time from the airborne data that required collection times of 20 – 40 min.

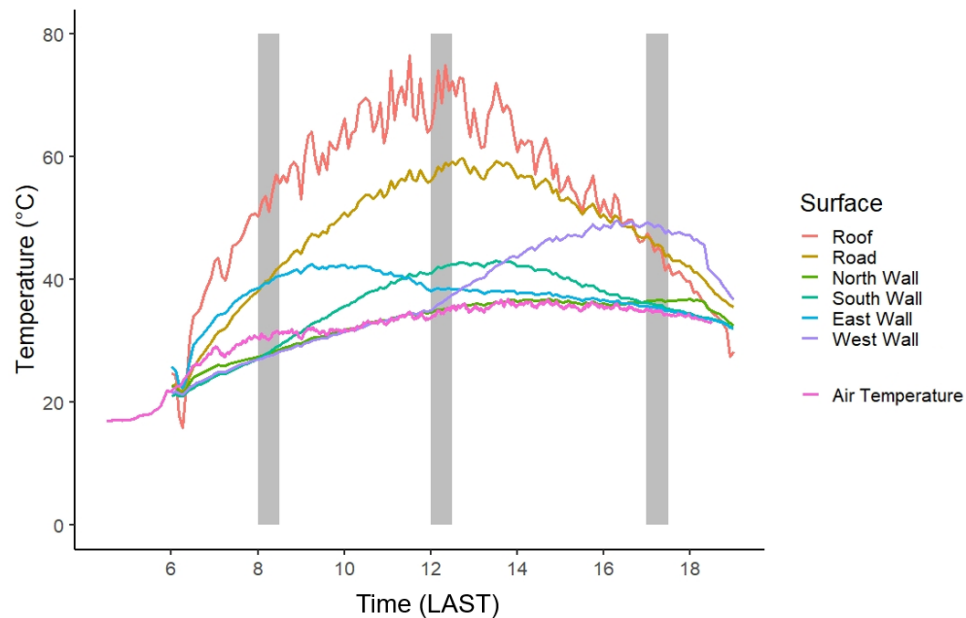


Figure 3.5 TUF3D modelled surface temperatures for the White Sands site. WhS8, WhS12, and WhS17 flight times are noted on the graph by the grey bars. Noise in roof surface temperatures are most likely a result of convection.

3.3.1 Temporal Change and Polar Plots

A convenient way to depict thermal anisotropy is by plotting DBT on a polar plot where the nadir brightness temperature is plotted in the center and increasing ONA brightness temperatures are plotted at increasing radials. The azimuth angles are plotted as the sensor view direction. Polar plots highlight hot regions, view directions where the sensor is observing the maximum sunlit surfaces, and cool regions where the sensor is observing the maximum shaded surfaces. This hot region is referred to as the hot spot and for the purpose of this thesis is defined as DBTs greater than the 95th percentile ($T_{B,95}$). The coolest region of the polar plot can likewise be described as less than the 5th percentile ($T_{B,5}$).

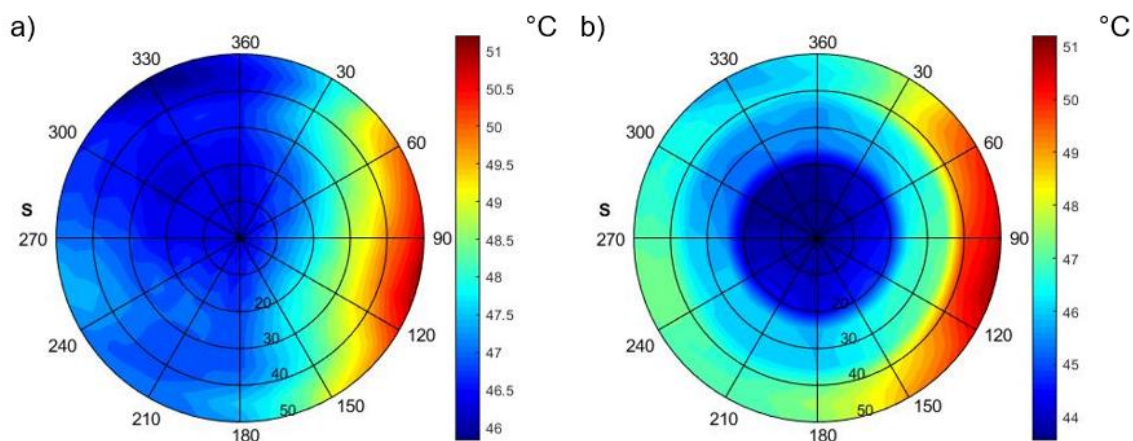


Figure 3.6 Polar plot of uncorrected directional brightness temperatures for WS17. Temperatures are generated from TUF3D to demonstrate the blurring effect of sampling different angles and view directions at different times. (a) model generated DBT for a single point in time and (b) DBT sampled at different times for different ONAs through the traverse.

Figure 3.6 shows the results of a simulation that tests the effect of changing solar position, and thus temporally changing component surface temperatures, on a polar plot. Surface temperatures for a simplified urban surface are calculated using the TUF3d model (Krayenhoff & Voogt 2007) and component surface temperatures are then used in the SUMVeg sensor view model to model the DBT. These polar plots represent a late afternoon flight where west facing surfaces are receiving direct solar radiation, so the hot spot appears for easterly sensor view azimuths. The flights were flown such that 45° ONA were sampled first, then the 25° ONA and lastly nadir (or as close as we could sample) was sampled. Since the surfaces are cooling in the late afternoon, this causes the outer portion of the polar plot to appear warmer than the center and can cause some distortions of the hot spot itself. Previous studies have shown that the hot spot region of a polar plot moves throughout the day such that it stays opposite the sun's position. The hot spot can become blurred and stretched if surface temperatures are changing

significantly as they are being sampled as the location of the hot spot moves with the solar position throughout the day.

Figure 3.7 shows the change in solar angle during each flight for each site. Each line represents a flight with the length of the line indicative of the change in solar position for that flight. Figure 3.8 shows the atmospherically corrected (but not temporally corrected) polar plots. A flight suspected of having temporal effects within the polar plot is LW17. The north, south, east, and west 25° view angles were sampled approximately 10 minutes later than the northeast, northwest, southeast and southwest 25° ONA samples due to the helicopter being re-routed mid-flight. This gap in sampling created pockets of cooler DBT sampled in those locations of the polar plot. The Western Springs flights took less time than the other two sites, so less temporal DBT change is expected. Other distortions of the plots are less apparent but some degree of blurring as shown in Figure 3.6 is expected for some flights.

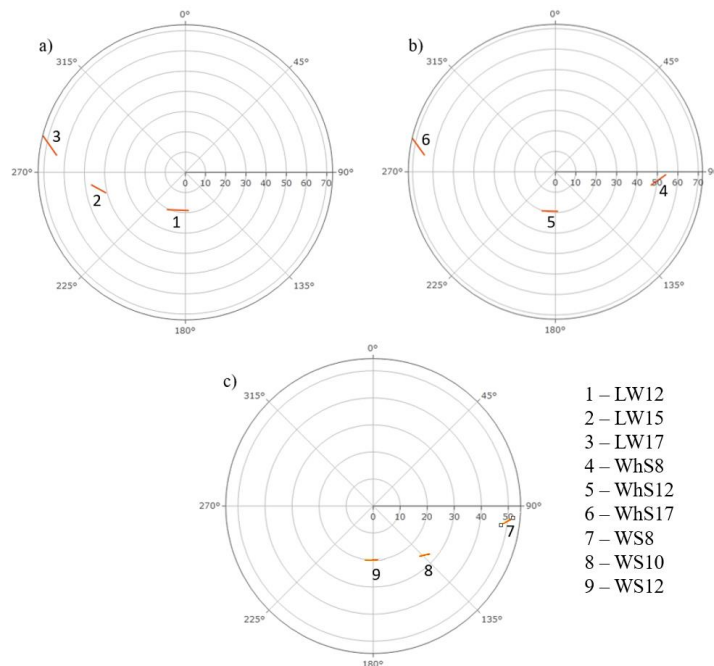


Figure 3.7 Solar position for the duration of each flight for (a) Liberty Wells, (b) White Sands, and (c) Western Springs.

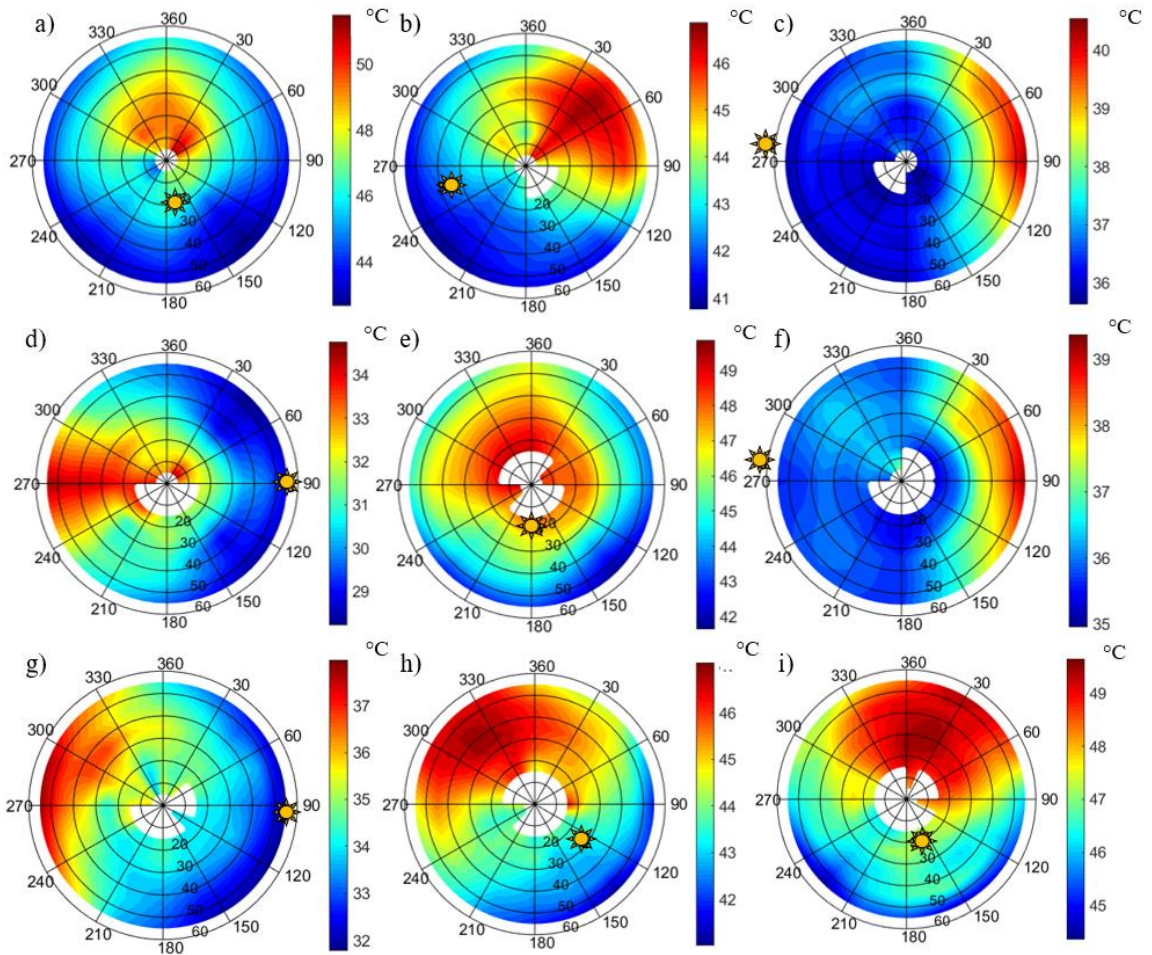


Figure 3.8 Atmospherically corrected (but temporally uncorrected) polar plots for (a) LW12, (b) LW15, (c) LW17, (d) WhS8, (e) WhS12, (f) WhS17, (g) WS8, (h) WS10, and (i) WS12.

The goal of this thesis was to capture the DBT from multiple view angles and view directions under similar environmental conditions that could then be compared to determine the effective anisotropy. The assumption is that the directional variability in DBT arises from changes in sensor (observer) viewing geometry, and not due to changes in any of the forcing conditions. This is not possible if the underlying surface temperatures show significant changes over the time required to collect all the airborne data. Because the airborne data take a finite period of time to collect, this section

assesses the need to correct DBT for temporal changes. Whether a correction was necessary for each flight was determined by running SUMVeg, a sensor view model used to model DBT for different ONA and view azimuths, to calculate the modelled change in DBT for each sensor orientation. These model results were then compared to repeated flight lines to determine the validity of the corrections. Repeated flight lines were flown for the same ONA and azimuth view angles as the start of the traverse. This means that four azimuth view angles and one ONA for the Liberty Wells and White Sands sites and one azimuth and ONA for Western Springs site. Temporal changes in DBT are dependent on the ONA and view azimuth, meaning a simple correction using the repeated data is insufficient for every view direction sampled. Consequently, this data was used to evaluate the performance of correction polynomials created using modelled DBT over 15-minute time steps.

3.3.2 Model Results

The magnitude of the change of an area averaged DBT is dependent on the azimuth and ONA of the sensor as well as the time in relation to the start of the flight. This means that each point on the polar plot could require a different correction polynomial. To accurately correct the polar plots being examined, SUMVeg, a sun-surface-sensor relations model that incorporates vegetation was used to generate expected anisotropy for 15-minute time steps. Multiple iterations of SUMVeg were run using both component surface temperatures extracted from thermal images (see Appendix C) and TUF3D generated surface temperatures to determine an optimal correction method that could be applied to all flights. It was determined that the method of correction that most closely agreed with the repeated data used TUF3D generated surface temperatures. SUMVeg is configured to run coupled with TUF3D and so the model geometry is similar, therefore it makes sense that the TUF3D surface temperatures generated with model forcing data observed for each site would work best with the SUMVeg model. 15-minute time steps from the beginning of each traverse were run for each of the Liberty Wells and White Sands flights (a total of 4 simulations) and the difference of each consecutive run was subtracted from t_1 (the first simulation representing the start of the traverse). For the Western

Springs site two simulations were run with a 20-minute time step to model the change in DBT from the start to end of the traverse. Figure 3.9 shows the difference between t_1 and the final time step t_f for each flight where the maximum change in DBT for each flight is observed. The change in DBT for each modelled time step used to create correction polynomials are shown in Appendix C.

Figure 3.9 a-f shows the modelled change in DBT for the Liberty Wells and White Sands sites. The model was run for $0^\circ - 55^\circ$ ONA in 5° steps and $0^\circ - 315^\circ$ in 45° steps to calculate a change over time for every point on the polar plots. The modelled change in DBT between the beginning of the traverse and the final modelled time step (45 minutes from the start) for LW12 suggests that the largest change in DBT is $\sim 1^\circ\text{C}$. These areas of largest change in DBT are found in the coolest regions of the polar plot at $\geq 50^\circ$ ONA. The modelled changes in DBT are very small for this flight and are within both the error range of the instrument and the standard deviation of the averaged DBT used to generate the observed polar plots, suggesting corrections are likely not needed for this flight. LW15 shows a maximum modelled change in directional brightness temperature of 1.27°C 45 minutes into the flight close to nadir. The polar plot of changing DBT indicate that the DBT was decreasing around nadir and along the north-south axis as the sun moves to the west. LW17 has the largest changes in DBT in the hot spot region, opposite the sun's position with a maximum magnitude of 2.49°C . This suggests the largest changes are expected to come from the cooling of sunlit walls and roofs.

The maximum change in temperature for WhS8 is centered on nadir, indicating that the model is predicting the largest temperature changes are associated with warming horizontal facets. The maximum change in temperature predicted for this flight was 3.69°C . During WhS12, the cool region begins to warm with the largest change in DBT a warming of 3.77°C . WhS17 shows the largest change in DBT as a cooling along the east-west axis, with the largest differences in nadir. This suggests that the roofs are expected to cool the most between 1700 and 1750 LAST. The maximum cooling for this flight is 3.1°C .

Figure 3.9g-i show the modelled change in DBT for the Western Springs site. Two model runs were performed for these flights as they were much shorter than the flights for the other sites. The difference of the model results were subtracted to produce the plots shown. The model was run for $0^\circ - 55^\circ$ ONA in 5° steps and $0^\circ - 340^\circ$ in 10° steps to calculate a change over time for every point on the polar plots for the Western Springs site. The modelled difference between the DBT at the start and end of the WS8 traverse suggest the largest change was a warming of $\sim 2^\circ\text{C}$ in the cool regions of the polar plot. Most of the modelled differences for this flight are $>1^\circ\text{C}$. The maximum predicted change in WS10 is a warming of $\sim 1.5^\circ\text{C}$. Most of the plot shows a warming of $>1^\circ\text{C}$ suggesting that all surfaces are warming during this time and all except west walls are heating at approximately the same rate. The modelled change in DBT for WS12 show small changes in DBT. The largest change is a warming of $\sim 0.9^\circ\text{C}$ at large off-nadir angles. These small changes in DBT suggest that a temporal correction is likely not necessary.

Correction polynomials were created by plotting the difference in DBT between each time step and t_1 for each ONA and view azimuth pair at each time step and fitting a curve to the plot. This created a curve that could be a linear, 2nd degree, or 3rd degree correction polynomial for each ONA and view azimuth pair that was sampled during the flights. The final correction polynomials can be found in the supplemental material.

Corrections were only considered necessary for LW15, LW17, WhS8, WhS12, WhS17, and WS8. Correction polynomials were generated from these modelled changes for all 8 azimuth angles for Liberty Wells and White Sands, and all 16 azimuth view angles for the Western Springs site, and each ONA sampled. Regression lines were fit to the curves to create polynomials which can be found in the supplemental material and polar plots representing each time step can be found in Appendix C.

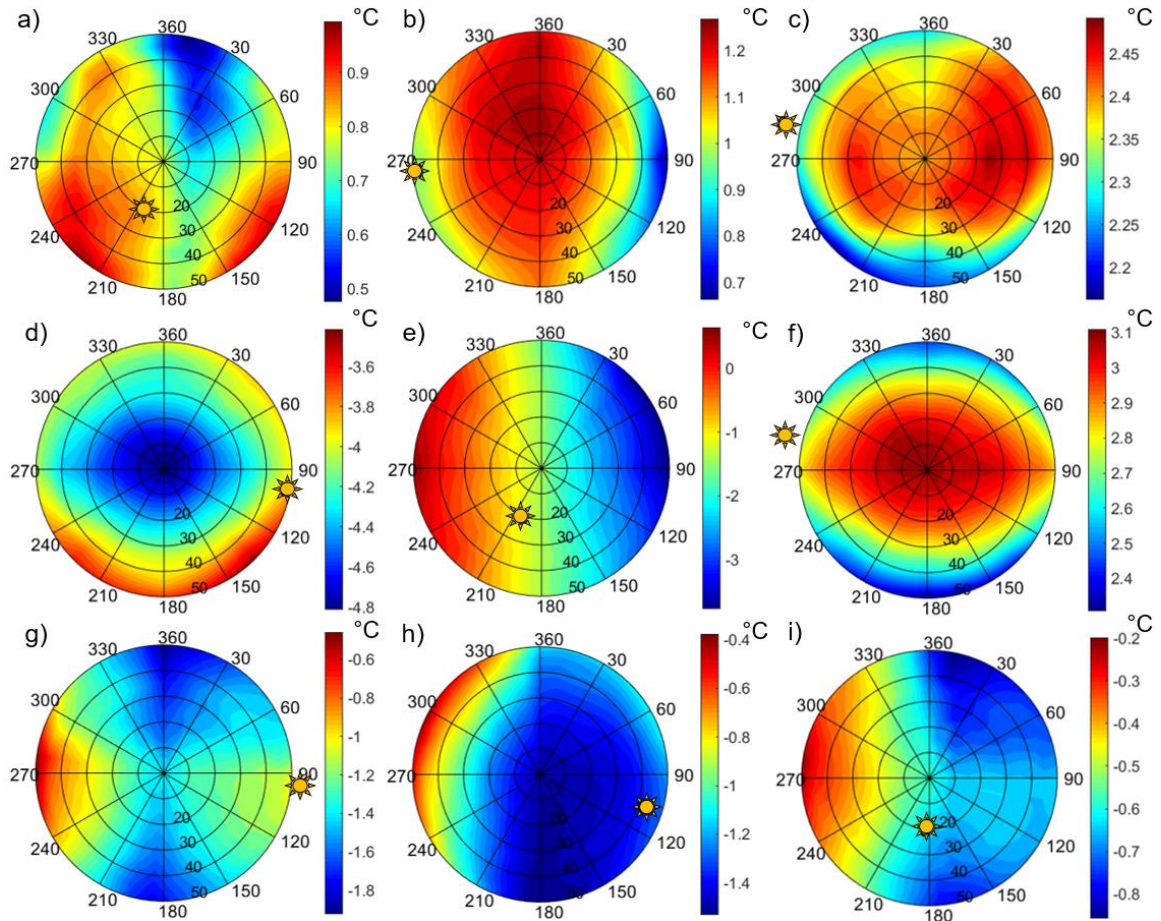


Figure 3.9 Modelled changes in directional brightness temperature, $t_1 - t_4$ from the start of the traverse to the end of the traverse for (a) LW12, (b) LW15, (c) LW17, (d) WhS8, (e) WhS12, (f) WhS17, and $t_1 - t_2$ for (g) WS8, (h) WS10, and (i) WS12. The polar plots were created by calculating at-sensor DBT for 15° FOV using SUMVeg coupled with the urban energy balance model TUF3D to calculate surface component temperatures. Solar position is denoted with a yellow sun symbol.

3.3.3 Comparison of Repeated Flight Lines

The flight plan for each study area incorporated some repeated flight lines to test for the change in surface temperature that may occur over each flight. The repeated section incorporated 4 flight lines that used the same off-nadir angle (45°) to sample each inter-cardinal direction. Figure 3.10 shows the comparison of beginning and end of traverse flight segments. A correction of the repeated data is compared to assess the accuracy of the temporal correction when one was considered necessary. Figure 3.10a confirms that a

correction for LW12 was not needed. The interquartile range matches very well and the difference in mean values is between 0.30-0.78°C. The largest change in mean DBT for LW15 was for the northeast and northwest view directions, the other view directions did not require a significant correction. The correction polynomials used moved the range of the northeastern and northwestern view direction temperatures up without shifting the other view directions much. There is a slight overcorrection for the southwest view direction, however the interquartile range still overlaps due to the large range of the first flight line. This is due to a lot of variability within the site geometry that caused large temperature ranges for certain view directions and will be discussed later in this chapter. The shifted interquartile range still overlaps well. Overall, the correction performed well. Larger corrections were needed for LW17, shown in Figure 3.10c. Here the corrections performed very well for all view directions except the northwest, where there is an overcorrection of 1.00°C. This is due to the spatial variability of the site being mostly divided north – south. Due to the airborne sampling method, the repeated data points are seeing the same surface directions but not necessarily the exact same areas, so spatial variability causes large changes for comparison. The mean values were between 0.18-0.79°C for the other view directions.

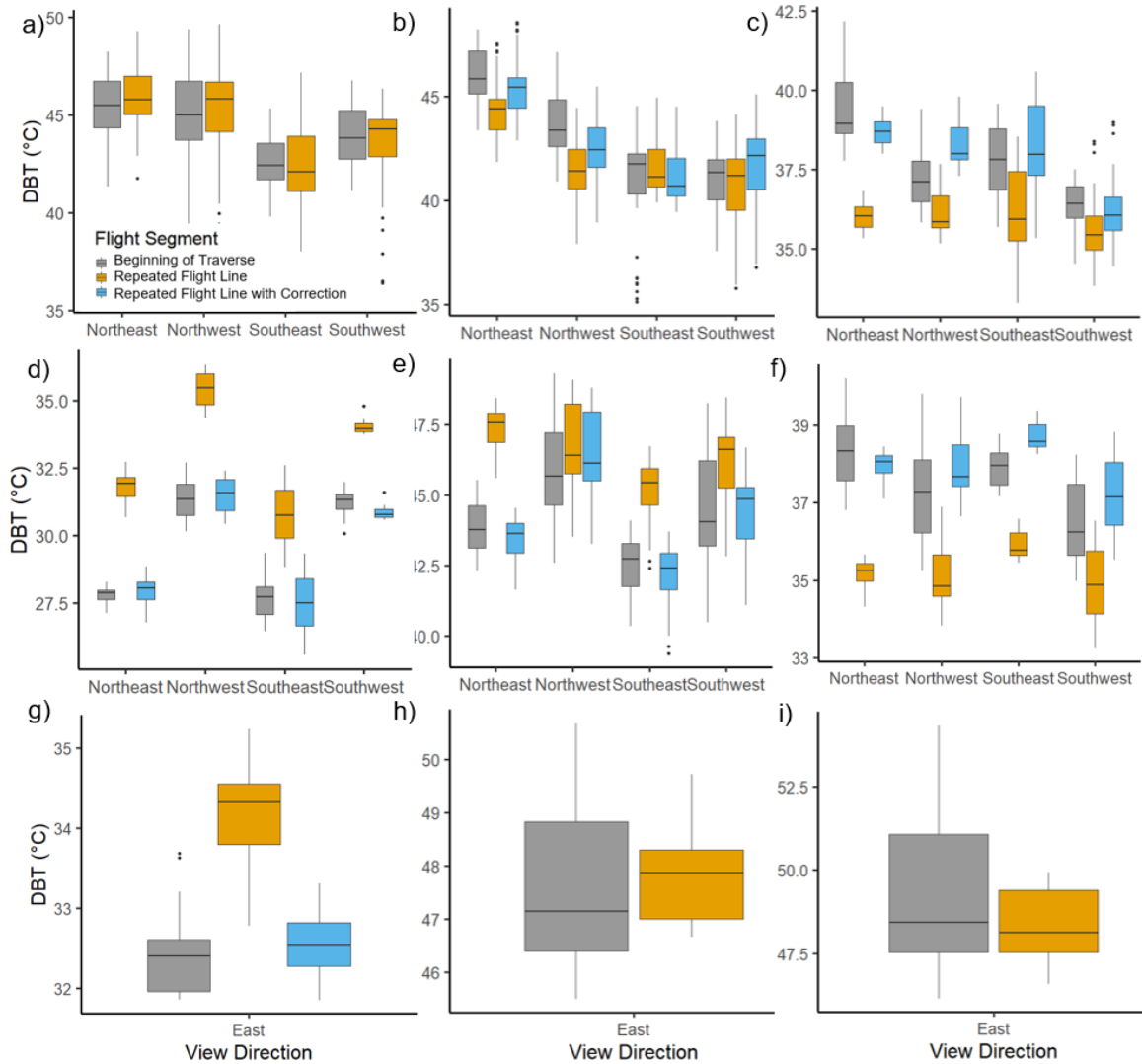


Figure 3.10 Results from the repeated flight legs for each of Flights (a) LW12, (b) LW15, (c) LW17, (d) WhS8, (e) WhS12, (f) WhS17, (g) WS8, (h) WS10, and (i) WS12. In each plot, directional brightness temperatures are plotted for the flight leg segment at the beginning of the airborne traverse, at the end of the traverse (repeated flight line) and the correction applied to the repeated section. Box and whiskers configured as in Figure 2.18.

The largest corrections were for WhS8. Figure 3.10d shows the temperature change from the beginning of the traverse to the repeated segment was very similar for all view directions, which implies the greatest change was likely horizontal surface temperatures. East walls experienced a change of 10°C during this traverse, but Figure 3.10d shows only a small change for westerly viewing azimuths which implies that sunlit walls are not

a large component of what the thermal imager is observing for White Sands. The correction performs well, moving the interquartile range of each view direction to overlap with the segment from the beginning of the traverse. The largest difference in mean temperatures between the beginning of the traverse and the corrected repeated flight line is 0.36°C for the northwest view direction. Corrections were needed for the solar noon flight of White Sands, unlike the solar noon flight of Liberty Wells. The largest corrections were needed for the northeast and southeast view directions due to the warming of south-facing walls as the sun reaches solar maximum. The largest difference in mean temperatures between the beginning of the flight and the corrected repeated flight line was 0.66°C . WhS17, the later afternoon flight for the White Sands neighbourhood also shows a need for a temporal correction. The DBT decreased consistently from the beginning of the flight to the repeated time, which was expected from decreasing component temperatures. The temporal correction polynomial does a good job of increasing the repeated temperatures to better match the data from the beginning of the traverse, however the correction does overcorrect slightly for all view directions except the northeast view azimuth. The largest of these overcorrections created a difference of 0.8°C in the mean DBT.

The repeated flight segment for the Western Springs neighbourhood was for an easterly view azimuth and 5° ONA, the closest to nadir that was sampled. Figure 3.10g-i shows the comparison between the start and end of the traverse for the Western Springs site. The difference between the mean DBT from the start of the traverse to the repeated flight leg is $\sim 1.5^{\circ}\text{C}$, which is large enough to require a correction. The correction used fits well, reducing the range and IQR of the repeated leg to more closely match that from the beginning of the traverse and reducing the difference in mean DBT to 0.07°C . The difference between the mean DBT for the beginning of the traverse and repeated segment is 0.22°C for WS10. The range and IQR also completely overlap. This observed difference was smaller than the modelled difference in DBT and indicates a temporal correction is not needed. The difference between the start and end of the traverse near nadir for WS12 is small. The range and IQR overlap for both flight segments and the difference in mean DBT is 0.84°C , which confirms a correction was not needed for this

flight. Using this method of correcting directional brightness temperatures for temporal effects, the late afternoon flights were the most difficult to fit good correction polynomials. Table 3.1 shows a summary of flights requiring a temporal correction of DBT.

Table 3.1 Magnitude of maximum temporal correction applied to each flight. No value indicates a correction was not applied to that flight.

Flight	Magnitude of Maximum Correction Applied (°C)
LW12	-
LW15	1
LW17	2
WhS8	4
WhS12	2.5
WhS17	3
WS8	1.2
WS10	-
WS12	-

3.4 Effective Anisotropy

3.4.1 Polar plots

In this section atmospherically and temporally corrected polar plots of DBT are presented and analyzed. The polar plots were generated by plotting the averaged mean directional brightness temperatures and then drawing contour lines around the points. Figure 3.11 shows the data points provided to create each polar plot. Polar plots were generated in Matlab R2018a. The Matlab program plots isobands using a marching squares algorithm to generate contours from the DBT matrix. No more than 20 contour lines are used. The exact number and interval is determined by the algorithm based on $T_{B,max}$ and $T_{B,min}$ and are always divisible by 2 or 5. The marching squares algorithm creates a contour plot by creating a contour grid one cell smaller than the input grid with each input grid value represented as the corner of each contour grid cell. The algorithm then moves clockwise around each contour cell checking if the contour level being checked falls along a contour

cell edge. Exact contour lines are located using linear interpolation along the boundary of each cell in the DBT matrix and the space between contour lines is filled based on the colour bar(MathWorks, 2020).

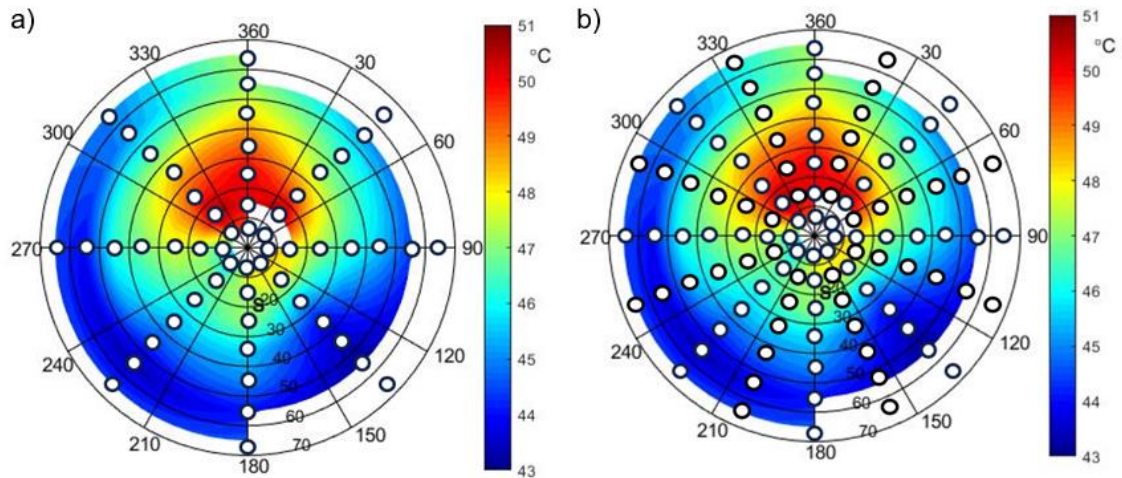


Figure 3.11 Sample polar plot depicting the data points as white circles. Observational data were collected for 15° - 55° ONA in 10° bins and 0° - 315° azimuth angles in 45° bins as well as partial coverage of 5° and 65° ONA.

Figure 3.12 shows polar plots with only observational data plotted. Blank areas represent missing data. These plots reveal the difficulty of obtaining observations at nadir with the sampling methodology used. Sampling was more successful at 5° ONA, so the 5° off-nadir bin incorporated all observations made at angles from 0 - 5° off-nadir. The polar plots are truncated at 55° ONA as complete coverage of 65° was not achieved for all plots. A consistent maximum ONA is important because it affects the values of effective anisotropy; the DBT at large ONA away from the hot spot tends to decrease with increasing ONA and therefore larger ONA increase effective anisotropy.

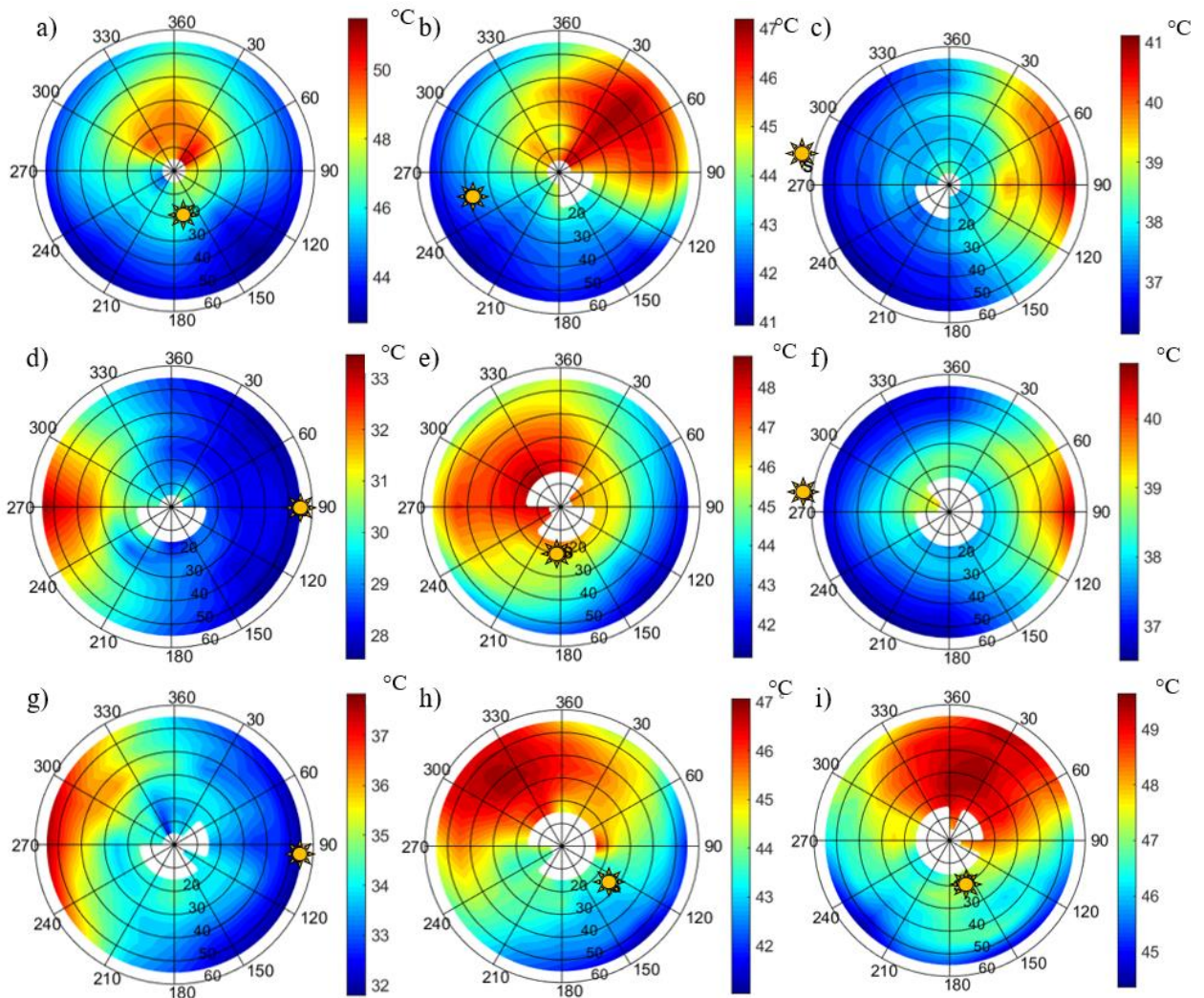


Figure 3.12 Polar plots of temporally corrected observed DBT for a) LW12, (b) LW15, (c) LW17, (d) WhS8, (e) WhS12, (f) WhS17, (g) WS8, (h) WS10, and (i) WS12. The solar position is noted with a yellow sun symbol and the maximum effective anisotropy (Λ_{Max}) is noted for each flight.

The nadir DBT is a useful reference measure for thermal anisotropy analysis (Vinnikov et al., 2012; Lagouarde et al, 2010) so to provide a complete polar plot it was estimated in one of two ways. For flights that had a 5° DBT for every azimuth angle, nadir DBT was calculated as the average of all 5° off-nadir angle brightness temperatures. This method can be used as an approximate nadir value because the difference in DBT for 0° – 5° off-

nadir angles is often not large, and when data exist for every sampled azimuth angle, the nadir value is expected to be close to the value that all 5° samples converge on. For flights that did not have full coverage of 5° off-nadir, the nadir DBT value was linearly interpolated by plotting DBT from -25° to +25° off-nadir angles along select opposing azimuth angles and fitting a line of best-fit to the curves. This interpolation was performed with 4 opposing azimuth pairs for the Liberty Wells and White Sands flights (N-S, NE-SW, E-W, NW-SE) and 8 pairs for the Western Springs flights as seen in Figure 3.11. The nadir brightness temperatures interpolated by each pair of opposing angles were then averaged to represent the nadir brightness temperature for each flight.

Completed polar plots that incorporate the filled-in nadir DBT are shown in Figure 3.13. Three measures of the overall anisotropy are assessed (Table 3.2). These are: the maximum effective anisotropy (Λ_{Max}), which is the difference between the maximum and minimum DBT ($T_{B,max} - T_{B,min}$) and is noted on the plots, the interquartile range (IQR), and the difference between the 95th ($T_{B,95}$) and 5th ($T_{B,5}$) percentiles (Λ_{95-5}). The latter two measures reduce the sensitivity of the anisotropy estimate to outliers.

The major features of the polar plots are a hot spot region that consists of an area of warmer DBTs and an area of relatively cooler DBTs that are most evident in the direction opposite the solar azimuth and which extend to a broader range of azimuth view angles at larger off-nadir angles. Because the hot spot region is created by sunlit surfaces, both horizontal and vertical, the location on a polar plot is approximately opposite that of the solar position (indicated by a yellow sun symbol) and is found at larger ONA for times of day with a large solar zenith angle. For the purpose of this analysis, the hot spot is defined as a DBT greater or equal to the 95th percentile ($T_{B,95}$). Table 3.3 gives a summary of the hot spot characteristics for each flight. The hot spot is described by the size in steradians of the area occupied by the hot spot within a unit circle. To find this value the length (difference between maximum and minimum ONA covered by the hot spot) and width (maximum azimuth angles covered by the hot spot) were substituted into the equation:

$$\Omega_{hot\ spot} = \frac{A}{r^2} = \frac{\pi * l * w}{r^2} \quad (3.1)$$

where $\Omega_{hot\ spot}$ is the solid angle of the hot spot in sr, l is the ONA covered by the hot spot in degrees, w is the maximum range of azimuth angles covered by the hot spot, and r is the radius of a unit circle (1).

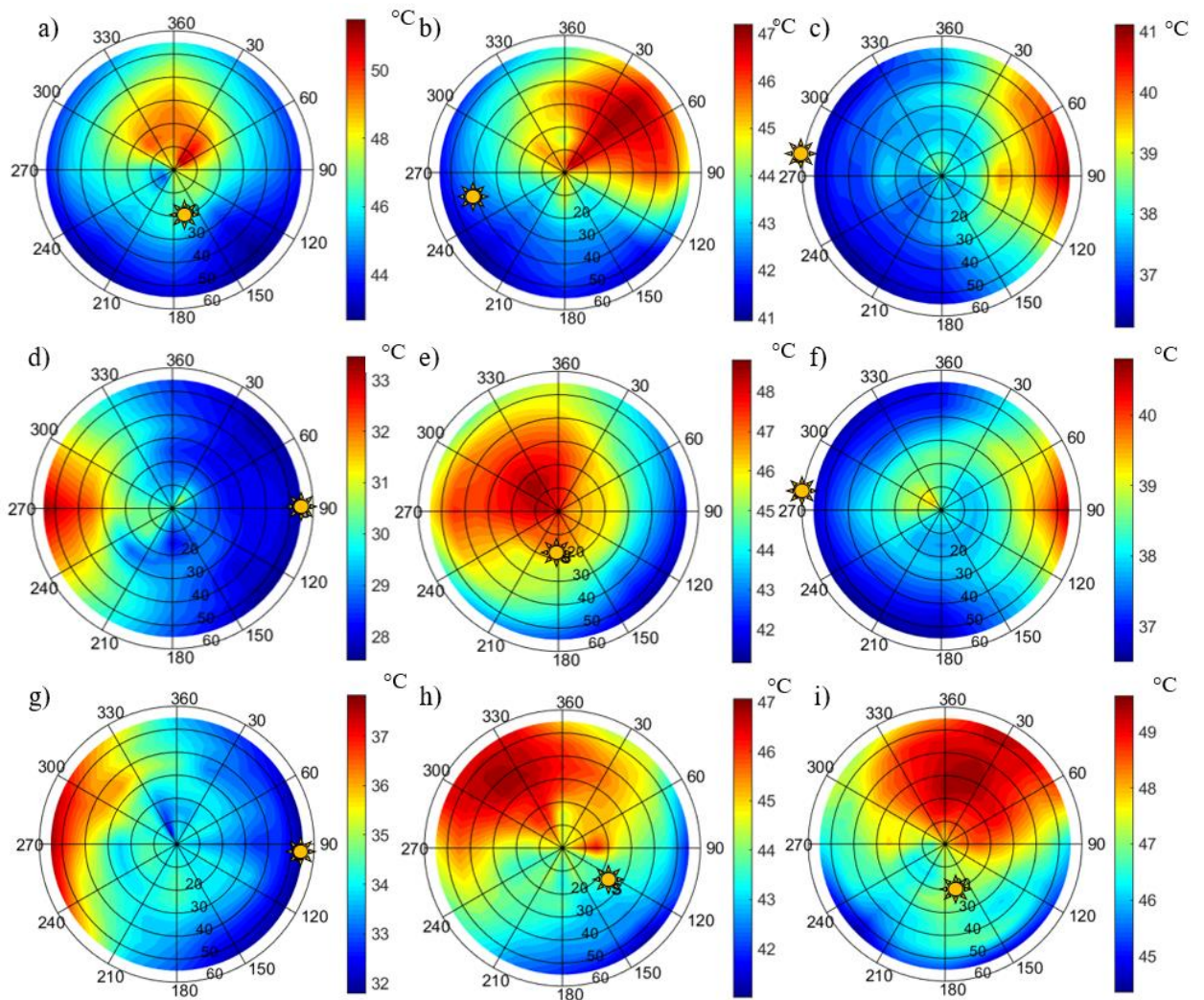


Figure 3.13 Complete polar plots of (a) LW12, (b) LW15, (c) LW17, (d) WhS8, (e) WhS12, (f) WhS17, (g) WS8, (h) WS10m and (i) WS12. The polar plots include observational data points as well as interpolated nadir points. The solar position is noted with a yellow sun symbol and the maximum effective anisotropy (Λ_{Max}) is noted for each flight.

Table 3.2 Measures of effective thermal anisotropy for each of the flights. All values in the chart are in ($^{\circ}\text{C}$).

	LW12	LW15	LW17	WhS8	WhS12	WhS17	WS08	WS10	WS12
$T_{B,max}$	50.15	47.21	41.11	33.46	48.81	40.81	37.85	47.07	49.64
$T_{B,min}$	42.67	40.92	36.13	27.53	41.15	36.50	31.78	41.01	43.53
Λ_{Max}	7.48	6.29	4.98	5.93	7.66	4.31	6.06	6.06	6.11
$T_{B,95}$	49.66	47.12	39.98	32.51	48.46	39.70	36.51	46.62	49.41
$T_{B,5}$	42.80	41.39	36.38	27.74	42.10	36.64	32.09	42.10	45.02
Λ_{95-5}	6.86	5.73	3.60	4.76	6.36	3.06	4.42	4.52	4.38
Q1	45.01	42.84	37.31	28.53	44.84	37.47	33.51	43.64	46.63
Q2	46.43	44.26	37.75	29.06	46.22	38.06	34.10	44.43	47.31
Q3	48.34	45.47	38.27	30.36	47.40	38.53	34.56	45.34	48.51
IQR	3.33	2.64	0.96	1.83	2.57	1.06	1.05	1.70	1.88

* Q1 is the first quartile, Q2 the second quartile and Q3 the third quartile.

Table 3.3 Hot spot characteristics for each polar plot. The solid angle is based on the area subtended by the hot spot on a unit circle.

Flight	Center ONA ($^{\circ}$)	Center Azimuth	Solid Angle (sr)
LW12	15	North	33.34
LW15	25	Northeast	15.08
LW17	55	East	18.05
WhS8	55	West	14.08
WhS12	5	Northwest	33.99
WhS17	55	East	13.81
WS8	55	West	18.05
WS10	45	Northwest	19.61
WS12	25	North-northeast	24.96

Liberty Wells

The first flight over the Liberty Wells site was flown at solar noon (LW12). The hottest region, or the hot spot region, of the polar plot is centered around 15° ONA at a northerly

view azimuth and covers a solid angle of approximately 33.34 sr for this flight. At solar noon, the horizontal surfaces receive the maximum direct solar radiation. The solar zenith angle at noon for this location at this time is approximately 20° from nadir so that south facing vertical facets are differentially warmed, causing the hot spot to be in a more northern position rather than directly at nadir. The coolest regions of the polar plot are located at large ONA opposite the hot spot region. These cool regions are caused by shaded facets and shadows cast on horizontal surfaces. At solar noon, the shaded facets are mostly restricted to shaded walls causing the coolest regions to be observed at large ONA. The largest anisotropy is typically observed at solar noon (Voogt and Oke, 1998; Lagouarde et al., 2004) due to the large range of DBT caused by very hot sunlit surface temperatures and cool, shaded walls. This pattern is true for the Liberty Wells site with $\Lambda_{\text{Max}} = 7.48^\circ\text{C}$ and $\Lambda_{95-5} = 6.86^\circ\text{C}$. The difference between Λ_{Max} and Λ_{95-5} is 1.62°C which suggests that there were large outliers for this flight, particularly in the hottest regions of the plot where the difference between $T_{B,\text{max}}$ and $T_{B,95}$ is 0.62°C . This suggests that there are no large outliers in this polar plot.

LW15 was flown 3 hours after LW12 and shows an easterly shift in the hot spot region as well as a stretching of this region from nadir out to larger ONA. The hot spot region of LW15 is located at a northeastern view azimuth between 5° to 35° off-nadir, covering a solid angle of 15.08 sr. This hot spot is smaller in area than at solar noon however it is stretched over more off-nadir angles. This is expected as the solar position moves from a slightly southern position close to nadir to a west-southwestern position at approximately 40° zenith angle. The coolest region also shifted with the movement of the sun; however, it follows the same pattern of the largest cool area opposite the hot spot region and for large ONA. From Table 3.2, $T_{B,95}$ was reduced by 2.78°C and $T_{B,5}$ was reduced by 1.47°C which means that the hottest surfaces were cooling faster than the shaded regions of this site. This led to a 1.31°C change in Λ_{95-5} for this 3-hour gap in sampling. The difference between Λ_{Max} and Λ_{95-5} is 0.56°C , suggesting outliers were not a major factor of this flight.

In the late afternoon (1700 LAST) the sun is positioned at a low elevation, so that west-facing vertical facets receive direct solar radiation at a small angle of incidence but with

most other sunlit surfaces receiving significantly less solar radiation. The low solar elevation results in large shadows and allows horizontal surfaces to begin to cool, causing the large cool region on the western half of the polar plot observed in Figure 3.13c. LW17 was sampled 2 hours after LW15. In this time the hot spot continued to stay approximately opposite the solar position and is now centered at an eastern view azimuth at 55° off-nadir covering a solid angle of 18.05 sr. The hot spot for LW17 is smaller than LW12 but larger than LW15, however it is likely that the hot spot size is underestimated due to the truncation of the polar plot at 55° ONA. The $T_{B,95}$ continued to cool, decreasing by 9.93°C while $T_{B,5}$ cooled by 6.07°C . After solar noon, $T_{B,95}$ cooled faster than $T_{B,5}$ which reduced the observed thermal anisotropy as the afternoon progressed. The difference between Λ_{Max} and Λ_{95-5} is 1.38°C , suggesting there were larger outliers for this flight, particularly between $T_{B,\text{max}}$ and $T_{B,95}$ which show a difference of 1.13°C . The thermal anisotropy (Λ_{95-5}) for the LW17 flight was 2.12°C smaller than LW15 and 3.60°C smaller than LW12.

The change in $T_{B,95}$ was larger than $T_{B,5}$ between each flight, indicating the hottest surfaces heat or cool more than the shaded, cooler surfaces that are closer to air temperature. This was an expected pattern as the largest thermal anisotropy, and therefore the largest temperature range, is expected to be observed at solar noon.

White Sands

The White Sands site was sampled three times, once in the morning, at solar noon, and then once in the late afternoon. This provided an evolution of DBT and thermal anisotropy over an entire day. The first flight, WhS8 was flown at 08:00 LAST. The hot spot region during this flight is centered at 55° ONA at a western view azimuth. During the morning, east walls are receiving direct solar radiation as the sun is at a large zenith angle. This causes the hot spot to be located at a large ONA, indicating more vertical facets are sunlit than horizontal facets. At this time, the hot spot covers a solid angle of 14.08 sr. This low solar elevation also causes large shaded regions, causing the coolest areas of the polar plot to take up a large region of the plot with the coolest areas opposite

the hot spot region. The difference between Λ_{Max} and $\Lambda_{95.5}$ is 1.16°C , with the difference between $T_{B,\text{max}}$ and $T_{B,95}$ accounting for this difference.

For WhS12 the hot spot is centered on 15° ONA with a northwestern view azimuth covering a solid angle of 33.99 sr. This is approximately a 2.5x increase from the morning hot spot size, however the polar plot truncation at 55° ONA means that the WhS8 hot spot is likely underestimated given its position at edge of the polar plot. From Table 3.2 $\Lambda_{\text{Max}} = 7.66^{\circ}\text{C}$ and $\Lambda_{95.5} = 6.36^{\circ}\text{C}$ with a difference of 1.3°C between the two assessments of thermal anisotropy. In this case, there is an anomalously cool $T_{B,\text{min}}$ (0.95°C cooler than $T_{B,5}$) likely caused again by the spatial variability of the site and the sampling method under or over sampling one region over another. When comparing WhS8 and WhS12, $T_{B,95}$ increased by 15.95°C and $T_{B,5}$ increased by 14.36°C . This led to a change in $\Lambda_{95.5}$ of 1.6°C for a change in solar elevation of 34.88° .

Similar to LW17, the hot spot of WhS17 is considerably smaller than it was at solar noon, covering a solid angle of 13.81 sr. This is similar in size as the morning traverse, however the hot spot observed for WhS8 covered more off-nadir angles due to the slightly larger solar elevation during the WhS8 traverses with LW17 and WhS8, the hot spot is likely underestimated due to the truncation of the polar plots to 55° ONA. The $\Lambda_{95.5}$ decreased by 3.3°C due to a decrease in $T_{B,95}$ of 8.76°C and a decrease of $T_{B,5}$ of 5.46°C for a solar elevation change of 45.21° .

As with the Liberty Wells site, $T_{B,95}$ experienced larger changes between flights than $T_{B,5}$. An interesting observation, however, was the much larger change in DBT between WhS8 and WhS12 compared to WhS12 and WhS17 despite the late afternoon flight occurring at a larger solar zenith angle than the morning flight.

Western Springs

Three flights were flown for the Western Springs neighbourhood at 08:00 LAST, 10:00 LAST, and 12:00 LAST. WS8, the first flight flown for this site, observed conditions similar to WhS8. Figure 3.13d shows the hot spot is located at an easterly view azimuth and occupies a solid angle of approximately 18.05 sr. Like LW15, allowed for a closer

examination of the evolution of observed DBT in the afternoon, WS10 allows for that same analysis during the morning. The change in solar elevation during the two-hour period between WS8 and WS10 was 23.62° and over this time Λ_{95-5} changed by 0.1°C . The consistent thermal anisotropy observed between these flights is due to the similar change in both $T_{B,95}$ and $T_{B,5}$ which increased by 10.11°C and 10.01°C respectively. The hot spot shifted to a more northwesterly view azimuth during this time and slightly increased in size to 19.61 sr. This followed the trend shown by LW15 that shows a gradual increase in hot spot size the closer the solar zenith is to solar noon. This is confirmed by the hot spot observed for WS12 which is 5.35 sr larger than the hot spot observed for WS10 and 6.91 sr larger than the hot spot observed for WS8. The hot spot of WS12 is located at a north-northeasterly view azimuth centered at a 25° ONA. The change in Λ_{95-5} is a decrease of 0.14°C . This decrease is unexpected and likely due to variability in the data causing a slight decrease in the change of $T_{B,5}$. The expectation would be for the thermal anisotropy to increase slightly at solar noon. Overall, the trend for this site suggests that both $T_{B,95}$ and $T_{B,5}$ change at a similar rate, thus the magnitude of thermal anisotropy remains approximately constant throughout the morning.

Comparison Between Flights

The hot spot for the morning flights of White Sands and Western Springs look quite similar in size and shape, with the center of the hot spot located at a westerly view azimuth for both flights. The hot spot region is slightly longer for the White Sands site, extending from 35° to 55° off-nadir compared to the hot spot for WS8 which only extends from 45° to 55° off-nadir. The hot spot for WhS8, however, is 3.97 sr smaller than that of WS8. The results of $T_{B,max}$ and $T_{B,95}$ for the morning and solar noon flights are similar, suggesting the differences in wind speed observed between the study days and the morning cloud cover observed for 12 July did not contribute to large differences in surface warming.

The largest effective anisotropy was expected to be observed at solar noon for the White Sands site because it is the least densely built neighbourhood with a large λ_{tree} . The observed anisotropy at solar noon is very similar for the Liberty Wells and White Sands

neighbourhoods. When comparing Λ_{Max} , White Sands did have a slightly higher anisotropy, however, for $\Lambda_{95.5}$, Liberty Wells having a larger $\Lambda_{95.5}$ by 0.5°C , suggesting the thermal anisotropy for both sites is very similar. The anisotropy for Western Springs at solar noon is less than the other sites, which was expected as there would be less temperature contrast due to decreased tree canopy coverage. The IQR for the solar noon flights is slightly larger for the Liberty Wells site than the White Sands site by 0.76°C , with the Western Springs site having the smallest IQR. The hot spots for both LW12 and WhS12 are similarly sized and are centered at 15° off-nadir although the hot spot of WhS12 extends to 5° off-nadir in the western view azimuth and to 25° off-nadir in the northwestern view azimuth whereas the LW12 hot spot is shifted to the northeast. The biggest difference between the Liberty Wells site and White Sands site at solar noon is the shift of the middle of the hot spot from a northerly azimuth during LW12 to northwest for WhS12. The hot spot for WS12 however, was centered on a larger ONA despite being at the same solar time as the other flights. The solid angle subtended by the hot spot of WS12 is also smaller than the hot spots of the other two sites.

The anisotropy is lowest for Liberty Wells and White Sands for the 1700 LAST flights as many surfaces are shaded and cooling. The lowest Λ_{Max} and $\Lambda_{95.5}$ were observed for the White Sands site, although the results for the Liberty Wells site are very similar with a $<1^{\circ}\text{C}$ difference in anisotropy. The IQR for these late afternoon flights are very similar with a difference of only 0.1°C . The hot spot in the late afternoon is smallest for WhS17, located at an easterly view azimuth and 55° ONA. In contrast, it covers three observation? points on the LW17 polar plot, ranging from an eastern azimuth between 45° - 55° off-nadir and a northeastern view azimuth at 55° . The solid angle subtended by the hot spot of WhS17 is 4.24 sr smaller than the hot spot for LW17. The hot spot is similar for both sites at both flight times which was expected as the landcover fractions were very similar for both sites.

3.4.2 FLIR T650 vs Heitronics KT15.82 Radiation Pyrometer

The Heitronics KT15.82 radiation pyrometer provides an independent measure of directional brightness temperatures to compliment the FLIR generated dataset. Results from each instrument were compared to determine how well the datasets match for future use. Based on the optimization described in Appendix A, temperatures from a circular area on the thermal images ($IFOV_{KT15.82}$) that matched the location of the KT15.82 FOV were extracted and averaged. These averaged DBT were then used to create a polar plot from thermal imager data that corresponds to the KT15.82 observations. Average temperatures for each view azimuth and ONA were plotted on polar plots for flights LW12 and WhS12 for each instrument and are shown in Figure 3.14. The overall pattern of hot spot and cool regions is similar in both datasets however the hot spot region of the polar plot created by the Heitronics KT15.81 appears to be hotter relative to the FLIR for both neighbourhoods. Difference polar plots (Figures 3.14c and f) show no clear pattern suggesting that the differences in average DBT are caused by noise from one of the instruments rather than a hot or cold bias from an instrument.

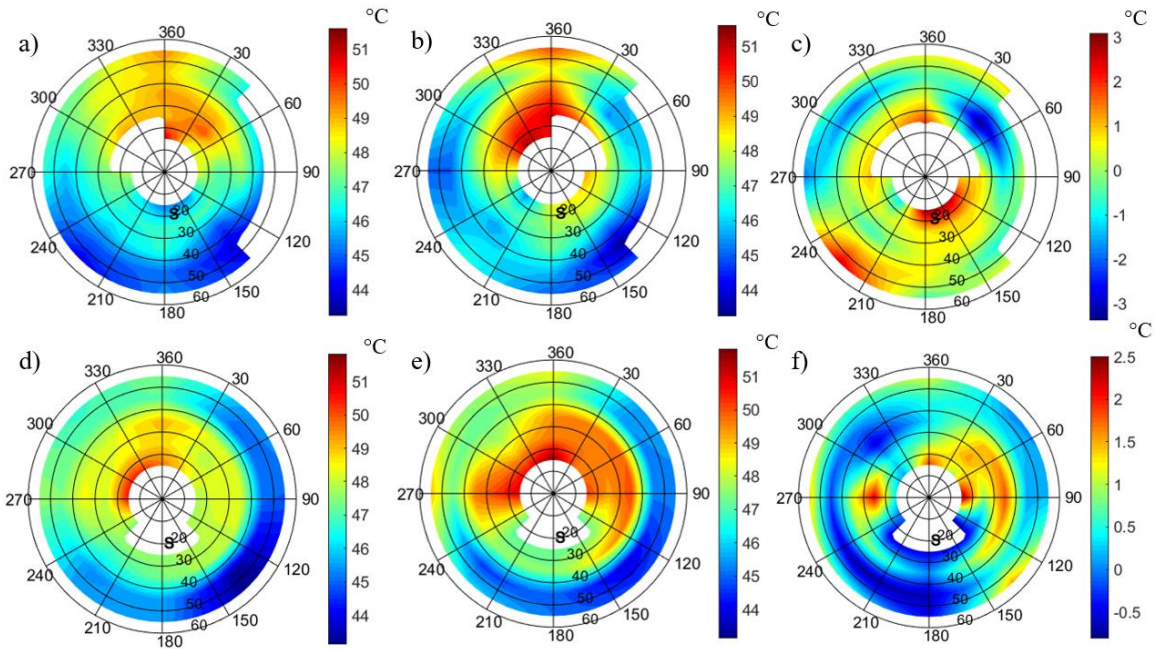


Figure 3.14 Polar plots produced for the FLIR T650 and Heitronics KT15.82 instruments and their differences for (top row) LW12 and bottom row (WhS12). (a) and (d) are FLIR T650, (b) and (e) are Heitronics KT15.82 LW12, (c) and (f) are differences expressed as KT15.82-FLIR T650. Solar position is denoted with a black S.

Table 3.4 shows a statistical comparison of the different polar plots. For the Liberty Wells site, the Heitronics shows a larger Λ_{Max} due to the combined larger $T_{B,\text{max}}$ and lower $T_{B,\text{min}}$. The differences between the Λ_{95-5} generated by each instrument, however, are quite small as is the difference between IQR for this flight. This larger range from the Heitronics instrument is likely noise, as the instrument response rate was set to 100 ms. This was deliberately chosen in order to better resolve surface temperature variability from the moving observation platform; however, it results in a slight loss of accuracy (temperature resolution $\pm 0.15^\circ\text{C}$ which gives a maximum possible error range of $\pm 0.65^\circ\text{C}$ (Heitronics, 2004)). For the WhS12 flight the difference between Λ_{Max} created from the two datasets is more similar, with a difference of 0.36°C . This measure of anisotropy is more similar between the two datasets because the Heitronics instrument provided a similar $T_{B,\text{min}}$ as the FLIR as opposed to the results for LW12. The difference between $T_{B,95}$ and $T_{B,5}$ shows the same pattern of the Heitronics dataset being warmer. This

indicates the differences observed during this flight are not outliers and, while differences due to sampling noise from the Heitronics are likely affecting this flight as well, the warmer shift of the Heitronics suggests that the projected $IFOV_{KT15.82}$ might not match as well for this flight. The instruments were removed from the mount each day which introduces the possibility of slight shifts in overlapping IFOV for both instruments.

Table 3.4 Comparison of the FLIR T650 and Heitronics KT15.82 generated polar plots. All values in the chart are in ($^{\circ}\text{C}$).

Instrument	Heitronics KT15.82		FLIR T650		Heitronics KT15.82 - FLIR T650	
	LW12	WhS12	LW12	WhS12	LW12	WhS12
$T_{B,max}$	51.62	51.83	51.03	50.68	0.59	1.14
$T_{B,min}$	43.25	43.92	44.01	43.13	-0.77	0.78
Δ_{Max}	8.37	7.91	7.02	7.55	1.35	0.36
$T_{B,95}$	51.06	51.10	49.98	50.54	1.08	0.56
$T_{B,5}$	44.96	44.72	44.10	43.36	0.86	1.36
Δ_{95-5}	6.09	6.37	5.88	7.18	0.22	-0.81
Q1	45.87	46.28	45.74	45.72	0.13	0.56
Q2	47.53	47.67	46.90	47.72	0.63	-0.05
Q3	48.60	49.72	48.33	48.45	0.27	1.27
IQR	2.72	3.43	2.59	2.73	0.13	0.71

A recommendation for future work is to optimize the $IFOV_{KT15.82}$ separately for each site. Figure 3.15 shows a short time series of the difference between two DBT that are based on projected $IFOV_{KT15.82}$ with 50% overlap in the IFOV on the FLIR imagery. The time series demonstrates the effect of the spatial variability within a single image for a 12° IFOV. The differences in average DBT created by these two test $IFOV_{KT15.82}$ can be as large as 3°C . This large variability in surface temperature over a small area is likely caused by the large tree canopies creating a lot of temperature contrast between the large pockets of cool tree canopy temperature and very hot impervious surfaces. The implication of this is that doing an exact match of the Heitronics IFOV and $IFOV_{KT15.82}$

might be difficult, but the comparison of polar plots suggests comparing entire flight lines will smooth some of that variability and Heitronics generated noise.

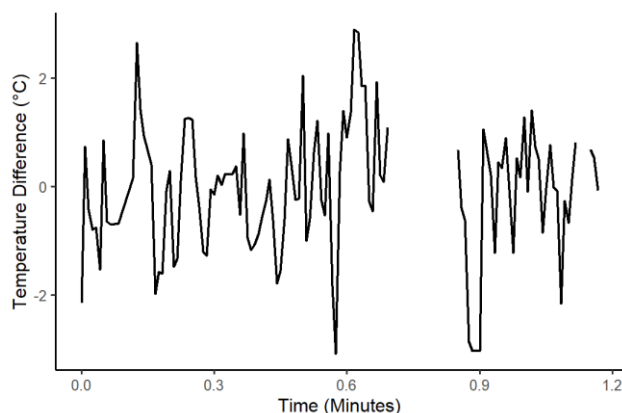


Figure 3.15 Difference in DBT between two overlapping test projected IFOV_{KT15.82} extracted from FLIR imagery. Time is displayed in decimal minutes from the start of the flight line.

3.4.3 Off-nadir versus Nadir Temperatures

Thermal anisotropy may also be analyzed by plotting the difference between the nadir and off-nadir temperatures for off-nadir angles taken at select view azimuth angles. This allows for different study days with similar conditions to be compared as differences are being compared rather than absolute temperatures. This analysis can also be useful to satellite remote sensing applications, as understanding the relationship between ONAs and nadir at different times of day and view azimuths helps in correcting land surface temperatures for anisotropic effects.

Figure 3.16 shows the results of this comparison of anisotropy. The principal solar axis refers to the axis in-line with the azimuth of the sun's position, whereas the perpendicular solar axis is the axis perpendicular to the principal solar axis. The hotspot is located along the principal solar axis and is observed when the instrument is positioned such that the sun is behind the observer, capturing sunlit walls as well as sunlit horizontal facets. For

the solar noon flights, the hotspot is close to nadir as the sun is at a small zenith angle. The change in temperature increases sharply from nadir near the hotspot, with LW12 exhibiting the largest increase in brightness temperature before sharply reducing at larger ONA. The WS12 flight shows a larger hot spot, extending to much larger ONA than the other two flights. LW12 represents the Liberty Wells site at solar noon, which has similar building cover as Western Springs, represented by WS12, but significantly more vegetation cover. This increase in vegetation reduces the hot spot region of the polar plot, as was shown by Lagouarde et al., (2004). WhS12 shows the most reduced difference between $T_{B,max}$ and $T_{B,nadir}$. From Figure 3.16c shows the relationship between vegetation and magnitude of anisotropy because WS12 has the least amount of tree-canopy cover and shows the most reduced negative amplitude. This indicates that WS12 does not have as large a $T_{B,min} - T_{B,nadir}$ as either of the sites with more tree-canopy coverage. The cooler region of the plots show a relationship between vegetation cover and magnitude of anisotropy with the site with the least amount of tree-canopy cover having the most reduced negative amplitude. The perpendicular solar plane of the solar noon flights shows similar patterns where the largest decrease in temperature is observed for the site with the least building cover. Interestingly, unlike the Liberty Wells site, the White Sands site does not show a symmetric decrease in temperature. This suggests that not only are the west-facing facets much more shaded or covered by vegetation compared to the other sites, the east-facing facets cool slower than the Liberty Wells site. Table 3.3 shows the percentage of walls obstructed by vegetation for each site and as it shows, there is a higher percentage of wall covered by large shrubs or tree-canopies for the White Sands site than the other two. This is true for all wall orientations within the site. The largest change in off-nadir to nadir temperature is observed for White Sands along the perpendicular solar plane, not the principal solar plane, affirming the importance of sampling both planes.

In Figure 3.16a and 3.16b, the morning flights show a very similar pattern of off-nadir – nadir temperatures and these differences are the same but opposite as you move towards or away from the solar position. This is likely because the shaded surfaces are very cool from nighttime cooling, but the sunlit surfaces have had a chance to warm, causing a similar deviation from nadir. The perpendicular solar plane does not show large

deviations from the nadir temperature. LW15 was flown during a similar solar zenith angle; however, it was sampled in the afternoon. This flight, having been flown in the afternoon after surfaces have had a chance to heat and then begin to cool, shows a larger difference between nadir and the cool region of the plot than the morning flights shows. This is partly because the hot spot is more reduced and closer to nadir than for the morning flights despite the similar solar angle. LW15 has reduced temperatures along the perpendicular solar plane because of the movement of the sun in the northern hemisphere causing the sun to be in a slightly southern position in the early afternoon, shifting the hotspot slightly to the north. The afternoon flights (Figure 3.16e and f) show an interesting pattern where the nadir hot spot has a much larger deviation from nadir than the cool region along the solar plane. This is likely because unlike the morning flights, the shaded surfaces have had some degree of warming as air temperatures have steadily increased all day warming the shaded areas. LW17 has a slightly hotter hot spot than WhS17 but the coolest temperatures are similar for each flight, giving LW17 a slightly larger thermal anisotropy. The spike in temperature observed for the WhS17 site near nadir along the principal solar plane can also be seen in the matching polar plot in Figure 3.13 to the western side of nadir. This spike is also seen in the perpendicular solar plane north of nadir and is smaller, but present, along the perpendicular solar plane of WhS12.

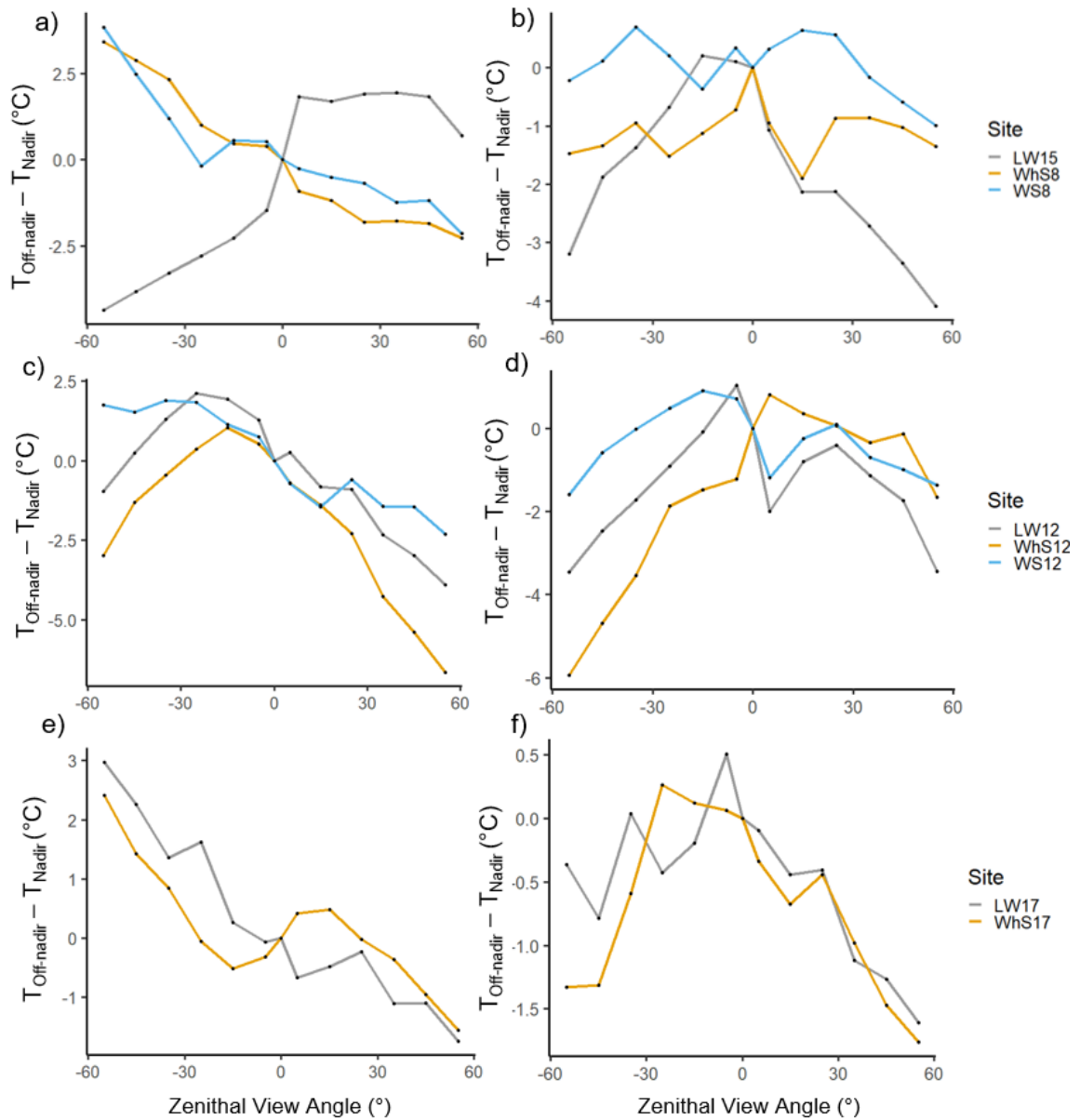


Figure 3.16 Difference of off-nadir and nadir temperatures for a) morning flights (WhS8 and WS8) and LW15 along the principal solar plane, b) morning flights and LW15 along the perpendicular solar plane, c) solar noon flights (LW12, WhS12, and WS12) along the principal solar plane, d) solar noon flights along the perpendicular solar plane, e) late afternoon flights (LW17 and WhS17) along the principal solar plane, and f) later afternoon flights along the perpendicular solar plane.

Table 3.5 Percent of total wall length obscured from sensor view by a tree canopy or large shrub. Values were calculated from digitized tree-canopy and building plan areas.

Wall blocked by tree:	Liberty Wells	White Sands	Western Springs
East (%)	14.95	22.25	12.51
West (%)	19.29	29.12	10.45
South (%)	14.90	21.59	14.12
North (%)	19.67	24.66	19.56

Figure 3.16 shows that the introduction of large tree canopies into an open low-rise/sparsely built neighbourhood creates cooler shaded temperatures. This increases the observed thermal anisotropy by making the cool region of the polar plot cooler. This is most obvious at solar noon when the sunlit surfaces are hottest, creating the largest temperature contrast. When calculating thermal anisotropy as the difference between $T_{B,max}$ and $T_{B,min}$, Liberty Wells and White Sands had very similar thermal anisotropy at solar noon, however, examining the difference between $T_{Off-Nadir}$ and T_{Nadir} indicates the differences between these sites. The White Sands site has a slightly smaller amplitude in the hot spot region and a much larger negative amplitude in the cool region of the plot. The Western Springs site has similar differences from nadir in the hot spot region, however it does not show this large negative deviation that the sites with large tree canopies do.

3.4.4 Assessment of Remotely Sensed Wall Temperatures

Anisotropy is the result of varying amounts of both horizontal and vertical facets with different surface temperatures forced by solar geometry and material property differences being observed by the instrument. Krayenhoff and Voogt (2016) found that the difference of opposing wall temperatures are an important factor of effective anisotropy. Figure 3.17 shows example images of typical houses found in each of the three sites.

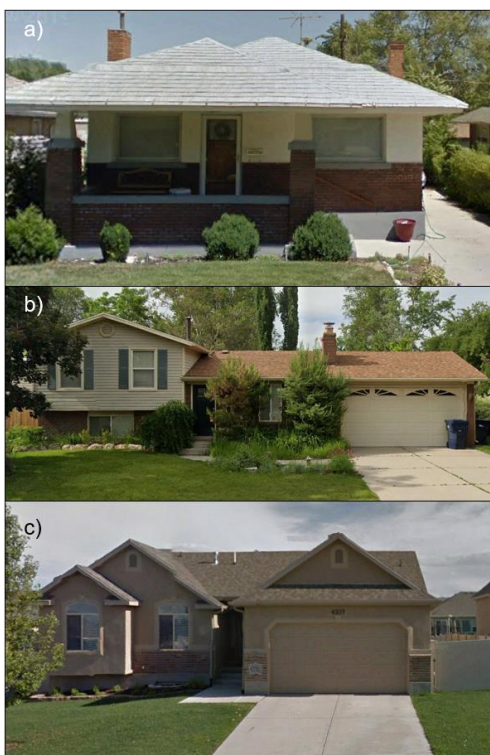


Figure 3.17 Sample houses from a) Liberty Wells, b) White Sands and c) Western Springs.

Liberty Wells and White Sands have similar vegetation cover and trees, or large shrubs, that tend to be planted up against building walls. This is expected to cause the walls to appear cooler both by shading and obstruction of the imager's view of the wall material as healthy transpiring tree-foliage is typically closer to air temperature than typical wall materials such as aluminum siding or brick. Walls are expected to be further cooled in the Liberty Wells site by the large porches found on the front of many of the houses. Hilland and Voogt, (2020) found that vertical facet self-shading by sub-facet scale structures like porches reduces the overall average facet temperature while both decreasing the surface temperature below the overhang as well as increasing the surface temperature above it. This could be important as at different ONAs, the thermal imager is observing a different fraction of vertical facet and could be observing mostly vertical facets above the porch at small ONAs and more shaded facet temperatures at lower larger ONAs. As the houses do not all face the same direction, this effect is expected to be equally observed for every

view direction. Houses in Western Springs, by contrast have relatively smooth walls with few sub-facet scale structures to provide shade and little vegetation to cool the apparent wall temperatures.

Wall temperatures were obtained by averaging wall temperatures extracted from thermal imagery taken from the truck traverses that coincided with each flight. Figure 3.18 shows the absolute difference in brightness temperature between opposing walls. The magnitude of temperature differentials ranges from 0.07°C to 8.56°C . The largest difference between north and south facing walls is for Western Springs, as there is less vegetation coverage blocking or shading the wall facets and decreasing the magnitude of the wall temperatures in general. The other sites show substantially smaller differences at solar noon when differences are expected to be maximized. The largest difference in north and south walls is observed for Western Springs and White Sands at solar noon. This caused south facing facets to be slightly hotter than north facing facets. The differences at solar noon ranged from 1.29°C for Liberty Wells to 6.03°C for Western Springs. The differences between north and south walls for the Liberty Wells and White Sands sites are quite small and is likely due to wall shading caused by both built features such as overhanging eaves and porches as well as large vegetation canopies shading the south walls. The mid-afternoon observations indicate that the surface temperature difference in north and south walls gets larger slightly after solar noon before again decreasing in the late afternoon. This is likely due to the tree-canopy coverage obscuring or shading the walls, leading to a slowed change in wall temperatures. This lag in temperature decrease after solar noon matches what Hilland (2018) found for buildings with large porches or overhangs.

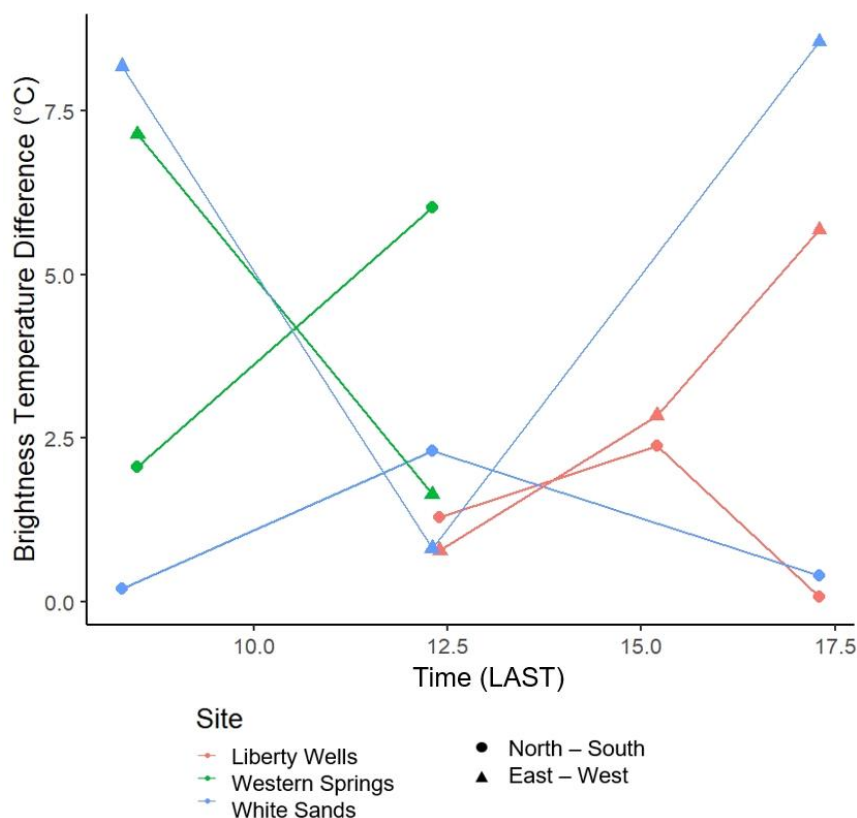


Figure 3.18 Opposing wall temperature differences. Temperature differences are expressed as absolute values. The data represented in this plot are a combination of three sampling times for different sites and wall orientations rather than a true time series.

Inversely, the largest east and west temperature differentials were observed during the morning and afternoon flights, with the lowest east-west temperature difference observed at solar noon for all sites. This is because at solar noon both the east and west facing facets are receiving similar amounts of solar radiation. The difference between east and west facing walls at solar noon is greatest for the Western Springs neighbourhood which was expected as it has less vegetation obstructing the walls. If there is no shading of east walls, they are expected to be relatively hot at solar noon as they have only just become shaded, whereas west-facing walls have been shaded and are much cooler. The largest temperature difference between east and west facing walls is observed for the White Sands flight and although there were no afternoon flights for Western Springs, the

morning trend suggests that White Sands would have a slightly larger temperature difference as it does for the morning flights. The wall temperature difference for east and west facing walls is very similar in both the morning and afternoon flights for White Sands. Houses in Liberty Wells having a lower temperature difference between east and west walls was expected due to the self-shading of the porches lowering the overall facet temperature of the sunlit walls.

The differences in opposing wall temperatures matches strongly with the observed thermal anisotropy for morning and afternoon flights. This is because at large solar zenith angles, vertical facets are receiving direct solar radiation causing the hot spot to be located at a larger ONA and more reliant of wall temperatures. This is apparent by looking at the afternoon flights. At solar noon, the hot spot is mostly formed by the difference in sunlit horizontal facets and shaded vertical facets. This is apparent as the thermal anisotropy is largest for LW12 and WhS12 however the opposing wall temperatures indicate the largest wall differentials were observed for WS12 between the north and south walls. Because the thermal anisotropy at solar noon is dependent on the difference between horizontal and vertical facets, the larger difference in opposing wall temperatures for WS12 caused the hot spot to be located at a larger ONA.

The effect of wall temperature differentials is most apparent when comparing opposite view directions on the polar plot such as what was done in Section 3.4.3. The cooler regions of the plots in Figure 3.16 show a relationship between vegetation cover and magnitude of anisotropy with the site with the least amount of tree-canopy cover having the most reduced negative amplitude. This all corresponds to the wall differential results which showed that the largest difference between opposing walls was found in the Western Springs site for all times and orientations except the morning observations of the White Sands site. Figure 3.16a and 3.16b also show a clear influence of wall temperature differentials as the magnitude of difference between east and west wall was similarly large for both WhS8 and WS8 which translates to very similar positive and negative amplitudes when looking at $T_{Off-Nadir} - T_{Nadir}$ along the principal solar plane. The difference between north and south wall temperatures was small during this flight and the

effect of this is evident in Figure 3.16b with the amplitudes being very small along the perpendicular solar plane.

3.5 Variability within Polar Plots

3.5.1 Flight Line Comparison and Spatial Variability

Past studies, such as Lagouarde et al. (2004), have used the standard deviation of the averaged mean zonal temperature values as an indicator of the spatial variability of a study site. The standard deviation of each point on the final polar plot is depicted in Figure 3.19. The average directional standard deviation was 1.89° for LW12, 1.65°C for WhS12, and 1.11°C for WS12. From these values it appears that the largest spatial variability is found in Liberty Wells, followed by White Sands and Western Springs. Western Springs is a smaller site than the other two with significantly lower vegetation cover. Table 3.4 shows the variability of landcover for each site when the site is subset into four smaller areas of a northwest, northeast, southwest and southeast quadrant. Liberty Wells has a clear east-west division of tree cover with a 2% difference between the two areas. Liberty Wells also has a difference in building cover of approximately 2-4% in the southern quadrants compared to the northern quadrants. In contrast, White Sands has a north-south difference in tree cover of approximately 5.5%. Western Springs has a more dispersed variability, with the southwest quadrant having much less tree cover than the other three quadrants as well as an increase in building cover for that quadrant.

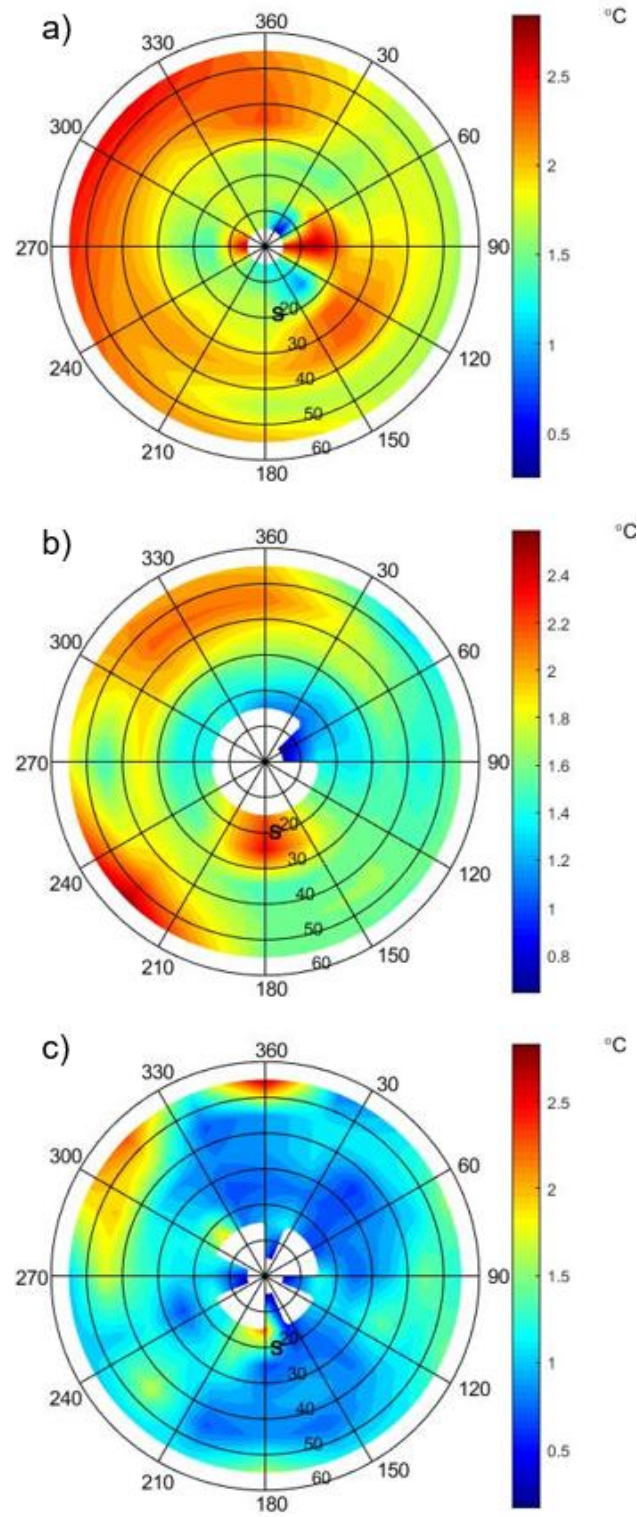


Figure 3.19 Polar plots of area averaged temperature standard deviation for (a) LW12, (b) WhS12, and (c) WS12.

Table 3.6 Spatial variability of λ_{tree} and λ_{p} for the three sites comparing the northeastern, northwestern, southeastern, and southwestern sections of the sites.

Landcover	Site	NE	NW	SE	SW	Average
λ_{tree}	Liberty Wells	0.2175	0.19398	0.21883	0.18916	0.2
	White Sands	0.17104	0.17353	0.22037	0.23298	0.19
	Western Springs	0.05998	0.078	0.04315	0.01919	0.05
λ_{p}	Liberty Wells	0.19271	0.20664	0.24683	0.22739	0.22
	White Sands	0.15895	0.16988	0.17082	0.16701	0.17
	Western Springs	0.22377	0.22347	0.22413	0.24165	0.22

Two flight lines were flown for each target angle and view azimuth within a 5-minute window across Liberty Wells and White Sands. This allowed for complete coverage of the full site and smoothed variability in the dataset due to variability in the site landcover. Comparing both flight lines for each solar noon flight, an assessment of the effect of spatial variability on area-averaged directional brightness temperature can be observed. Boxplots comparing the two flight lines for different ONA and view directions are shown in Figure 3.20.

The variability of surface cover is compared over the two flight lines for each view direction at 25° and 45° off-nadir. At a 25° off-nadir angle, the IQR of each flight line for Liberty Wells is similar in size. The largest differences in IQR are observed for the 45° ONA flight lines. The greatest difference in mean flight line temperatures at a 25° off-nadir angle is 3.21°C for a northeast view direction. The northeast and southeast view directions have differences in flight line mean temperatures >2°C and the south and west facing flight lines have a difference in mean temperatures <1°C. An effect of spatial variability on the different flight lines is the skewing of the data, which can be seen when observing Liberty Wells to the south or north where one flight line has a positive skew and the other a negative skew. With a 45° off-nadir angle, the range of temperatures for each view direction increases, sometimes only for one flight line. This is expected as a larger area is being observed. The interquartile range of each flight line overlaps for this view angle, with the exception of the west-facing view angles. The largest difference in

mean temperatures are northwest and southeast facing view directions with differences in mean temperatures $>2^{\circ}\text{C}$. North, northeast, south, and southeast facing flight lines all have a difference in mean temperatures between flight lines $<1^{\circ}\text{C}$.

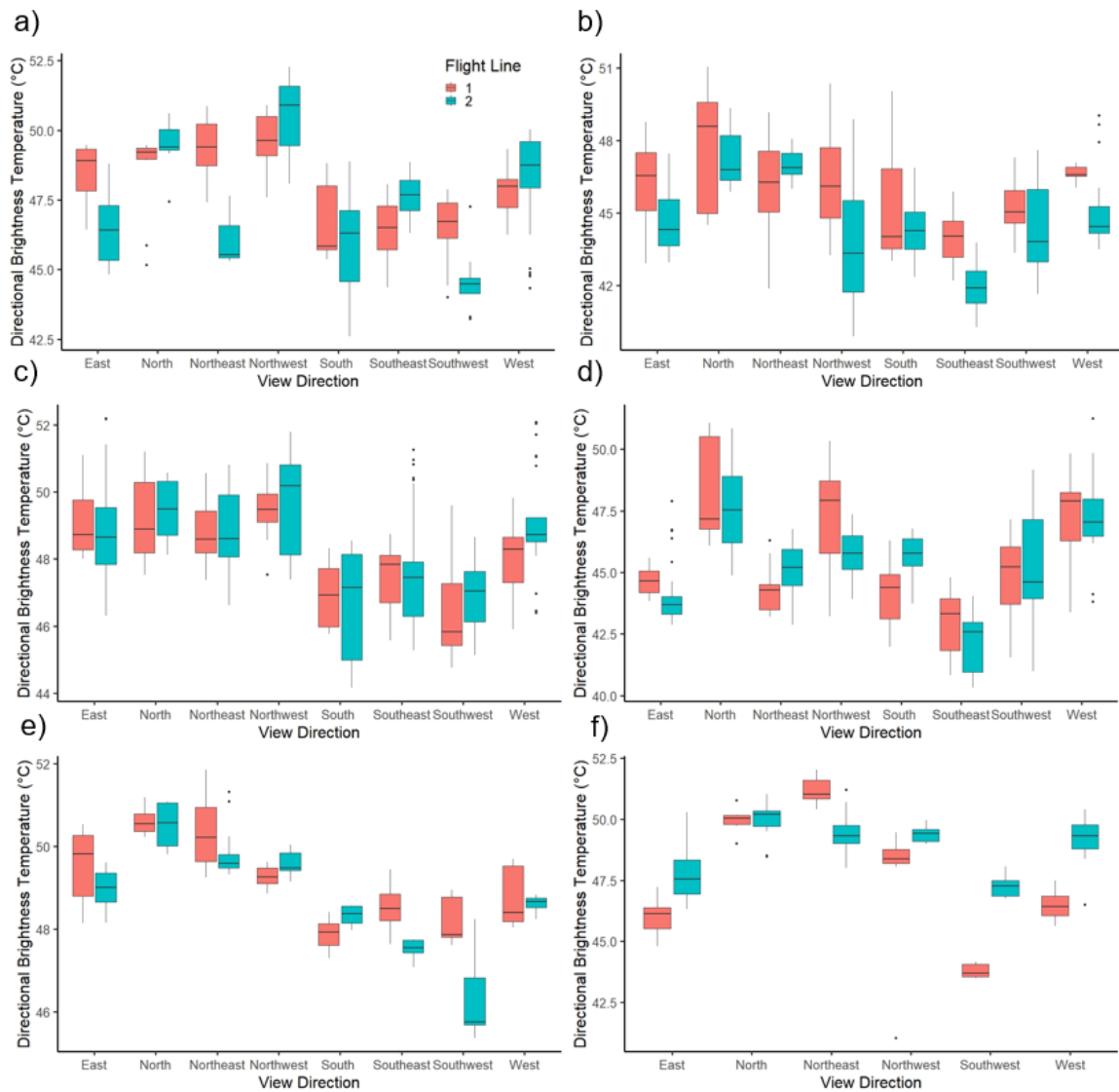


Figure 3.20 Comparison of DBT from select view azimuths and off-nadir angles for two flight lines separated by 5 minutes. (a) LW12 at a 25° ONA, (b) LW12 at a 45° ONA, (c) WhS12 at a 25° ONA, (d) WhS12 at a 45° ONA, (e) WS12 at a 25° ONA, and (f) WS12 at a 45° ONA. The boxes and whiskers are configured as in Figure 2.18.

White Sands, by contrast, has smaller differences in mean flight line temperatures despite the larger vegetation cover difference across the site compared to Liberty Wells. When viewing at a 25° off-nadir angle, only west facing flight lines have a difference in mean temperatures >1°C and at a 45° ONA only northwest and south facing flight lines show a difference in mean temperatures >1°C.

The interquartile range of the flight lines for 45° off-nadir view angles for Western Springs are smaller relative to the other two sites, suggesting vegetation at the other sites creates a larger IQR in area-averaged temperatures and contributes to the difference in range between flight lines. The largest difference in mean flight line temperatures is 3.43°C when observing in a southwest direction, however there is not enough data available for the south and southeast view directions to compare the difference in flight line temperatures. The only view direction with a difference in mean temperatures >1°C is when the observer is facing north. When viewing the site at a 25° off-nadir view angle, the magnitude of differences in mean temperatures over flight lines decreases. The southwest view direction is the only view direction to have a difference in mean flight line brightness temperatures >1°C.

This spatial variability has implications for the polar plots generated for each site. The DBT plotted on the polar plots are an average of each similarly oriented subset FOV_{subset} from each flight line. This means that variability observed when comparing flight lines is smoothed by averaging over both lines, however the skewing of the data caused by the variability of different flight lines could shift the average DBT causing some DBT to appear warmer or cooler than they would have if the site were homogeneous. This can lead to apparent outliers in the polar plot DBT. This is observed for a few flights such as WhS12 where there are large differences between $T_{B,5}$ and $T_{B,min}$.

Chapter 4

4 Discussion and Conclusion

4.1 Urban Anisotropy

Urban areas are known to generate thermal anisotropy, particularly more built up downtown neighbourhoods. However, limited data is available to characterize the thermal anisotropy of vegetated urban residential neighbourhoods which cover large extents of many cities. It is shown in this thesis that residential open low-rise / sparsely built neighbourhoods are capable of generating significant anisotropy and that this anisotropy varies with surface geometry. Both building plan area and vegetation cover create differences in anisotropy although only significant differences in tree-canopy coverage were investigated in this thesis. The site with less tree-canopy coverage reduced the overall anisotropy observed for both large and small solar zenith angles, although the anisotropy of all sites at large zenith angles became small and more similar. This occurs because at times of day with large solar zenith angles, such as early morning or late evening, the shadows cast by all trees and building vertical facets are large enough even for open residential areas to overlap and reduce the overall anisotropy. The overall structure of the polar plots were affected by the site geometry. Increasing vegetation cover created more shading of vertical facets which reduced the size of the hot spot away from nadir. No significant reduction in hot spot size was observed along the view azimuths near the hot spot center, likely because the three sites investigated had different surface geometries, although the Liberty Wells and White Sands neighbourhoods were quite similar. The results imply that the maximum effective anisotropy is very similar between Liberty Wells and White Sands, which was expected due to the similar site characteristics. However, when comparing the difference in 95th and 5th percentiles to eliminate the effect of outliers, the difference in anisotropy between the two sites becomes slightly larger. When comparing anisotropy in this way, Liberty Wells exhibits the largest anisotropy. The neighbourhoods sampled had similar building plan area fractions, however they had different configurations, with Liberty Wells having more

self-shading of vertical facets due to porches and a smaller inter-building spacing than White Sands. Hilland and Voogt (2020) found that the wall differential for buildings with ‘simpler’ facet geometry was larger than for buildings with more complex vertical facets. Results from this study suggest that when comparing sites with large tree-canopy coverage, this facet geometry causes slight differences but is not a strong control on the thermal anisotropy.

The study areas investigated in this thesis were chosen in part because of their relatively uniform neighbourhood characteristics. However, even these sites had spatial variability due to varying surface geometries. Both building and tree canopy coverage could vary from 5 – 6% across the sites. This variation in surface characteristics resulted in the largest standard deviations between thermal images of similar azimuthal and off-nadir view directions being observed for the site with large variability in building plan fraction. Tree canopies also contributed to the high spatial variability due to the large, randomly located cool regions created by these large tree canopies. Voogt (2008) found that increasing surface variability could increase the thermal anisotropy of different sites. This spatial variability has implications for scale in sampling sites with significant tree-canopy cover. Tree-canopy coverage is variable in any real world neighbourhood and these results indicate that for small sample areas or inadequate sampling over a larger area, the DBT can be highly variable and lead to potential outliers or warm/cool pockets appearing on the polar plot. Sampling over larger study areas smooths some of the variability and allows for comparison with coarser dataset such as data obtained from satellite imagery.

Previous studies from Iino and Hoyano, (1996), Nichol, (1998), Voogt and Oke. (1998), Lagouarde et al., (2004), and Lagouarde et al., (2010) have found Λ_{Max} to be on the order of 9 - 10°C over densely built urban areas. The results from this work found anisotropy to be ~6 – 8°C for the mix of open low rise and sparsely built neighbourhoods observed. This suggests that anisotropy for these neighbourhoods can be significant despite less built structure compared to more densely built downtown-type neighbourhoods, and that increasing the vegetation can, to a point, increase the anisotropy of the site. The overall distribution of DBT within the polar plots behaves as expected based on previous work (Lagouarde et al, 2004; Voogt and Oke, 2008).

Effective thermal anisotropy is dependent on the off-nadir angles being compared and in Voogt and Oke (1998), a maximum ONA of 45° was used. Sampling at larger ONA will always make the anisotropy appear larger because away from the hotspot the DBT drops off quickly at large angles. Using a maximum 45° ONA as a constraint, the largest effective anisotropies observed were 7.22°C , 6.41°C and 4.06°C for Liberty Wells, White Sands and Western Springs respectively. These correspond to a decrease of 4%, 16.3% and 23.1% relative to the maximum effective anisotropies reported for the maximum 55° ONA used in this study.

Voogt and Oke (1998) examined three sites, a residential site (Vancouver R), a light industrial site (Vancouver LI), and city center site (Vancouver CC). Figure 4.1 shows a comparison of maximum thermal anisotropy from different studies of mid-latitude sites near solar noon. Vancouver R shows a maximum thermal anisotropy near solar noon of approximately 6°C for their residential site, which is $\sim 1.22^\circ\text{C}$ smaller than that observed for Liberty Wells and $\sim 0.41^\circ\text{C}$ smaller than the White Sands site. Western Springs, with its low tree canopy coverage, has a thermal anisotropy $\sim 1.94^\circ\text{C}$ less than the residential site. The light industrial area had very similar λ_p and λ_{tree} values as the Vancouver city center, however its buildings were much shorter (smaller building height to width ratio), which changes the amount of shading present. Consequently, the Λ_{Max} observed for this site was approximately 6.7°C ; 1°C smaller than LW12, 0.03°C larger than WhS12, and 2.64°C larger than WS12. Compared to the Vancouver city center site at midday, the Salt Lake City residential study sites show less anisotropy - 20 – 30% less in the case of Liberty Wells and White Sands, and 40 % less in the case of Western Springs.

Using this same constraint, the thermal anisotropies observed for the Liberty Wells and White Sands are approximately 0.5°C and 1°C larger respectively than that for the Saint Barnabé site reported by Lagouarde et al. (2004). The Saint Barnabé site had a λ_p value of 0.25 (similar to Liberty Wells) and a λ_{tree} value of 0.30 which is much larger than either the Liberty Wells or White Sands sites and is comprised of a mix of low-rise and mid-rise dwellings. The maximum effective anisotropy of the Western Springs site (λ_{tree} of 0.05) is 1.62°C less than the Saint Barnabé site. Compared to the downtown Marseille site examined by Lagouarde et al. (2004), the thermal anisotropy for the Salt Lake City

residential sites studied here are lower by $\sim 0.8^{\circ}\text{C}$, $\sim 1.6^{\circ}\text{C}$, and 3.9°C for Liberty Wells, White Sands, and Western Springs respectively.

Lagouarde et al., (2010) looked at a city center site in Toulouse, France and observed a Δ_{Max} when constrained to 45° ONA of approximately 8°C at solar noon in July (Figure 4.1). This site has minimal tree-canopy coverage (between 0.05 – 0.08) and a high building plan area fraction (0.54). The results are very similar to the other city center sites which all show a large thermal anisotropy. It is important to note that these sites also have large building height to width ratios.

The thermal anisotropy of Western Springs compared to that of Liberty Wells and White Sands seems to affirm the hypothesis that increasing tree canopy cover in areas with low λ_p will increase the thermal anisotropy. Comparing these results to the thermal anisotropy of a site with very high vegetation cover suggests that increasing the tree canopy coverage past a threshold will lower the thermal anisotropy as the whole site becomes cooler due to an increase in overlapping shade. This corroborates the hypothesis suggested in Section 1.3.

Figure 4.1 shows a comparison of airborne observational studies of thermal anisotropy for urban settings. Table 4.1 outlines the sample dates and conditions of these observations. Figure 4.1 shows that for a site with both very low building cover and very low tree-canopy cover, the thermal anisotropy is relatively low (e.g. WS12). As building cover increases, the thermal anisotropy also increases. It is important to note however, that the height to width ratio of the buildings increases (as well as a decrease in tree height to building height ratio) for the city center sites which also contributes to the increase in thermal anisotropy. The increase in height to width ratio means there is a lot more influence from vertical surfaces compared to the residential sites, which all have low- to mid-rise buildings. These large vertical surfaces create more temperature contrast similar to the tree canopies by creating large hot surfaces as well as large, cool shaded regions. This explains the difference in thermal anisotropy between the Vancouver CC and Vancouver LI sites. Both have very similar λ_p and λ_{tree} values, however the height to

width ratio is much larger for Vancouver CC, creating larger temperature contrasts and consequently a larger Λ_{Max} .

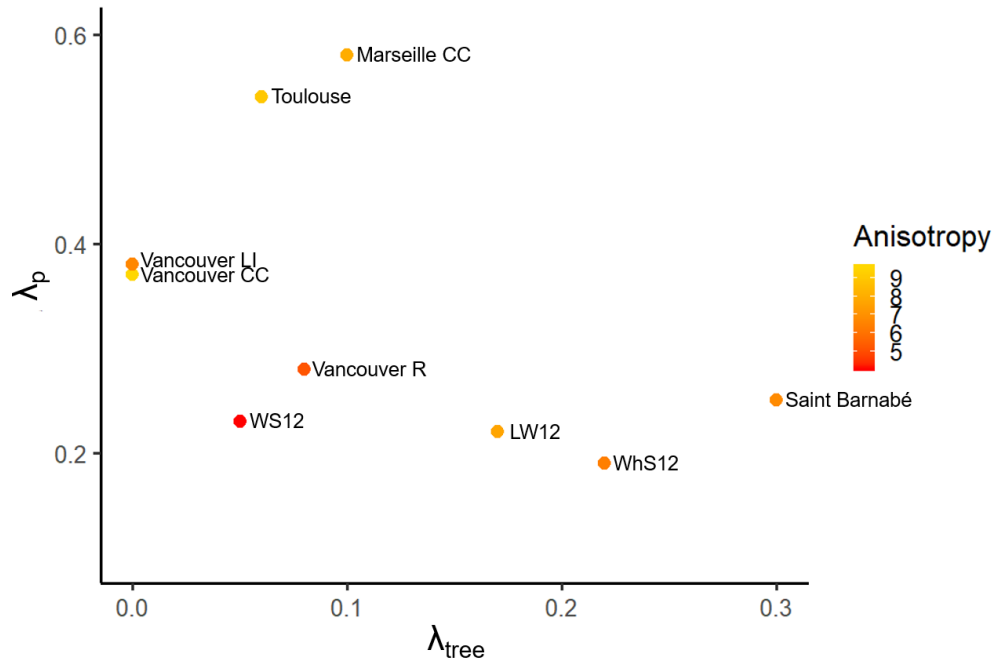


Figure 4.1 Comparison of Λ_{Max} (constrained to a max ONA of 45°) by tree-canopy plan fraction (λ_{tree}) and building plan fraction (λ_{p}) for 9 mid-latitude neighbourhoods at mid-day: Marseille city center (CC) and Saint Barnabé in France (Lagouarde et al., 2004), Toulouse city center in France (Lagouarde et al., 2010), Vancouver city center (CC), Vancouver light industrial (LI), and Vancouver Residential (R) in Canada (Voogt and Oke, 1998) as well as LW12, WhS12, and WS12. Circle colour indicates the magnitude of thermal anisotropy as indicated by the colour bar.

Increasing the tree-canopy cover increases the anisotropy when comparing the LW12, WhS12, WS12, and Vancouver R sites supporting the hypothesis that increasing vegetation will increase the temperature contrast and hence anisotropy across the site for open low-rise / sparsely built sites. Thermal anisotropy for the Saint Barnabé site was similar to that for the LW12 and WhS12 sites, although there were slight differences in building height, with the Saint Barnabé site having some buildings 1 – 2 storeys taller than the Liberty Wells and White Sands sites. Increasing the building height to width

ratio can increase the Λ_{Max} , as observed between Vancouver CC and Vancouver LI, which implies the sensitivity of thermal anisotropy to changes in λ_{tree} is reduced for $\lambda_{\text{tree}} > 0.2$ or could even be reducing the Λ_{Max} . This comparison of study results suggests that a characteristic maximum summer (leaf-on), clear sky, mid-latitude thermal anisotropy for low density residential sites with considerable tree-canopy coverage is approximately 7°C even as the tree-canopy coverage increases to close to 30%.

Table 4.1 Summary table of site conditions for the sites discussed in Figure 4.1 (Voogt and Oke, 1998; Lagouarde et al., 2004; Lagouarde et al., 2010)

Site	Date	Time (LAST)	Latitude (°)	Solar Zenith Angle (°)	T_{air} (°C)	RH(%)	Wind Speed (m/s)
LW12	12 Jul	12:00	40.76	18.94	34.5	40.5	2.1
WhS12	15 Jul	12:00	40.76	19.37	32.4	38.9	1.8
WS12	19 Jul	12:00	40.76	20.06	34.2	16.0	0.0
St. Barnabé	12 Jul	11:58	43.30	21.30	24.5	31.0	6.0
Vancouver R	17 Aug	12:15	49.27	36.60	21.0	-	5.1
Vancouver LI	15 Aug	12:15	49.27	35.96	21.0	-	4.1
Vancouver CC	16 Aug	11:45	49.27	39.09	18.6	-	8.2
Marseille	26 Jun	12:35	43.29	21.20	29.4	43.9	4.3
Toulouse	15 Jul	11:45	43.60	24.0	24.3	-	3.0

Generalizing from the results presented in this thesis, the anisotropy found in this study and for residential neighbourhoods in Vancouver and Marseille are very similar, suggesting that anisotropy between 4 - 8°C can be expected for residential neighbourhoods in mid-latitude cities for summer clear sky leaf-on conditions. For similar conditions but sites with considerable tree canopy cover (at least >10%), this expected maximum anisotropy becomes 7 – 8°C. This is important because approximately 50% of the population in Canadian cities lives in a low-density

neighbourhood (at least 66% of these low-density houses are single-family dwellings) (Turcotte, 2008). This means that low density residential neighbourhoods cover a large fraction of urban land area, particularly compared to areas like city centers which, although they create large thermal anisotropy, are relatively small compared to the entire urban area. From a satellite perspective, these low-density residential areas will take up more pixels over a city area so understanding the anisotropy of these areas is important.

4.2 Land Surface Temperature

Land surface temperature is a critical variable needed to perform calculations for surface energy balances and hydrological cycles (Li et al., 2013). Thermal anisotropy has been found to impact measurements associated with land surface temperature such as thermal inertia, which describes the variation of land surface temperature (Zhan et al., 2012), thermal infrared emissivity, which impacts the earth's surface radiation and energy budget (García-Santos et al., 2015), and the urban heat island (Li and Li, In Press) among others. With the increased availability of affordable, high spatial or temporal resolution satellite data, satellites are often used to generate land surface temperatures.

The ATSR series of sensors are the only satellite-borne series of sensors capable of viewing multiple view directions of the same surface in short succession. Coll et al., (2019) determined, using the Advanced Along Track Scanning Radiometer (AATSR) on board the European Space Agency Envisat satellite, that the thermal anisotropy calculated between the nadir view angle and forward-looking view angle ($\sim 55^\circ$) was as large as 8°C over heterogeneous, non-isothermal surfaces. Polar orbiting and geostationary satellites only provide one view direction of a target location at a time, although polar orbiting satellites can provide multiple view directions when a site is observed over different observation days. Polar orbiting satellites, such as MODIS, are popular satellite platforms for thermal analysis because they provide 1 km resolution at nadir compared to 3 km for geostationary satellites such as SEVIRI, however, a limitation of polar orbiting satellites is the range of potential ONA for an image. MODIS, for example, has a swath of $\pm 55^\circ$ with potential ONA up to 65° for some pixels. Hu et al., (2016) found the urban thermal

anisotropy of a downtown core derived from MODIS satellite imagery to be on the order of $\sim 9^{\circ}\text{C}$ when averaging over the summer months for 10 years. The thermal anisotropy observed by satellite platforms corresponds to thermal anisotropy observed using airborne methods for densely built sites which indicates that the resolution of satellite imagery allows for the effects of thermal anisotropy to be observed.

Using the MODIS instruments as an example, the possible view angles and times of AQUA and TERRA satellites for the Salt Lake City valley were plotted. The polar plot shown in Figure 4.2 show a compilation of approximate view angles and times that AQUA and TERRA would have viewed Salt Lake City, UT between July 8 – 21, 2018. The satellites observed the city at approximately the solar noon flight times. Assessing the polar plots for only four view azimuths (northwest, west, northeast, east) that correspond to the MODIS viewing azimuths, the Δ_{Max} of each study site is 6.27°C (16.1% decrease) for LW12, 6.95°C (9.3% change) for WhS12, 3.09°C (41.6% decrease) for WS12. This demonstrates that for common view angles and observation times for a MODIS user, there is a potentially large thermal anisotropic effect that can be observed for these sites depending on the day of observation. This indicates that open low rise or sparsely built neighbourhoods, particularly with significant tree-canopy coverage, can produce large thermal anisotropy that can be observed with satellite imagery and must be considered. This analysis assumes that both the satellite nadir and off-nadir view is observing a consistent LCZ. However, the large ONA IFOV of MODIS imagery introduces the possibility of observing a much larger area at large ONA compared to nadir. This anisotropic effect would be exacerbated, or possibly reduced, by spatial anomalies, such as large parks, bodies of water, or neighbouring LCZ covering a portion of the pixel.

Similar comparisons can be made for Landsat satellites, which follow a similar flight path and overpass time as the MODIS satellites. Landsat 7 has a thermal infrared (TIR) radiometer with a resolution of 60 m and Landsat 8 has a TIR radiometer with a resolution of 100 m, which is a considerably higher resolution than MODIS but samples at a restricted ONA range of $\pm 7.5^{\circ}$. Comparing near nadir measurements from LW12, WhS12, and WS12, the difference along a Landsat transect is 3.4°C for LW12, 2.0°C for

WhS12, and 1.9°C for WS12. The range of ONA a Landsat TIR sensor can observe is considerably smaller than a MODIS thermal sensor so the uncertainty between Landsat measurements due to thermal anisotropy is relatively small. The anisotropic effect on these measurements is still relevant when comparing Landsat land surface temperature observations to land surface temperatures obtained by other sensor platforms. The smaller anisotropy observed by a Landsat satellite does not imply the results are a better measure of urban LAST due to the extremely limited representation of vertical surface temperatures captured by these sensors. Vertical surface temperatures not only contribute to the overall temperature of the urban surface, they are arguably more important for some uses, like pedestrian comfort, than roof temperatures, which are primarily sampled near nadir and which provide only limited direct thermal emission (for a pitched roof) into a street canyon.

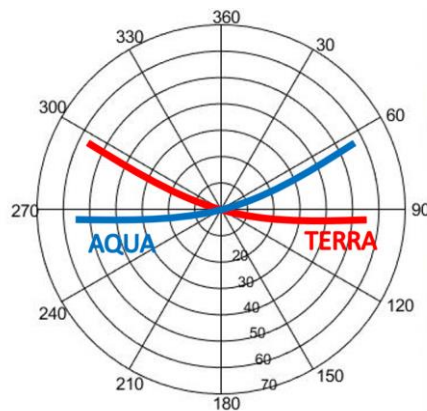


Figure 4.2 Polar plot showing the MODIS viewing angle distributions for Salt Lake City between 8 July and 21 July 2018.

4.3 Critique and Evaluation of the Sampling Method

Airborne sampling of anisotropy is an effective method for sampling many view directions over a relatively short period of time in a relatively homogeneous study area compared to the use of satellite imagery. The time required to undertake the airborne

sampling, however, is long enough that surface temperatures are likely to have changed appreciably over the sampling period. This creates a limitation in creating a polar plot that is representative of a single point in time (specific solar zenith and azimuth angles). Lagouarde et al., (2004) addressed this problem by limiting sampling durations to under 20 minutes, which limits the number of flight lines that can be flown.

Results from this thesis suggest that, for some urban geometries, morning flights undergo such rapid increase in surface temperatures that corrections are still needed for traverses under 20 minutes. Performing temporal corrections on DBT is a way to simulate polar plots that are representative of a single point in time, however this solution also poses problems. Temporal corrections are dependent on both ONA and view azimuth, so creating valid corrections requires a knowledge of the change in DBT from multiple, if not all, view directions and ONAs. Limiting these comparisons creates the risk of a poor correction but increasing these data necessitates a longer period of airborne sampling or the use of multiple instruments or viewing platforms that must then be intercompared.

Alternatively, numerical models (e.g. surface energy balance models such as TUF3d) that can represent temperatures of the three-dimensional urban surface structure and combined with a sensor view model can be used to create temporal corrections of DBT for all data points. However, the calculated correction is subject to the accuracy of the models in predicting the changes in DBT for a particular site that arise from limitations in the model's ability to represent the surface temperature. Parameterizations of the convective heat transfer process as well as the limitations of a model to accurately represent a site's detailed surface characteristics all affect accuracy. Real world sites are not uniform, as many models used for urban energy balance and sensor view DBT assume, which introduces a further problem. The addition of tree-canopy vegetation that is not uniformly sized, shaped, or distributed is an additional complexity in modelling a real site. The model used in this thesis was run with crude approximations of the site geometries and comparisons were done to repeated flight legs to compare the performance of the correction polynomials.

A third approach to the problem of temporal changes is to change the sampling methodology to reduce the number of sampled view directions. A greater number of sampled view directions provides potentially more detail to the polar plot of directional brightness temperatures but comes at the expense of a longer acquisition time, which increases the likelihood of the need for temporal corrections. In this section, tests are conducted to determine the impacts of using different azimuth and off-nadir angle sampling configurations to determine whether using a reduced number of sampling points could successfully replicate the observed polar plots. These results provide important guidance for the design of future observational campaigns to minimize the data acquisition time while ensuring sufficient view angles are sampled to retrieve the important components of the directional temperature distribution.

Observations from WhS8, WhS12, and WhS17 were used to generate polar plots with different combinations of off-nadir angles and view azimuths. Test 1 used all azimuth angles sampled in this thesis but limited the ONA to nadir, 25°, and 45° off-nadir. Test 2 used all azimuth angles and limited the ONA angles to just nadir and 45°. Tests 3 – 5 used only 4 azimuth angles, north, south, east, and west, which are close to the principal and perpendicular solar axis sampled by this thesis for these three flights. Test 3 uses all ONA angles sampled for this thesis whereas test 4 uses nadir, 25°, and 45° ONA angles and test 5 only uses nadir and 45°. Figure 4.3 demonstrates the different tests performed and the results of creating a contoured polar plot with different data point positions for WhS17. Contour plots are constrained by the point density used to generate the plot, and as such, there are limitations to extrapolating information from these plots. The results of the other two flights can be found in Appendix C. The polar plots are generated by using a marching squares algorithm to determine the relationship between every cell in an input matrix and then linearly interpolating along the borders of each cell to determine the location of a contour line.

The polar plot representation of each site is skewed depending on the location of datapoints used to create these input matrices. Figure 4.3 shows this effect, as Figures 4.3a, b, d, and e all use more than one ONA per view azimuth and consequently represent the hot spot as a smaller area than polar plots created with only one large ONA observed.

This is relevant as past studies, such as Voogt and Oke (1998), only used nadir and 45° off-nadir for observation angles which would have left a lot of ambiguity in assessing the full extent of the hot spot and the overall pattern of a polar plot. Interpreting a polar plot with few data points plotted increases the uncertainty of the DBT away from the observational results.

Table 4.2 summarizes the results of the tests by comparing the resultant matrices. The $T_{B,max}$, $T_{B,min}$, Λ_{Max} , $T_{B,95}$, $T_{B,5}$, and Λ_{95-5} are shown for the full dataset of each flight and the limited matrices created using the constraints of each test. Comparing $T_{B,Max}$, and $T_{B,Min}$, using all ONA angles and limiting the view azimuths appears to be the best approach. This means sampling in the principal and perpendicular solar planes at as many ONA angles as possible. Comparing $T_{B,95}$ and $T_{B,5}$, which gives a more unbiased assessment of anisotropy, gives similar results. Sampling as many ONA angles as possible within a short time period allows the maximum magnitude of the hot spot to be completely observed as long as the view azimuths are in-line or perpendicular to the solar angle. This method, however, does not account for potential lag generated by different material properties within the sites heating at different rates and lagging the solar position change. This potential lag means that the location of the hot spot could be offset slightly from the solar azimuth. Focusing the sampling density to the area opposite the solar position would allow for the best characterization of the hot spot and any potential lag in the hot spot position if that is the objective of the observations.

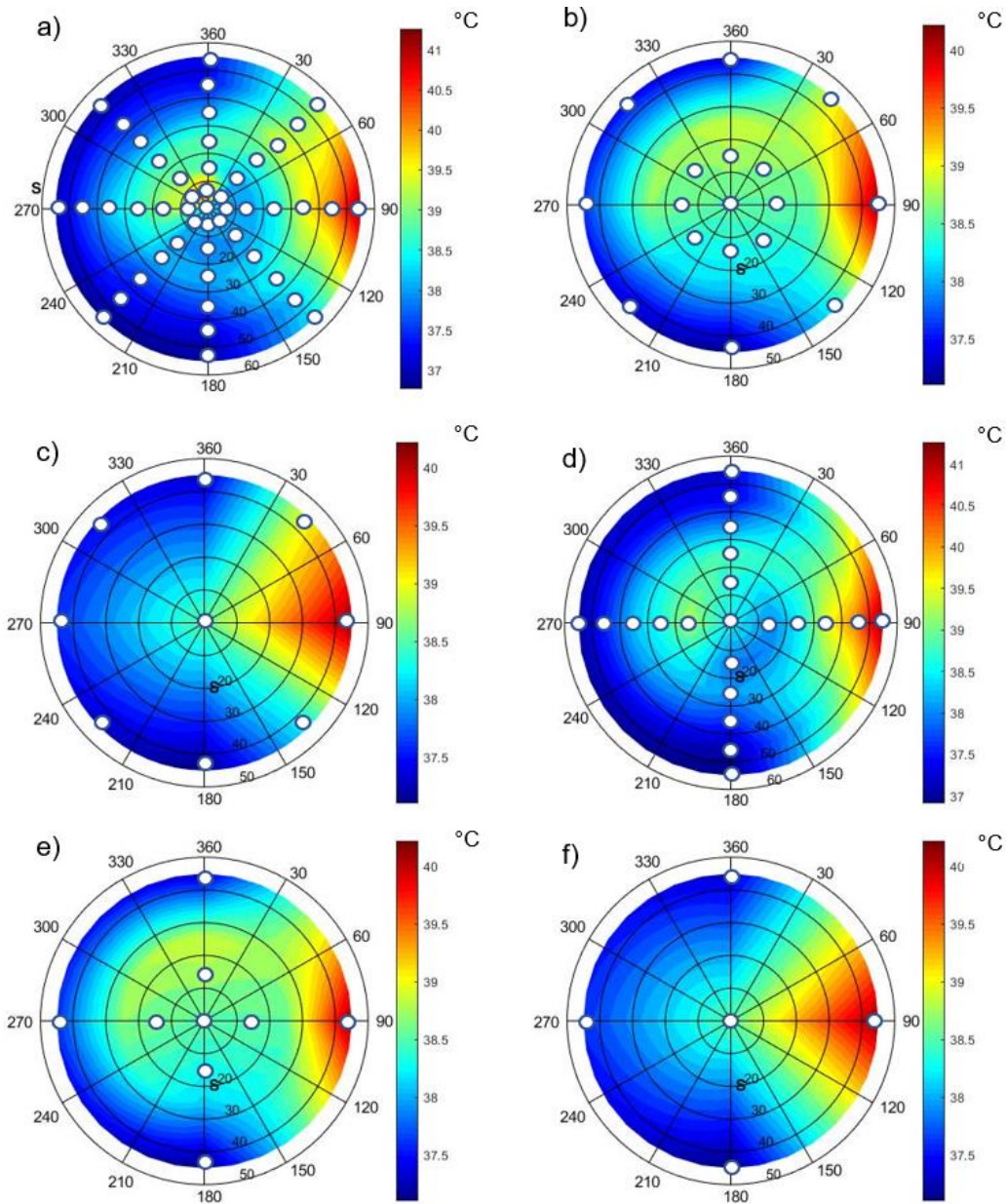


Figure 4.3 Polar plots using limited number of data points. The white dots indicate the data points used to create each plot. (a) Complete dataset, (b) test 1, (c) test 2, (d) test 3, (e) test 4, and (f) test 5.

Table 4.2 Results of differing azimuth and zenith configurations on effective anisotropy for the morning (WS8), solar noon (WS12), and late afternoon (WS17) flights. Bolded rows indicate the results from the complete combination of azimuth and zenith angles and ΔT indicates the difference of the test from these original datasets.

Test	$T_{B,max}$ (°C)	$T_{B,min}$ (°C)	Λ_{max} (°C)	$T_{B,95}$ (°C)	$T_{B,5}$ (°C)	Λ_{95-5} (°C)
WhS8	33.46	27.53	5.93	32.51	27.74	4.76
1	32.93	27.91	5.02	31.71	27.99	3.72
ΔT	0.53	-0.37	0.90	0.80	-0.24	1.04
2	32.93	27.91	5.02	32.29	27.94	4.35
ΔT	0.53	-0.37	0.90	0.21	-0.20	0.41
3	33.46	27.77	5.69	32.85	28.16	4.69
ΔT	0.00	-0.24	0.24	-0.34	-0.41	0.07
4	32.93	28.20	4.73	32.27	28.21	4.07
ΔT	0.53	-0.66	1.19	0.23	-0.46	0.70
5	32.93	28.20	4.73	31.92	28.38	3.55
ΔT	0.53	-0.66	1.19	0.58	-0.63	1.22
WhS12	48.81	41.15	7.66	48.37	42.26	6.11
1	48.15	42.40	5.76	47.75	42.85	4.90
ΔT	0.66	-1.25	1.91	0.62	-0.59	1.21
2	47.79	42.40	5.39	47.14	42.61	4.54
ΔT	1.02	-1.25	2.27	1.23	-0.35	1.58
3	48.59	41.86	6.74	48.14	42.73	5.40
ΔT	0.22	-0.71	0.93	0.24	-0.47	0.71
4	47.84	43.10	4.75	47.79	43.40	4.39
ΔT	0.97	-1.95	2.92	0.58	-1.14	1.72
5	47.79	43.10	4.69	47.79	43.40	4.39
ΔT	1.02	-1.95	2.97	0.58	-1.14	1.72
WhS17	40.81	36.50	4.31	39.44	36.71	2.73
1	39.81	36.92	2.89	38.94	36.98	1.96
ΔT	1.00	-0.42	1.42	0.50	-0.27	0.77
2	39.81	36.92	2.89	39.40	36.95	2.45
ΔT	1.00	-0.42	1.42	0.05	-0.24	0.28
3	40.81	36.63	4.18	39.72	36.84	2.88
ΔT	0.00	-0.13	0.13	-0.28	-0.13	-0.15
4	39.81	36.92	2.89	39.41	36.97	2.43
ΔT	1.00	-0.42	1.42	0.03	-0.26	0.30
5	39.81	36.92	2.89	39.45	36.94	2.51
ΔT	1.00	-0.42	1.42	-0.01	-0.23	0.22

4.4 Summary and Conclusions

This thesis presents airborne observations of effective thermal anisotropy for three different open low rise/sparsely built, vegetated urban sites. The observation method attempted to maximize the number of azimuth and zenith sensor view directions sampled to create the highest possible resolution of the directional variability while minimizing temporal effects on the observed directional brightness temperatures. Three residential, suburban-type neighbourhoods within Salt Lake City, Utah were observed for three different solar angles to compare the thermal anisotropy created with different tree canopy cover and solar angle. The results suggest that:

1. temporal variability of directional brightness temperatures measured within the 30-minute flight times is significant requiring corrections of up to 4°C;
2. future sampling should be restricted to less than 20 minutes and might use a restricted range of viewing angles of only the parallel and perpendicular solar planes to minimize sampling time or else temporal corrections should be applied;
3. early morning observations are subject to the largest changes in surface temperature and therefore affects the temporal variability of DBT;
4. increasing the amount of tree-canopy coverage increases the spatial variability of DBT across flight lines;
5. increasing vegetation cover in open low rise/sparsely built neighbourhoods can increase the effective anisotropy by up to 3°C due to the increase in temperature contrast observed by the sensor in agreement with previous model results (Dyce & Voogt 2018);
6. open low-rise/sparsely built sites with low tree-canopy cover fractional area do not exhibit large changes in effective anisotropy at different solar zenith angles;
7. the extent of wall self-shading and vegetation location with respect to the built structure needs to be considered along with λ_p and λ_{tree} when assessing effective anisotropy;

8. the effective thermal anisotropy of open low-rise/sparse built sites with some degree of tree canopy coverage is significant, with greater thermal anisotropy observed for the sites with more tree canopy coverage ($\sim 8^{\circ}\text{C}$) compared to similar sites with low vegetation cover ($\sim 6^{\circ}\text{C}$).

Potential of random uncertainty in the thermal anisotropy exists due to the need for corrections due to atmospheric and temporal interference on the order of the thermal anisotropy although steps were taken to verify the validity of the corrections used. Observations of different sites were obtained on different days, causing a potential difference in the maximum range observed for each site, although conditions between study days were very similar. Systematic uncertainty is believed to be small due to calibration tests performed (see Appendix A) on all instruments used in this project.

The results of this thesis emphasize the importance in considering thermal effective anisotropy for all urban surface cover. The implications for satellite assessments of land surface temperature were discussed, as well as possibilities for refining the airborne observation technique used in this work. These data will be useful for refining techniques of anisotropy assessment for satellite thermal observations as well as for evaluating models of urban thermal anisotropy. The results of this thesis suggest that the thermal anisotropy of typical North American suburban type neighbourhoods is significant and needs to be considered when discussing the remotely sensed surface temperature of these sites. The effective thermal anisotropy is largest at solar noon for typical North American suburb-type neighbourhoods, with the anisotropy similar at solar angles close to peak solar zenith angle but falling off steeply for large solar zenith angles.

4.5 Future Work

This thesis has identified many different paths for future work to take. First, the observational data collected in this project provides a detailed and valuable dataset that would enable the evaluation of both urban canopy-scale models, including those that incorporate integrated canyon scale vegetation (Krayenhoff et al., 2020), as well as

models of urban thermal anisotropy, such as the sensor view model SUMVeg. In the former case, the detailed facet-scale temperatures from the airborne thermal imagery that represent at the neighbourhood scale roofs, walls, roads and vegetation, as well as their combined influence (e.g. ground-level temperature) can be used to test the performance of modelled component temperatures, assuming work to characterize the surface emissivity is undertaken. In the latter case, the airborne DBT provide the potential to evaluate models of urban thermal anisotropy, especially those that incorporate vegetation, to test their ability to predict the effect of vegetation on thermal anisotropy for similar neighbourhoods.

This work examined sites with tree-canopy shading as well as a combination of tree-canopy and complex building form and determined differently structured polar plots for similar, and large, thermal anisotropy between these different scenarios. The effects of self-shading were also investigated by Hilland and Voogt (2020) who determined that it had a large effect on wall temperatures. Observational data are limited by the constraints of real neighbourhoods, so sensor view models could be used to determine the individual effects of complex wall structure like porches or overhangs versus vegetation shading in more detail than was explored here.

It was discovered in this work that temporal variability of DBT can be large, particularly during morning traverses where DBT changes rapidly enough to require a temporal correction for a 20-minute traverse. It was also clear by examining the difference between morning and afternoon traverses with similar solar elevation that the DBT changes at different rates in the morning and afternoon. The temporal variability of DBT was only examined for the three sites and three flight times observed for each site. It is currently unknown what the minimum sampling time would be for other site geometries or solar elevations. Model assessment of temporal variability over different flight times could be performed to determine the minimum sampling time for airborne thermal anisotropy for different solar elevations and site geometries. This would identify the best sampling method to observe the thermal anisotropy of a particular site while eliminating the need to correct for temporal variability in DBT.

A comparison of these data to satellite data could be undertaken to improve the capability of satellite data to predict effective anisotropy. As Hu et al., (2016) point out, vegetation is difficult to distinguish from the built structure at the satellite scale. These data provide a useful baseline anisotropy estimate for relatively homogeneous neighbourhoods for comparison to satellite estimates.

Assessing the relationship between nadir and off-nadir temperatures further could help develop methods of correcting for the anisotropic effect of these sites on land surface temperature.

This thesis examined the thermal anisotropy of a limited number of study sites for which the variation in vegetation and built cover characteristics is constrained. Future work is recommended to test the differences in building cover (λ_p) with constant tree-canopy cover to determine the effect that building properties have on the thermal anisotropy of sites with significant tree-canopy coverage. Similar observations are recommended to test the effect of building height to width ratio in neighbourhoods with significant tree-canopy coverage such as open mid-rise and open high-rise neighbourhoods.

Observations using a different sampling methodology to minimize the temporal effects on the dataset would be of benefit as well. Both correcting and not correcting temporal data can create different uncertainties within the dataset. Developing a method that minimizes or eliminates the need for these corrections, while also acknowledging the necessity for this approach in some cases, would create a better comparison between sites.

References

- A. Berk, P. Conforti, R. Kennett, T. Perkins, F. Hawes, and J. van den Bosch, "MODTRAN6: a major upgrade of the MODTRAN radiative transfer code," Proc. SPIE 9088, Algorithms and Technologies for Multispectral, Hyperspectral, and Ultraspectral Imagery XX, 90880H (June 13, 2014); doi:10.1117/12.2050433.
- Adderley, C., Christen, A., & Voogt, J. A. (2015). The effect of radiometer placement and view on inferred directional and hemispheric radiometric temperatures of an urban canopy. *Atmospheric Measurement Techniques*, 8, 2699-2714.
- Apogee Instruments. (2020a). *Infrared Radiometers*. Retrieved from Apogee Instruments Specification Sheets: <https://www.apogeeinstruments.com/content/SI-100-400-spec-sheet.pdf>
- Apogee Instruments. (2020b). *Apogee Pyranometers*. Retrieved from Apogee Instruments: <https://www.apogeeinstruments.com/content/SP-510-610-spec-sheet.pdf>
- Berk, A., Bernstein, L. S., & Robertson, D. C. (1987). *MODTRAN: A Moderate Resolution Model for LOWTRAN7*. Technical Report GL-TR-89-0122, United States Air Force.
- Byrnes, A. E., & Schott, J. R. (1986). Correction of thermal imagery for atmospheric effects using aircraft measurement and atmospheric modeling techniques. *Applied Optics*, 25(15), 2563-2570.
- Campbell Scientific. (2020). *HC2-S3-L*. Retrieved from Campbell Scientific: <https://www.campbellsci.ca/hc2-s3>
- Coll, C., Galve, J., Niclos, R., Valor, E., & Barbera, J. (2019). Angular variations of brightness surface temperatures derived from dual-view measurements of the Advanced Along Track Scanning Radiometer using a new single band atmospheric correction method. *Remote Sensing of Environment*, 223, 274-290.
- Dyce, D., & Voogt, J. A. (2018). The influence of tree crowns on urban thermal effective anisotropy. *Urban Climate*, 91 - 113.
- FLIR. (2016). *User's manual FLIR T6xx series*. Retrieved from FLIR Systems: <https://www.flir.com/globalassets/imported-assets/documents/flir-t6xx-series-user-manual.pdf>
- Garcia-Santos, V., Coll, C., Valor, E., Niclos, R., & Caselles, V. (2015). Analyzing the anisotropy of thermal infrared emissivity over arid regions using a new MODIS land surface temperature and emissivity product (MOD21). *Remote Sensing of Environment*, 169, 212-221.
- Guillevic, P. C., Bork-Unkelback, A., Gottsche, F. M., Hulley, G., Gastellu-Etchegorry, J.-P. O., & Privette, J. L. (2013). Directional view effects on satellite land surface temperature products over sparse vegetation canopies - A multisensor analysis. *IEEE Geoscience and Remote Sensing Letters*, 10(6), 1464 - 1468.

- Heitronics. (2004). *Infrared Radiation Pyranometer KT15IIP*. Retrieved from Heitronics Infrarot Messtechnik GmbH:
https://heitronics.com/fileadmin/content/Prospekte/KT15IIP_e_V510.pdf
- Hilland, R. V. (2018). The effect of sub-facet scale geometry on vertical facet temperatures in urban street canyons. *Electronic Thesis and Dissertation Repository*, p. 5761. Retrieved from <https://ir.lib.uwo.ca/etd/5761>
- Hilland, R. V., & Voogt, J. A. (2020). The effect of sub-facet scale surface structure on wall brightness temperatures at multiple scales. *Theoretical and Applied Climatology*. doi:<https://doi.org/10.1007/s00704-020-03094-7>
- Hu, L., Monaghan, A., Voogt, J., & Barlage, M. (2016). A first satellite-based observational assessment of urban thermal anisotropy. *Remote Sensing of Environment*, *181*, 111-121.
- Iino, A., & Hoyano, A. (1996). Development of a method to predict the heat island potential using remote sensing and GIS data. *Energy and Buildings*, *23*, 199 - 205.
- Kadygrov, R. N., Ganshin, E. V., Miller, E. A., & Tochilkina, T. A. (2015). Ground-based Microwave Temperature Profilers: Potential and Experimental Data. *Atmospheric and Oceanic Optics*, *28*(6), 598 - 605.
- Kantor, A. J., & Cole, A. E. (1962). Mid-latitude atmospheres, winter and summer. *Geofisica Pura e Applicata*, *53*(1), 171-188.
- Kimes, D. S. (1980). View angle effect in the radiometric measurement of plant canopy temperature. *Remote Sensing of Environment*, *10*, 273 - 284.
- Kimes, D. S., Newcomb, W. W., Nelson, R. F., & Schutt, J. B. (1986). Directional reflectance distributions of a hardwood and pine forest canopy. *Transactions on Geoscience and Remote Sensing*, *24*(2), 281 - 293.
- Krayenhoff, E. S., & Voogt, J. A. (2007). A microscale three-dimensional urban energy balance model for studying surface temperatures. *Boundary-Layer Meteorology*, *123*(3), 433-461.
- Krayenhoff, E. S., & Voogt, J. A. (2016). Daytime thermal anisotropy of urban neighbourhoods: morphological causation. *Remote Sensing*, *8*(2), 108.
- Krayenhoff, E., Jiang, T., Christen, A., Martilli, A., Oke, T., Bailey, B., . . . Crawford, B. (2020). A multi-layer urban canopy meteorological model with trees (BEP-Tree): Street tree impacts on pedestrian-level climate. *Urban Climate*, *32*, 100590.
- Kustas, E. P., Choudhury, B. J., Inoue, Y., Pinter, P. J., Moran, M. S., Jackson, R. D., & Reginato, R. J. (1990). Ground and aircraft infrared observations over a partially-vegetated area. *International Journal of Remote Sensing*, *11*(3), 409 - 427.
- Lagouarde, J.-P., Ballans, H., Moreau, P., Guyon, D., & Coraboeuf, D. (2000). Experimental study of brightness surface temperature angular variations of maritime pine (*pinus pinaster*) stands. *Remote Sensing of Environment*, *72*, 17 - 34.

- Lagouarde, J.-P., Moreau, P., Irvine, M., Bonnefond, J.-M., Voogt, J. A., & Sollicec, F. (2004). Airborne experimental measurements of the angular variations in surface temperature over urban areas: case study of Marseille (France). *Remote Sensing of Environment*, 93, 443 - 462.
- Li, N., & Li, X. (In Press). The impact of building thermal anisotropy on surface urban heat island intensity estimation: An observational case study in Beijing. *IEEE Geoscience and Remote Sensing Letters*.
- Li, Z.-L., Tang, B.-H., Wu, H., Ren, H., Yan, G., Wan, Z., . . . Sobrino, J. A. (2013). Satellite-derived land surface temperature: Current status and perspectives. *131*, 14 - 37.
- Li-Cor. (2020). *LI-200 R Pyranometer*. Retrieved from LI-COR: <https://www.licor.com/env/products/light/pyranometer>
- Luvall, J. C. (1990). Estimation of tropical forest canopy temperatures, thermal response numbers, and evapotranspiration using an aircraft-based thermal sensor. *Photogrammetry Engineering and Remote Sensing*, 56(10), 1393 - 1401.
- MathWorks. (2020). *Contour Properties*. Retrieved from MathWorks: https://www.mathworks.com/help/matlab/ref/matlab.graphics.chart.primitive.contour-properties.html#budgut_-ContourMatrix
- Melexis. (2013). *MLX90614 family*. Retrieved from ACROBOTIC: <https://learn.acrobotic.com/datasheets/MLX90614.pdf>
- Minkina, W., & Dudzik, S. (2009). *Infrared Thermography: Errors and Uncertainties*. Wiley.
- Nichol, J. E. (1998). Visualisation of urban surface temperatures derived from satellite images. *Journal of Applied Meteorology*, 19, 1639 - 1649.
- NOAA/National Centers for Environmental Information. (n.d.). *2018 Local Climatological Data Annual Summary with Comparative Sata*. Retrieved from NOAA: <https://www1.ncdc.noaa.gov/pub/orders/IPS/IPS-D2DDC4AA-73E9-47CD-970B-AA5520CFDCCB.pdf>
- Norman, J. M., Divakarla, M., & Goel, N. S. (1995). Algorithms for extracting information from remote thermal-ir observations of the earth's surface. *Remote Sensing of Environment*, 51, 157 - 168.
- Oke, T. (1987). *Boundary Layer Climates*. Routledge.
- Oke, T., Mills, G., Christen, A., & Voogt, J. (2017). *Urban Climates*. Cambridge University Press.
- OMEGA. (2020). *Infrared Thermometer*. Retrieved from OMEGA a spectris company: <https://assets.omega.com/manuals/M3921.pdf>
- Roth, M., Oke, T., & Emery, E. J. (1989). Satellite-derived urban heat islands from three coastal cities and the utilization of such data in urban climatology. *International Journal of Applied Meteorology*, 10(11), 1699 - 1720.

- Scaramuzza, D., Martinelli, A., & Siegwart, R. (2006). A toolbox for easily calibrating omnidirectional cameras. *Iros*.
- Sensirion. (2015). *Datasheet SHT3x-DIS*. Retrieved from Adafruit: https://cdn-shop.adafruit.com/product-files/2857/Sensirion_Humidity_SHT3x_Datasheet_digital-767294.pdf
- Soux, A., Voogt, J. A., & Oke, T. R. (2004). A Model to Calculate what a Remote Sensor 'Sees' of an Urban Surface . *Boundary-Layer Meteorology*, *111*(1), 109-132.
- Stewart, I. D., & Oke, T. R. (2012). Local climate zones for urban temperature studies. *Bulletin of the American Meteorological Society*, *93*, 1879 - 1900.
- Sugawara, H., & Takamura, T. (2006). Longwave radiation flux from an urban canopy: Evaluation via measurements of directional radiometric temperature. *Remote Sensing of Environment*, *104*, 226 - 237.
- Turcotte, M. (2008). The city/suburb contrast: How to measure it? Canadian social trends. *Statistics Canada Catalogue no. 11-008-XWE*. Retrieved from <https://www150.statcan.gc.ca/n1/pub/11-008-x/2008001/t/10459/4097957-eng.htm>
- Vinnikov, K., Yu, Y., Goldberg, M., Tarpley, D., Romanov, P., Laszlo, I., & Chen, M. (2012). Angular anisotropy of satellite observations of land surface temperature. *Geophysical Research Letters*, *39*(23).
- Voogt, J. (2008). Assessment of an Urban Sensor View Model for thermal anisotropy. *Remote Sensing of Environment*, *112*(2), 482-495.
- Voogt, J. A., & Oke, T. R. (1997). Complete urban surface temperatures. *Journal of Applied Meteorology*, *36*, 1117 - 1132.
- Voogt, J. A., & Oke, T. R. (1998). Radiometric Temperatures of Urban Canyon Walls obtained from Vehicle Traverses. *Theoretical and Applied Climatology*, *60*, 199-217.
- Zhan, W., Chen, Y., Voogt, J., Zou, J., Wang, J., Ma, W., & Liu, W. (2012). Assessment of thermal anisotropy on remote estimation of urban thermal inertia. *Remote Sensing Environment*, *123*, 12 - 24.

Appendix A

A Instrument Characteristics and Lab Tests

A.1 FLIR T650 Lens errors

Imaging lenses are subject to lens errors such as vignetting and optical lens distortions. Lab tests were performed to test for the magnitude of these errors and to determine when a correction was appropriate. Corrections, when needed, are presented in the following sections.

A.1.1 Lens Vignetting

Lens vignetting is the effect of radiation “fall off” at the outer edges of an image due to the longer path lengths between the radiation source area and the periphery of the lens compared to the center. This effect is more severe for wider-angle lenses. (Minkina and Dudzik, 2009).

Temperature fall-off for the $45^\circ \times 34^\circ$ lens used on the FLIR T650 thermal imager was performed by Hilland (2018) using a 2.54 cm thick matt black aluminum plate heated to 80°C and allowed to cool to room temperature within the full frame of the thermal imager. Pixel temperatures were extracted in lines from the middle of the plate to the outer corners and plotted in Figure A.1. The sensor was at room temperature, or $\sim 22^\circ\text{C}$. The magnitude of temperature fall-off is not only dependent on distance of a pixel from the center of the image but also on the temperature difference between the sensor and the target. The larger the temperature difference between the target and the sensor, the larger the magnitude of the vignette distortion. There are some slight variations in the surface of

form straight lines. The software finds the intersection of these squares and can calculate the correction needed to straighten the lines formed by these intersections (Scaramuzza et al., 2006).

As the corrections are for a thermal imager lens, the checkerboard is made of a low-emissivity tape that, when warmed to above room temperature, creates a visible contrast between the tape and the background within thermal images as shown in Figure A.2. This contrast is needed for the software to calculate the intersection of the checkerboard squares. A total of 34 images were used to create correction coefficients. Scaramuzza et al. (2006) suggest a mean projection error of <1 pixels is ideal and the coefficients determined by the software created a mean projection error of 0.1465 pixels which is within an ideal range. These corrections were applied to the CSV temperature files discussed in Section 2.3.1 before they were converted to raster tiff files.

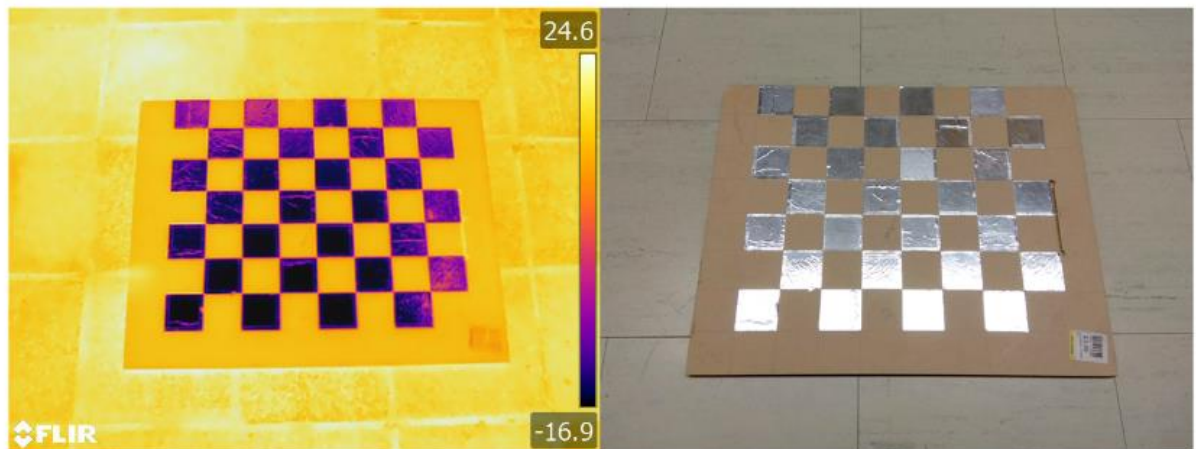


Figure A.2 Thermal image (left) and photo (right) of the checkerboard used to perform the lens distortion calculations. From Hilland (2018).

A.2 Equipment tests

A.2.1 Standardization of FLIR T650 and Apogee SIF-1H1

Temperatures provided by the FLIR T650 were compared to road surface temperatures provided by an Apogee SIF-1H1 infrared radiometer. To test the accuracy of both instruments and ensure the validity of comparing them, a recently purchased and factory calibrated Heitronics KT15.81 radiation pyrometer was compared to both instruments. Lab tests were performed to test the accuracy of the FLIR T650 thermal imager compared to the Heitronics KT15.81 instrument. Further tests were conducted to compare the Apogee SIF-1H1 infrared radiometer to the Heitronics KT15.81. The spectral range of all three instruments is similar and can be found in Table A.1.

Table A.1 Instrument specifications (Heitronics, 2004, FLIR, and Apogee, 2020).

<u>Instrument</u>	<u>Accuracy</u>	<u>Spectral Response</u>
Heitronics KT15.81*	± 0.5 °C	8 - 10 μm
FLIR T650sc	± 1 °C	7.5 - 14 μm
<u>Apogee SIF-1H1</u>	<u>± 0.2 °C</u>	<u>8 - 14 μm</u>

* The only difference between the KT15.81 and KT15.82 instruments are the spectral response

A comparison was performed between the three instruments using a 2.54 cm thick aluminum plate with an emissivity of 0.94 heated to approximately 70°C and placed so that the camera, Heitronics, and Apogee instruments were all viewing the plate at the same location without interfering with the other instruments. The Heitronics was placed 41 cm away from the centre of the plate, which made the IFOV diameter approximately 12 cm. The Apogee SIF-1H1 instrument was positioned 23 cm above the plate at a 10°

angle creating a rectangular IFOV of approximately 28 cm x 11cm. During processing of the FLIR video a polygon was created in the estimated view area of the Heitronics and Apogee IFOV. An average temperature was extracted with this area that could be compared to the other instrument results.

Figure A.3 shows the Heitronics KT15.82 dataset plotted against the FLIR T650sc dataset. The data trend follows the 1:1 line very well, suggesting there is good agreement between the instruments. The largest difference between the FLIR T650sc and the Heitronics KT15.81 is observed for large target temperatures when the difference between plate temperature and air temperature was largest. From the trendline, the FLIR thermal imager appears to slightly overestimate temperatures significantly larger than air temperature and slightly underestimate temperatures below air temperature, however, the largest differences of $\pm 0.4^{\circ}\text{C}$ observed during this test are within the error range of both instruments and so no correction was applied.

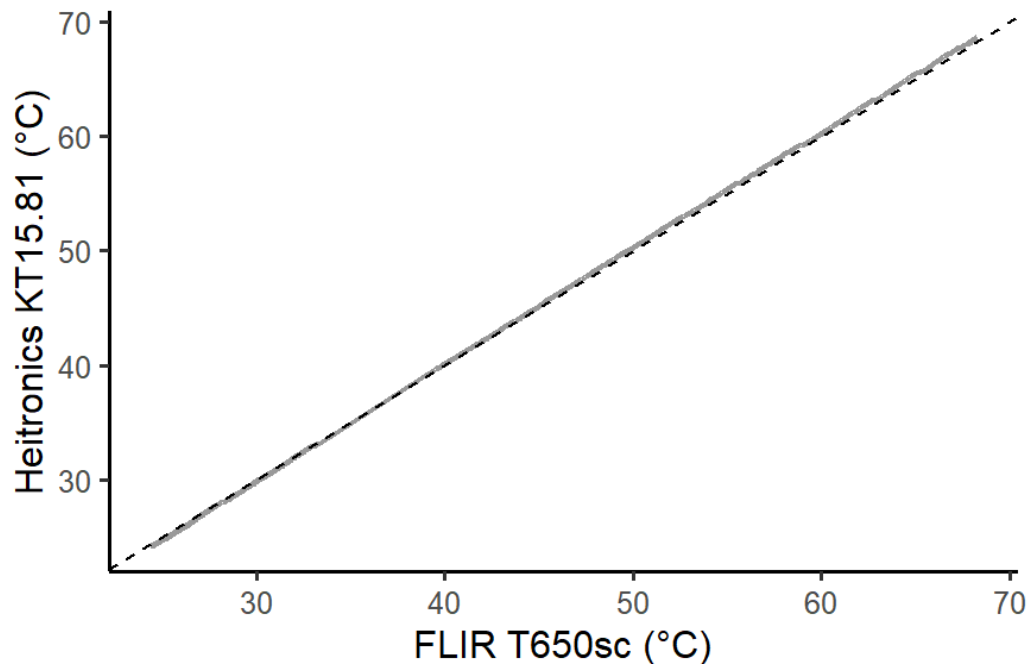


Figure A.3 Comparison between the Heitronics KT15.81 and FLIR T650sc plate temperature results. The dashed black line represents the 1:1 line. The correlation coefficient for this data is 0.99.

The Apogee SIF-1H1 instrument was used to measure road surface temperatures which were compared to atmospherically corrected thermal images to verify the validity of the atmospheric corrections. Figure A.4 shows the results of the plate test for the FLIR T650sc and Apogee SIF-1H1. The Apogee instrument is consistently between 0.3 – 0.6°C larger than the FLIR thermal imager, with the difference decreasing as the plate cooled to room temperature. When the plate was near 70°C there is some noise in the comparison, likely caused by the emissivity of the plate.

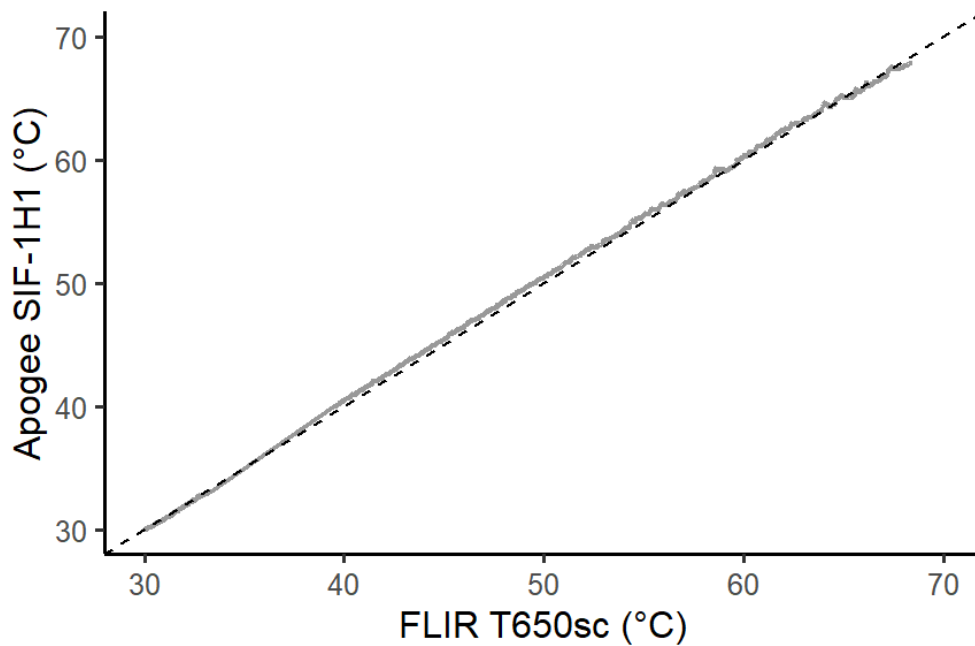


Figure A.4 Comparison between the Apogee SIF-1H1 and FLIR T650sc plate temperature results. The dashed black line represents the 1:1 line. The correlation coefficient for this data is 0.85.

A.3 Optimization of FLIR T650 and Heitronics KT15.82 FOV Overlap

The FLIR T650 thermal imager and Heitronics KT15.82 were positioned to ensure overlap in the FOV of the instruments. To determine the area of overlap for the Heitronics KT15.82 in the thermal images, measurements were taken in the lab to determine an approximate location of the KT15.82 projected IFOV ($\text{IFOV}_{\text{KT15.82}}$) within the thermal images. Tests were then performed using data from flights on 2 separate days to determine the optimal size and position of the $\text{IFOV}_{\text{KT15.82}}$. Five different lines of sight were tested for the center of the $\text{IFOV}_{\text{KT15.82}}$ to optimize the location where the instrument radiometric source area overlap (Figure A.5). Mann-Whitney U-tests were performed between the average brightness temperature within each circular test area for each image corresponding to an off-nadir angle (ONA) and azimuth view direction pair and the Heitronics KT15.82 dataset. The percentage of view directions with p-value scores < 0.05 are shown in Table A.2 to show the performance of each subset IFOV. From the results, the match of source area overlap is very sensitive due to the large spatial variability within the sites and noise from the Heitronics KT15.82 sensor due to the 100ms response rate. This spatial variability is due to the large tree canopies in the Liberty Wells and White Sands sites causing randomly placed cool areas next to very hot impervious surfaces. Due to the sensitivity of the $\text{IFOV}_{\text{KT15.82}}$ location, a larger area was tested at the location of best match for both flights, FOV3. This larger area did not improve the match for the Liberty Wells site, but it did improve the White Sands site match. Based on these results, the location of IFOV3 corresponds best to the Heitronics KT15.82 dataset for both flights and is used for the comparison in Section 3.4.2.



Figure A.5 Sample thermal image from LW12 showing (left) the center points of FOV1 – 5 with FOV1 being the lab determined $IFOV_{KT15.82}$ and (right) FOV6 and FOV7 showing the increase and reduction of FOV3 (the location of best match).

Table A.2 Optimization of thermal imager FLIR T650 and Heitronics KT15.82 instrument comparison. FOV1 is the lab tested IFOV_{KT15.82} representing where the Heitronics KT.82 and FLIR T650 overlap. FOV2 – 5 are similarly sized circles moved 50 pixels to the left, right, above, and below the original IFOV_{KT15.82}. FOV6 –increased the size of the IFOV by 5° for location of best match (highest percentage). Percentages represent the percent of polar plot points (ONA and view azimuth pairs) that are considered similar with $p < 0.05$. Each polar plot point is represented by 10 – 80 thermal images.

Liberty Wells	Percent of ONA and view azimuth pairs with $p < 0.05$
FOV1	67%
FOV2	61%
FOV3	71%
FOV4	61%
FOV5	51%
FOV6	58%
White Sands	
FOV1	63%
FOV2	63%
FOV3	68%
FOV4	63%
FOV5	65%
FOV6	72%

Appendix B

B MODTRAN Sensitivity Tests

MODTRAN 6 allows the user to provide input surface temperatures to generate integrated radiances as well as observer and target positions. For our purposes, the program was set up with the observer height and observation angle specified and the target as a static position. The range of temperatures within each site ranged from below air temperature for shaded surfaces (approximately 20°C for most flights) up to 75°C for very hot surfaces. The airborne sampling method also meant that there was a range of sensor height and off-nadir angles sampled. These variables are continuous between a minimum and maximum range of values however MODTRAN requires discrete values and multiple iterations of the program to simulate multiple sensor orientations. Sensitivity tests were run using a consistent atmosphere to test the step-sizes needed for each of these variables to generate an accurate correction curve while also minimizing MODTRAN iterations. The sensitivity tests for each variable were conducted using MODTRAN's pre-set Mid-latitude Summer atmospheric profile (Kantor and Cole, 1962).

B.1 Surface Temperature

The surface temperature sensitivity test was used to determine how large the step size of input surface temperature could be and still get accurate corrections. Surface temperatures between 15°C and 70°C were input into MODTRAN in 1°C steps and a corrected brightness temperature was calculated over the spectral response of the FLIR imager. The true brightness temperature was plotted against the corrected brightness temperature and a polynomial was determined from the curve of best fit. This was then done again for 5°C, 10°C, and 15°C step sizes. These correction polynomials were applied to a series of temperature values to test the accuracy of the correction polynomial.

Figure B.1 shows the difference in correction when those correction polynomials are used for the longest path lengths tested with a sensor orientation of 45° ONA and a sensor height of 0.6 km above ground level. As step sizing is increased, the difference in correction polynomials increases, introducing more potential error into the atmospheric correction polynomials. The input surface temperature is not particularly sensitive below 10°C however the correction polynomial created using a 15°C step size begins to create large differences compared to the correction polynomial created with a 1°C step size. From this, any step size $\leq 10^\circ\text{C}$ is acceptable.

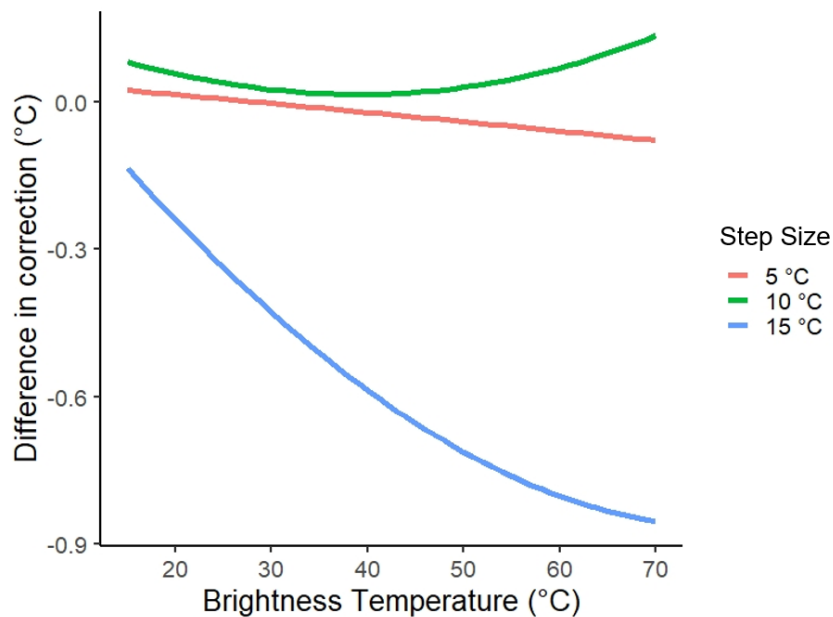


Figure B.1 Comparison of atmospheric correction polynomials for increasing step size to a baseline step size of 1°C. The sensor was oriented at a 45° ONA and 0.6 km above ground level. MODTRAN calculated brightness temperature was plotted against input surface temperature (first at 1°C and then at 5°C, 10°C, and 15°C intervals) and a curve of best fit was applied to create correction polynomials for each step size. These were then applied to a range of pixel temperatures and compared to the smallest step size of 1°C, as the smallest step size is expected to produce the most accurate curve.

B.2 Off-nadir Angle

The off-nadir angles sampled with the Aaronia tilt sensor ranged from 0° - 60° .

MODTRAN sensitivity tests on the ONA needed to be conducted to determine a discrete set of input parameters that could accurately predict the corrections needed for the datasets within a reasonable number of program iterations. For these tests, increasingly larger bin sizes were tested for the target angles of 25° and 45° ONA as well as the sample limits of 5° and 55° ONA. Table B.1 shows a summary of the tests conducted.

The bin range represents the full range of ONA included in the bin with the angle label representing the median of the bin. A bin range of 1° for 45° ONA would be $45^\circ \pm 0.5^\circ$.

The absolute difference is the largest difference between the upper or lower boundary of the bin range and the median value. As expected, the largest errors are observed for longer path lengths and the greatest difference between surface temperature and air temperature. From these tests, the largest error is encountered for very hot surfaces and a bin size of 10° . This error is below $\pm 0.5^\circ\text{C}$, or half of the instrument error of the FLIR thermal imager, except for at 55° ONA where it is still $< 1^\circ\text{C}$. The tilt sensor data was very noisy so considering the uncertainty in tilt sensor results at a fine resolution and the results of this test, 10° ONA was chosen for the ONA bin size.

Table B.1 Differences in atmospheric corrections for different bin sizes of ONA. Bin range is expressed as the full range of ONA with the angle as the median of the bin range. Maximum absolute differences in correction are shown for each bin and are expressed as the largest absolute difference in correction between the upper or lower boundary of the bin and the median value. This test is based on a mid-latitude summer atmospheric profile at a given true brightness temperature and sensor altitude. The largest ONA used in the analysis of these observations is 55° ONA, which was sampled at approximately 0.3 km above ground level. The target angles of 45°, 25°, and nadir (5°) are also examined.

0.3 km				0.6 km			
Height:				Height:			
True Brightness Temperature (°C)	Angle (°)	Bin Range (°)	Maximum Absolute Difference (°C)	True Brightness Temperature (°C)	Angle (°)	Bin Range (°)	Maximum Absolute Difference (°C)
15	45	1	0.01	15	5	1	0.00
15	45	5	0.02	15	5	5	0.00
15	45	10	0.05	15	5	10	0.00
15	55	1	0.01	15	25	1	0.00
15	55	5	0.04	15	25	5	0.01
15	55	10	0.09	15	25	10	0.03
35	45	1	0.01	35	5	1	0.00
35	45	5	0.07	35	5	5	0.00
35	45	10	0.15	35	5	10	0.02
35	55	1	0.02	35	25	1	0.02
35	55	5	0.10	35	25	5	0.04
35	55	10	0.24	35	25	10	0.09
70	45	1	0.09	70	5	1	0.00
70	45	5	0.20	70	5	5	0.01
70	45	10	0.45	70	5	10	0.05
70	55	1	0.14	70	25	1	0.03
70	55	5	0.16	70	25	5	0.12
70	55	10	0.74	70	25	10	0.26

B.3 Sensor Altitude

The sensitivity of our corrections to the changes in flight altitude over the course of the flight were tested to determine a suitable bin size that would minimize program iterations while also reducing the maximum absolute difference between the upper or lower boundary of a bin and the median value. Table B.2 shows a comparison of bin sizes of

100 m, 50 m, and 10 m for 45° and 25° ONA to assess the acceptable bin size. Bins are shown in Table B.2 as the full bin range with the altitude the median of the bin.

Corrections are larger for longer path lengths; however, the maximum absolute difference between bin boundaries and median values is reduced for larger flight heights at the same ONA and input surface temperature.

Table B.2 Differences in atmospheric corrections for different bin sizes of sensor altitude. Bin range is expressed as the full range of altitudes with the angle as the median of the bin range. Maximum absolute differences in correction are shown for each bin and are expressed as the largest absolute difference in correction between the upper or lower boundary of the bin and the median value. This test is based on a mid-latitude summer atmospheric profile at a given true brightness temperature and sensor ONA. The flights typically ranged from 400 to 800 m above the ground with the transition from a target angle of 45° ONA to 25° ONA occurring at approximately 0.5 km above ground level for most flights.

ONA: 45°				ONA: 25°			
True Brightness Temperature (°C)	Altitud e (m)	Bin Rang e (m)	Maximu m Absolute Differenc e (°C)	True Brightness Temperature (°C)	Altitud e (m)	Bin Rang e (m)	Maximu m Absolute Differenc e (°C)
35	400	10	0.02	35	600	10	0.02
35	400	50	0.12	35	600	50	0.09
35	400	100	0.23	35	600	100	0.18
35	500	10	0.02	35	700	10	0.02
35	500	50	0.11	35	700	50	0.08
35	500	100	0.21	35	700	100	0.17
35	600	10	0.02	35	800	10	0.02
35	600	50	0.10	35	800	50	0.08
35	600	100	0.20	35	800	100	0.16
70	400	10	0.07	70	600	10	0.05
70	400	50	0.33	70	600	50	0.22
70	400	100	0.64	70	600	100	0.48
70	500	10	0.06	70	700	10	0.04
70	500	50	0.29	70	700	50	0.20
70	500	100	0.57	70	700	100	0.44
70	600	10	0.05	70	800	10	0.04
70	600	50	0.26	70	800	50	0.19
70	600	100	0.52	70	800	100	0.40

B.4 Humidity

The sensitivity of the atmosphere in the Salt Lake City valley to changes in humidity was tested to determine the sensitivity of our atmospheric corrections to differences in atmospheric profile inputs. The relative humidity was increased for each layer of the atmosphere between the ground and sensor in steps of 5%. Figure B.2 shows the results of this test on the atmospheric profile for 15 July 2018 at solar noon using a microwave radiometer generated atmospheric profile. The atmospheric profiles of 12 July and 19 July 2018 had similar air temperature and water content trends, so it is expected that the results apply to all study days. The atmosphere in the Salt Lake City valley was very dry, ~20% relative humidity each day with a fluctuation of up to 5 - 10% reported between different sensors across the valley provided by the MesoWest network. Relative humidity fluctuated by close to 5% between different neighbourhoods. MODTRAN was run with multiple atmospheric profiles with increasing relative humidity to test the sensitivity of the atmosphere over SLC to observed variability in relative humidity. Multiple true brightness temperatures were tested to determine the sensitivity of the atmospheric corrections to changes in relative humidity for a large range of brightness temperatures. From the Figure, changes of +/- 0.5°C were found for the expected range of ~5% relative humidity fluctuation. This is within the error range of the thermal imager and infrared pyrometer used in this thesis. The changes in atmospheric correction exceed 1°C for increases in relative humidity of 10% or larger for very hot surface temperatures indicating that for most surface temperatures (<70°C surface temperatures) the sensitivity of our atmospheric corrections to observed variability in relative humidity is low.

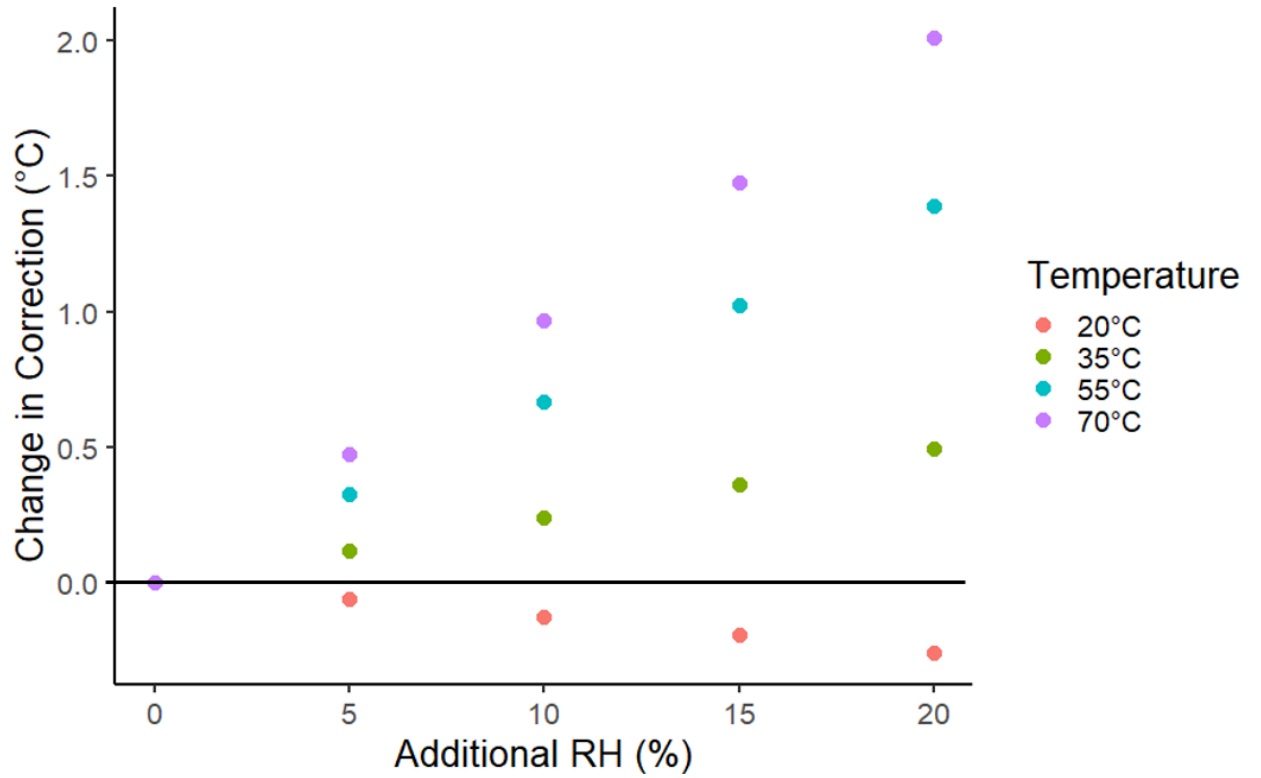


Figure B.2 Change in atmospheric corrections with increasing relative humidity (RH) for the atmospheric profile of 15 July 2018 at solar noon (Flight WhS12). Temperatures used are true brightness temperatures for surfaces such as shaded, irrigated grass (20°C), shaded road or roof (35°C), sunlit road (55°C), and sunlit roof (70°C).

Appendix C

C Supplemental Figures

Figures C.1, C.2, and C.3 show component temperatures extracted from thermal images and averaged over 5-minute time steps.

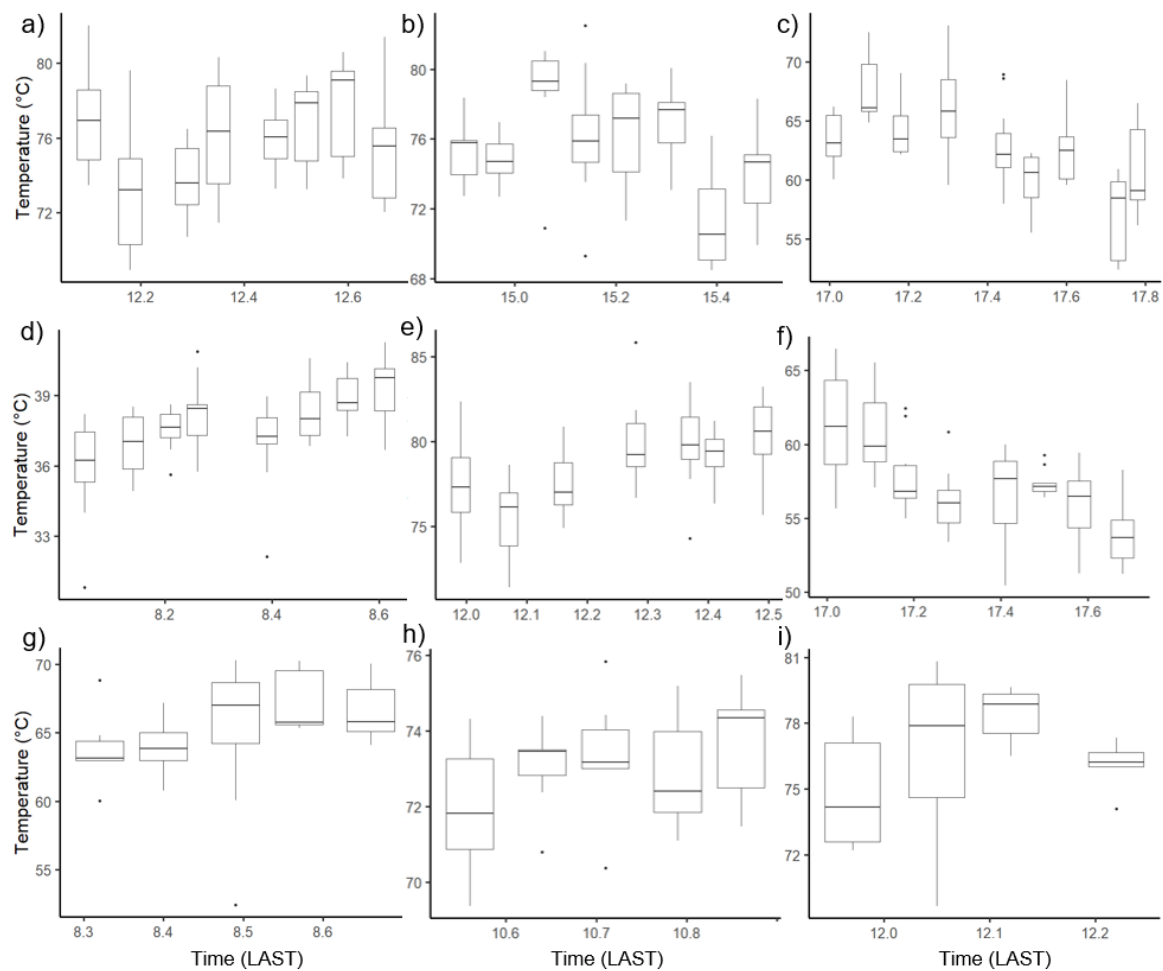


Figure C.1 Sunlit roof temperatures extracted from atmospherically corrected helicopter thermal images taken 5-minutes apart for the duration of each flight for (a) LW12, (b)LW15, (c) LW17, (d)WhS8, (e)WhS12, (f)WhS17, (g)WS8, (h)WS10, and (i)WS12. Time uses decimal hours and is in local apparent solar time. Note that the duration of

WS8, WS10, and WS12 are about half the length of the other flights. Box and whisker meanings are the same as Figure 2.18.

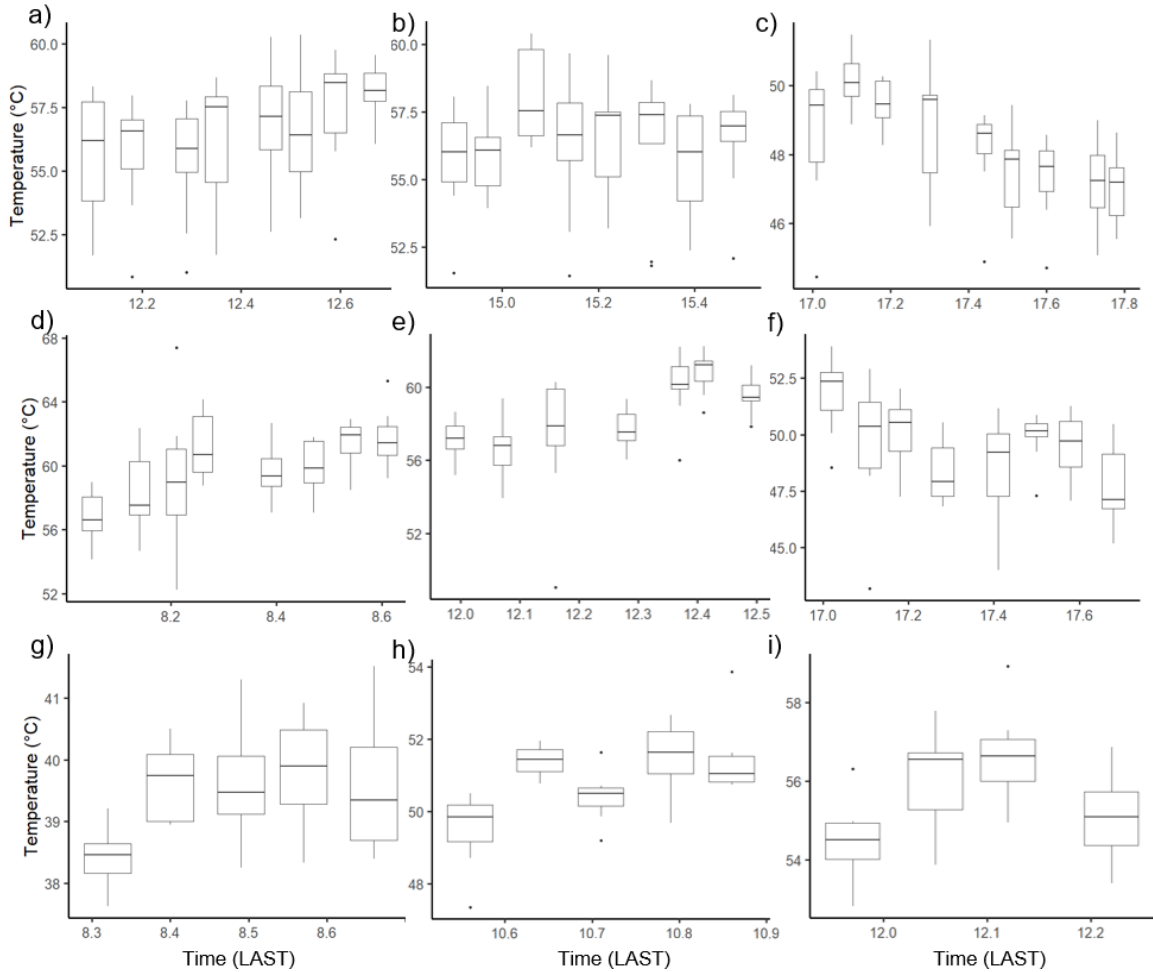


Figure C.2 Sunlit roof temperatures extracted from atmospherically corrected helicopter thermal images taken 5-minutes apart for the duration of each flight for (a) LW12, (b) LW15, (c) LW17, (d) WhS8, (e) WhS12, (f) WhS17, (g) WS8, (h) WS10, and (i) WS12. Time uses decimal hours and is in local apparent solar time. Note that the duration of WS8, WS10, and WS12 are about half the length of the other flights. Box and whisker meanings are the same as Figure 2.18.

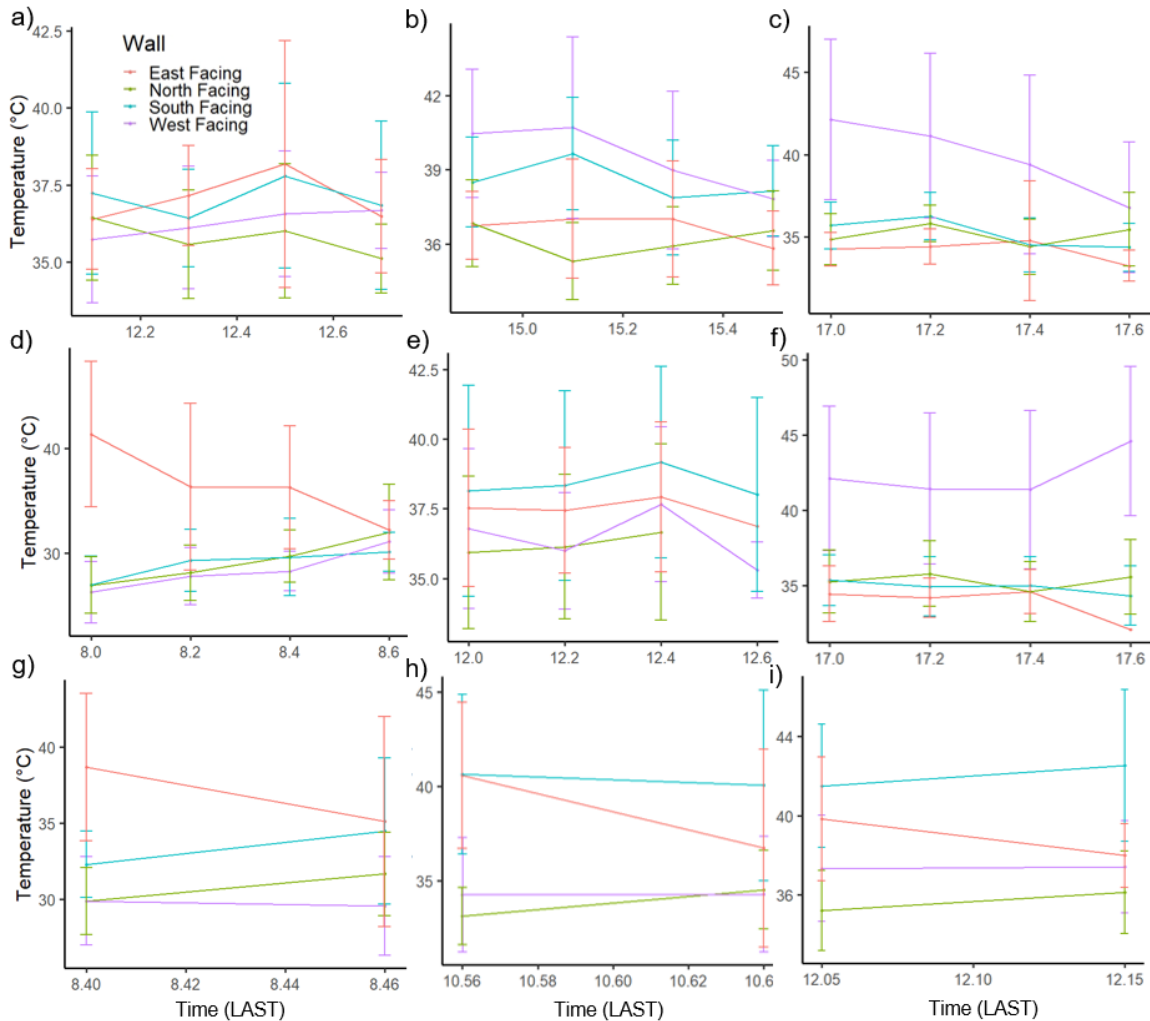


Figure C.3 Wall temperatures extracted from truck thermal images taken 5-minutes apart for the duration of each flight for (a) LW12, (b) LW15, (c) LW17, (d) WhS8, (e) WhS12, (f) WhS17, (g) WS8, (h) WS10, and (i) WS12. Error bars indicate the standard deviation over the 5-minute averaged temperature. Time is in decimal hours and uses local apparent solar time. Note that the duration of WS8, WS10, and WS12 are about half the length of the other flights. Straight lines between points are used to help visualization and are not indicative of the variability in data between data points.

Figures C.4 to C.12 show results of modelled temporal change in DBT for each flight generated using SUMVeg coupled with TUF3D. The plots show the initial modelled polar plot and then the modelled change in that initial polar plot in 15-minute time steps.

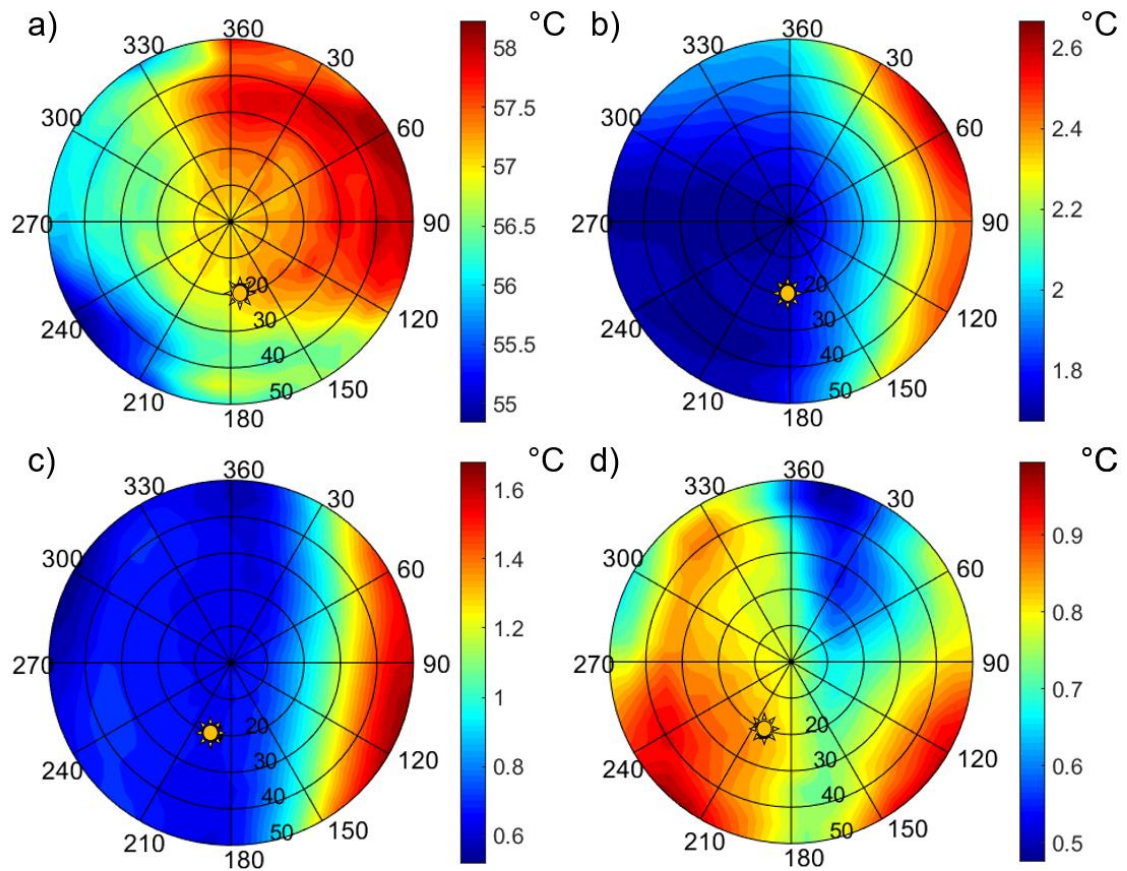


Figure C.4 Modelled LW12 (a) DBT for start of the traverse (t_1) and the temporal changes in these DBT for (b) $t_1 - t_2$, (c) $t_1 - t_3$, and (d) $t_1 - t_4$ where t_i is the modelled DBT in 15-minute time steps from t_1 to a total of 45-minutes after the start of the traverse (t_4). The location of the sun is indicated by a sun symbol on the polar plot.

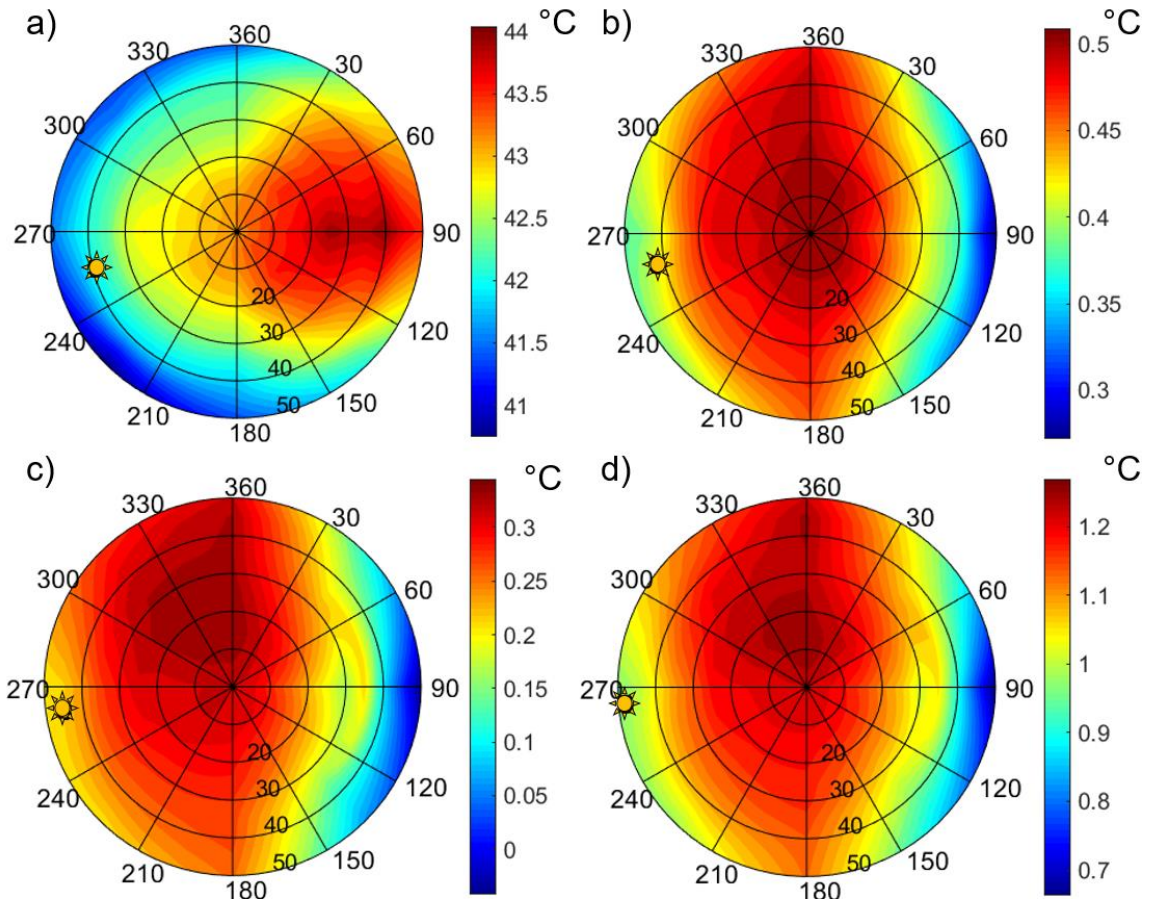


Figure C.5 Modelled LW15 (a) DBT for start of the traverse (t_1) and the temporal changes in these DBT for (b) $t_1 - t_2$, (c) $t_1 - t_3$, and (d) $t_1 - t_4$ where t_i is the modelled DBT in 15-minute time steps from t_1 to a total of 45-minutes after the start of the traverse (t_4). The location of the sun is indicated by a sun symbol on the polar plot.

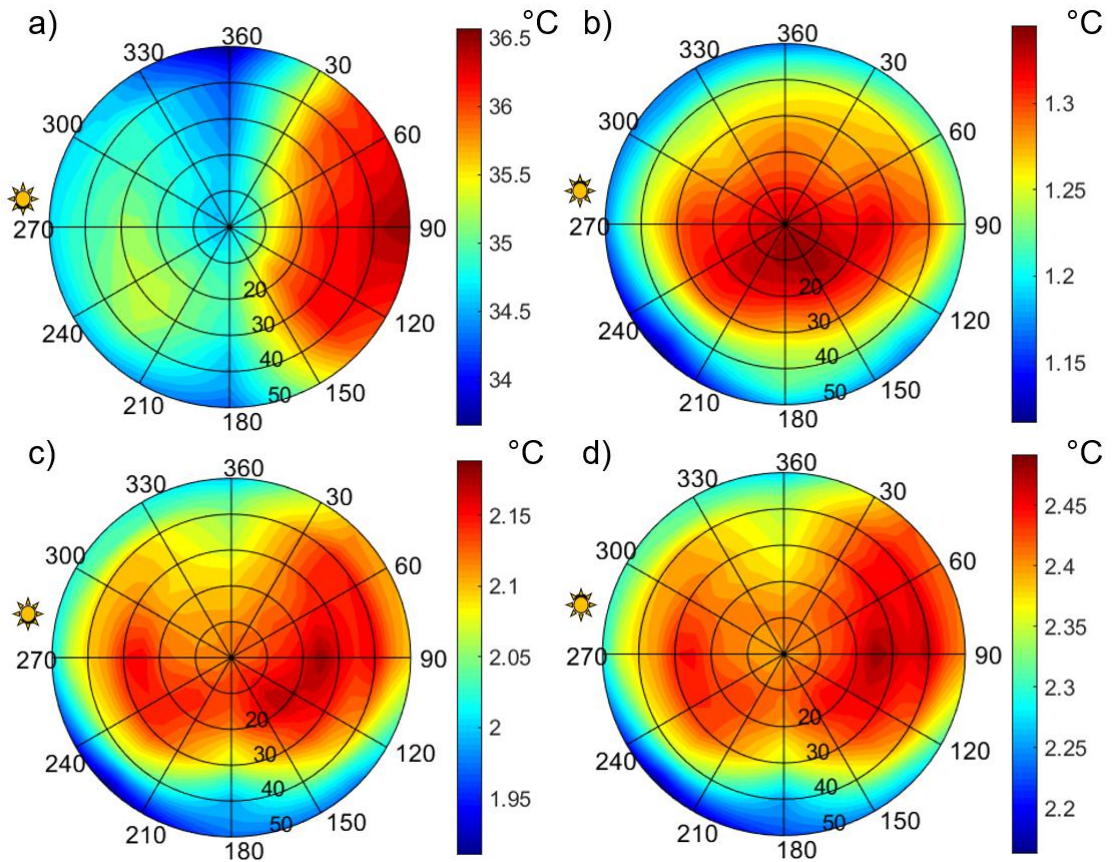


Figure C.6 Modelled LW17 (a) DBT for start of the traverse (t_1) and the temporal changes in these DBT for (b) $t_1 - t_2$, (c) $t_1 - t_3$, and (d) $t_1 - t_4$ where t_i is the modelled DBT in 15-minute time steps from t_1 to a total of 45-minutes after the start of the traverse (t_4). The location of the sun is indicated by a sun symbol on the polar plot.

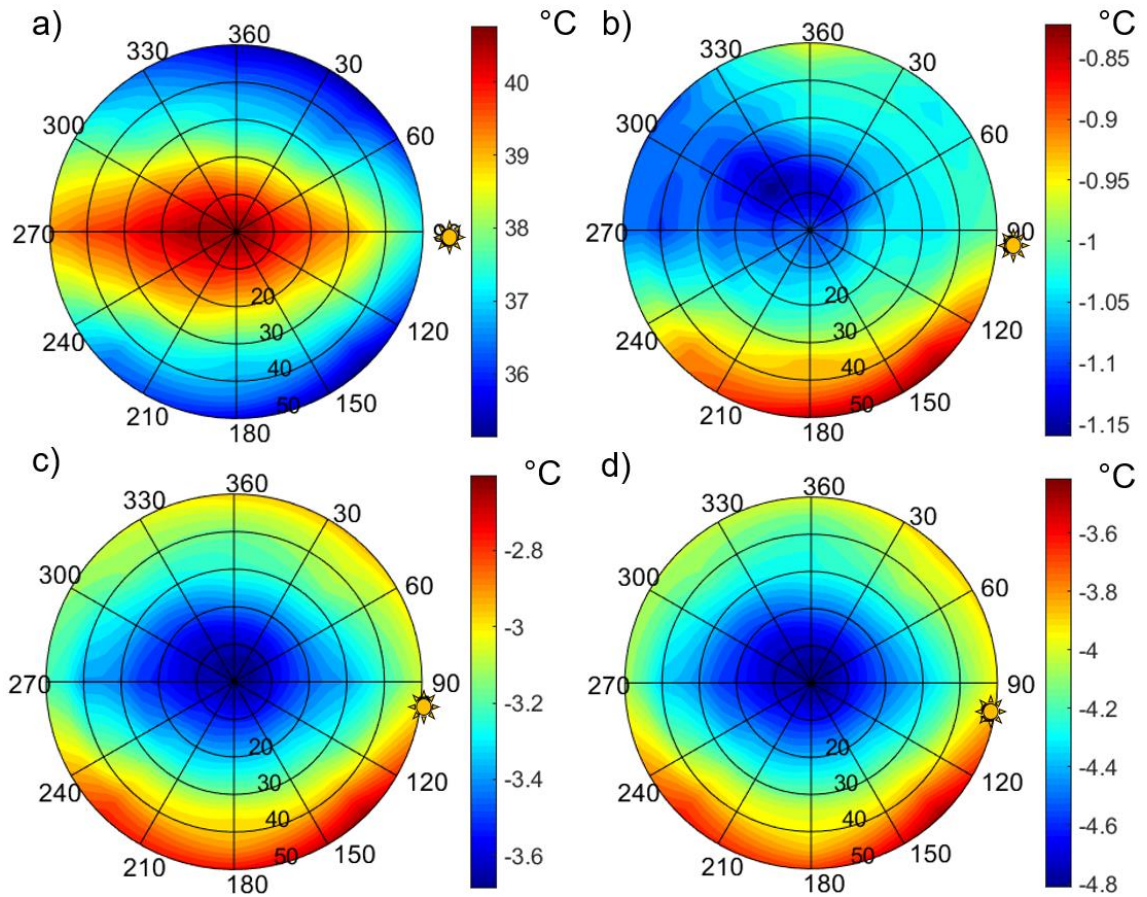


Figure C.7 Modelled WhS8 (a) DBT for start of the traverse (t_1) and the temporal changes in these DBT for (b) $t_1 - t_2$, (c) $t_1 - t_3$, and (d) $t_1 - t_4$ where t_i is the modelled DBT in 15-minute time steps from t_1 to a total of 45-minutes after the start of the traverse (t_4). The location of the sun is indicated by a sun symbol on the polar plot.

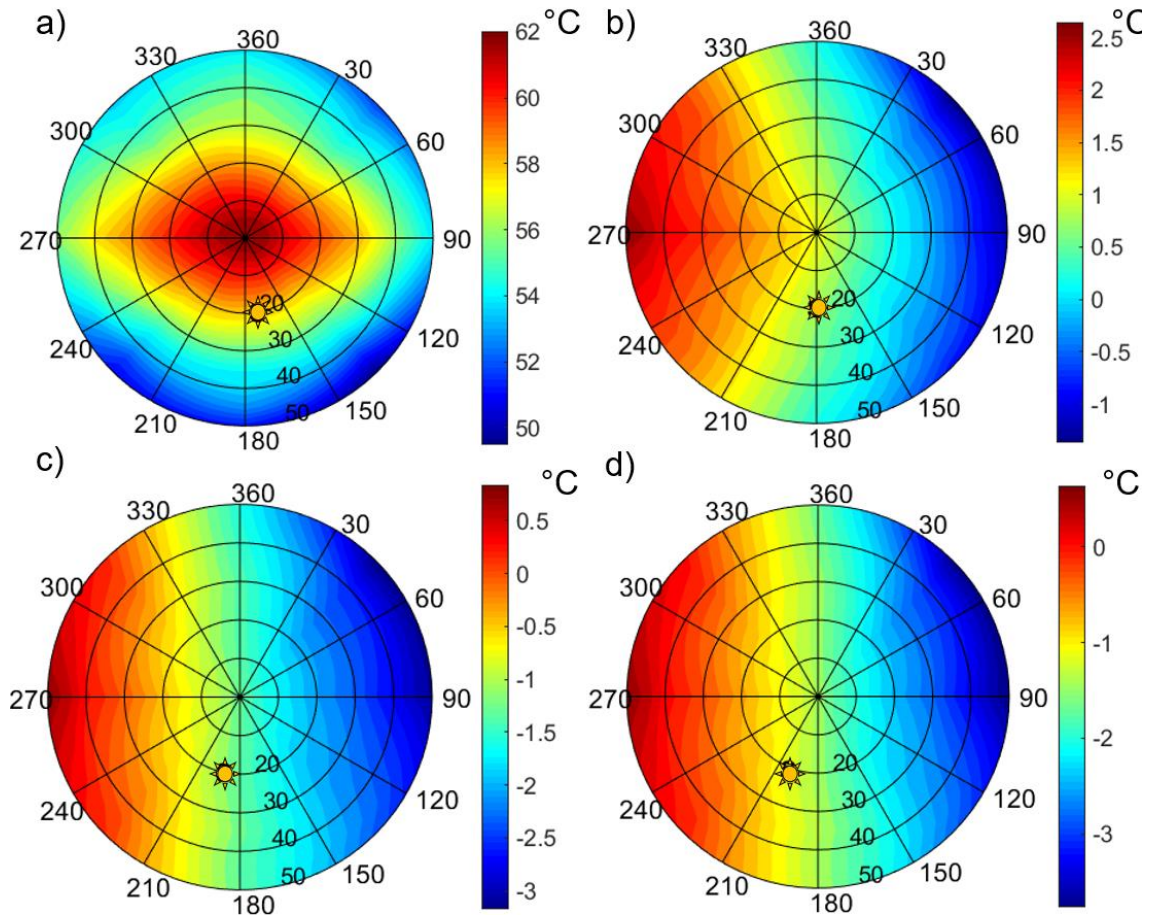


Figure C.8 Modelled WhS12 (a) DBT for start of the traverse (t_1) and the temporal changes in these DBT for (b) $t_1 - t_2$, (c) $t_1 - t_3$, and (d) $t_1 - t_4$ where t_i is the modelled DBT in 15-minute time steps from t_1 to a total of 45-minutes after the start of the traverse (t_4). The location of the sun is indicated by a sun symbol on the polar plot.

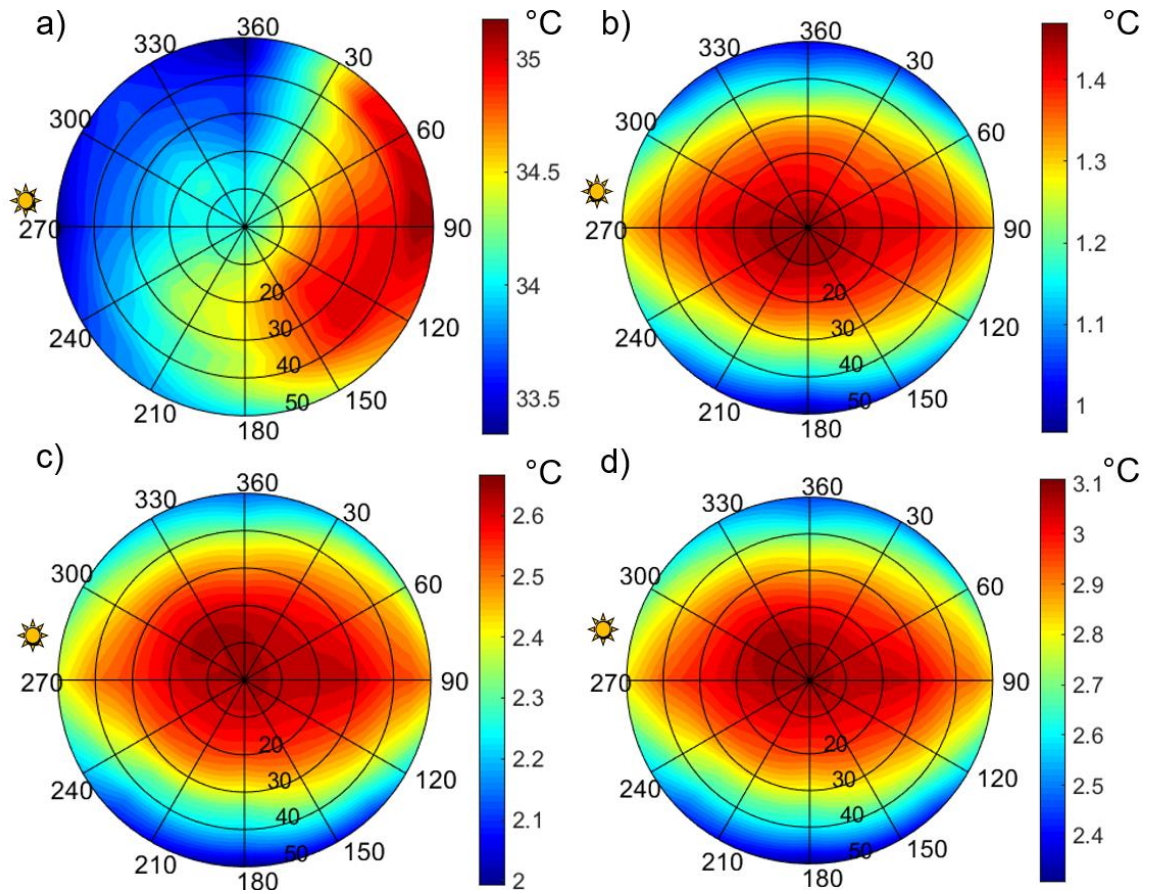


Figure C.9 Modelled WhS17 (a) DBT for start of the traverse (t_1) and the temporal changes in these DBT for (b) $t_1 - t_2$, (c) $t_1 - t_3$, and (d) $t_1 - t_4$ where t_i is the modelled DBT in 15-minute time steps from t_1 to a total of 45-minutes after the start of the traverse (t_4). The location of the sun is indicated by a sun symbol on the polar plot.

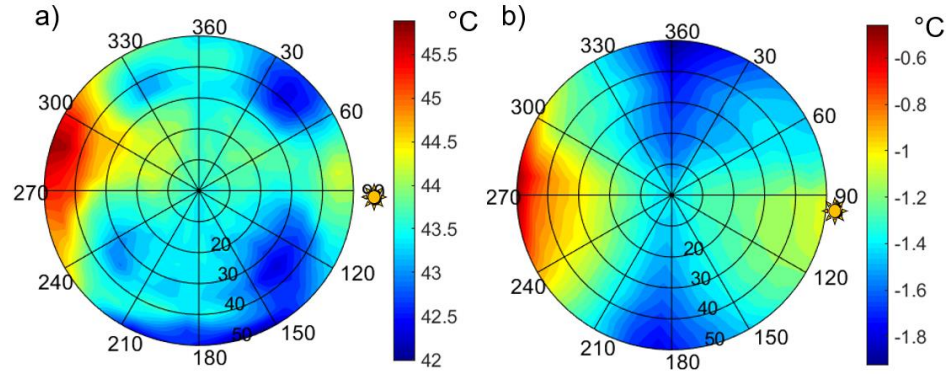


Figure C.10 Modelled WS8 (a) DBT for start of the traverse (t_1) and the temporal changes in these DBT for (b) $t_1 - t_2$ where t_2 is the modelled DBT 15-minutes after the start of the traverse. The location of the sun is indicated by a sun symbol on the polar plot.

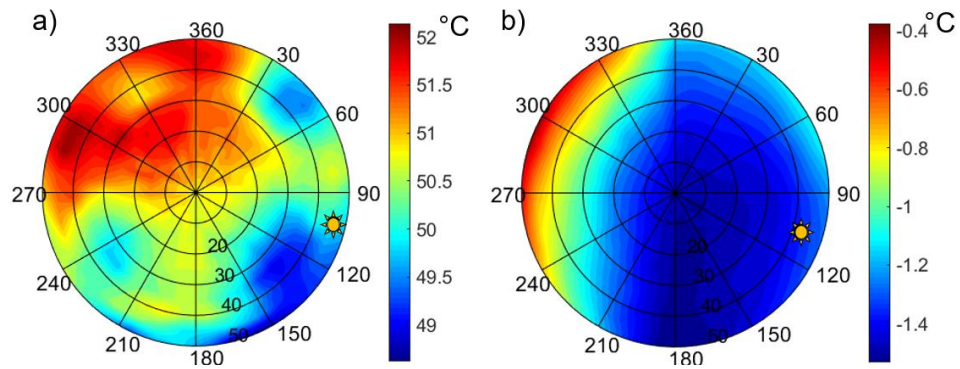


Figure C.11 Modelled WS10 (a) DBT for start of the traverse (t_1) and the temporal changes in these DBT for (b) $t_1 - t_2$ where t_2 is the modelled DBT 15-minutes after the start of the traverse. The location of the sun is indicated by a sun symbol on the polar plot.

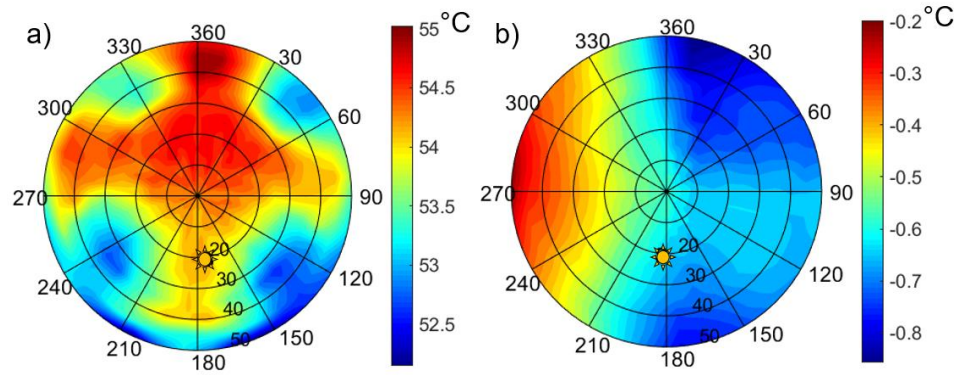


Figure C.12 Modelled WS12 (a) DBT for start of the traverse (t_1) and the temporal changes in these DBT for (b) $t_1 - t_2$ where t_2 is the modelled DBT 15-minutes after the start of the traverse. The location of the sun is indicated by a sun symbol on the polar plot.

Figures C.13 and C.14 depict the polar plots created with limited data points for WhS8 and WhS12 respectively.

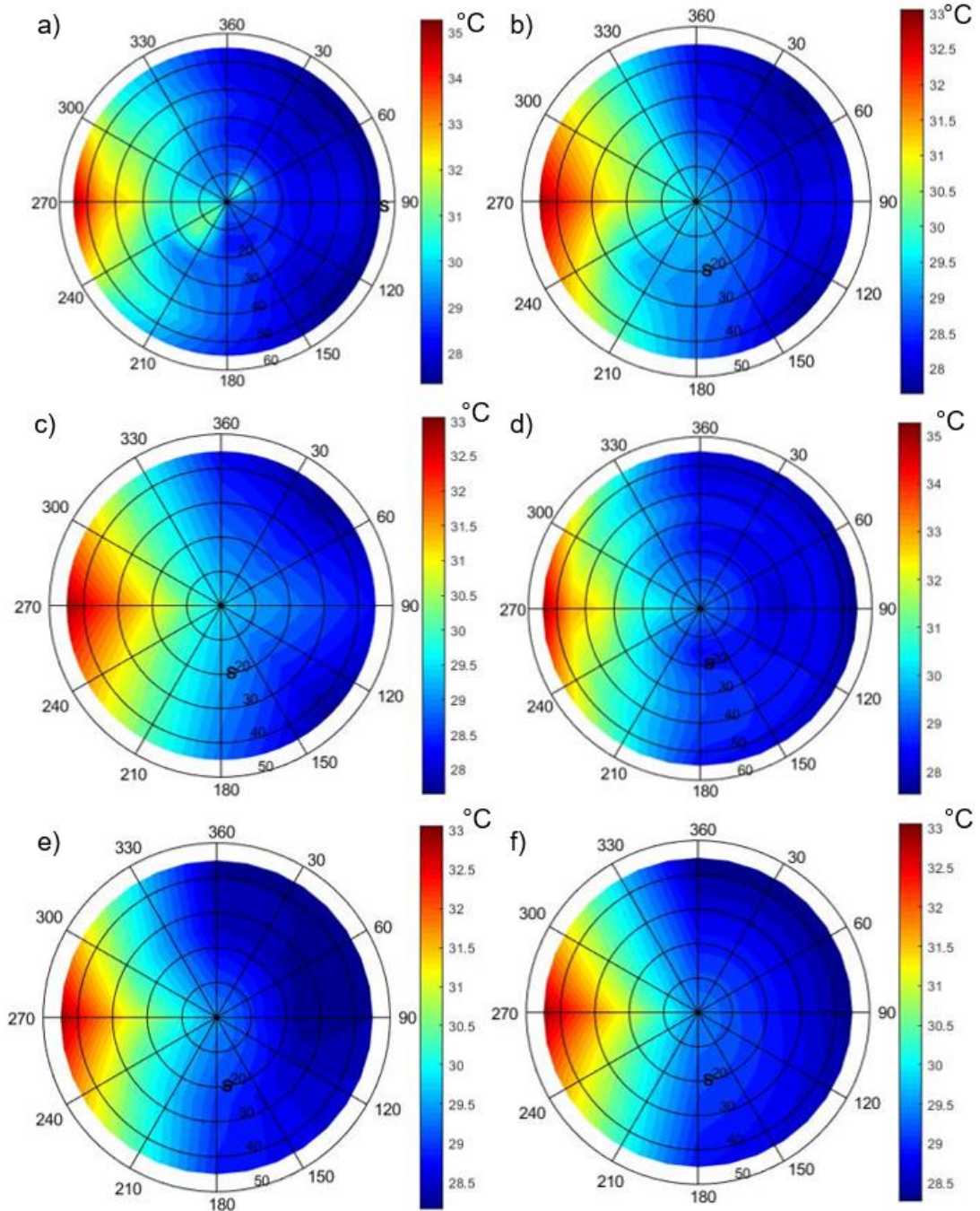


Figure C.13 Polar plots using limited number of data points for WhS8. (a) Complete dataset, (b) test 1, (c) test 2, (d) test 3, (e) test 4, and (f) test 5. The number and location of points used for each test are the same as Figure 4.2.

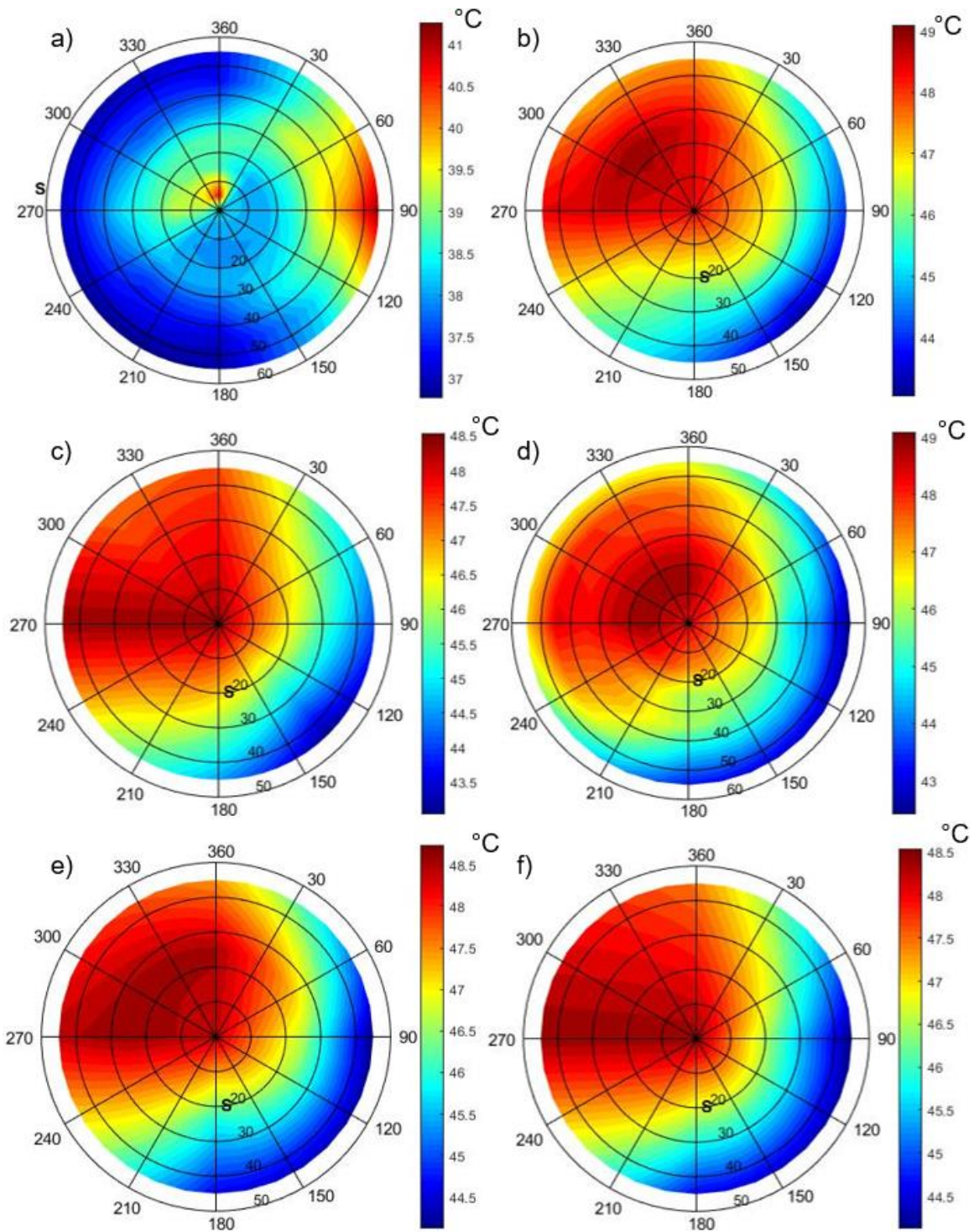


Figure C.14 Polar plots using limited number of data points for WhS12. (a) Complete dataset, (b) test 1, (c) test 2, (d) test 3, (e) test 4, and (f) test 5. The number and location of points used for each test are the same as Figure 4.2.

Curriculum Vitae

Name: Samantha Claessens

Post-secondary Education and Degrees: York University
Toronto, Ontario, Canada
2012-2017 B.Sc.

The University of Western Ontario
London, Ontario, Canada
2017-2020 M.Sc.

Honours and Awards: Brian Luckman Award for Physical Geography Graduate in Year 2 – 4 demonstrating academic achievement in the previous year; Department of Geography, The University of Western Ontario 2019

American Meteorology Student Paper Presentation Award; 15th Symposium on the Urban Environment
Jan. 2020

Related Work Experience Teaching Assistant
The University of Western Ontario
2017 – 2020

Graduate Research Assistant
Surface Climates Lab, The University of Western Ontario
2017 – 2019

Presentations:

Samantha Claessens, J.A. Voogt, Airborne Observations of Thermal Anisotropy from Urban Residential Neighbourhoods in Salt Lake City. *Canadian Association of Geographers – Ontario Division*, Guelph, ON, Canada. October 2019. Oral.

Samantha Claessens, J.A. Voogt. Airborne Observations of Thermal Anisotropy from Urban Residential Neighbourhoods in Salt Lake City. *American Meteorological Society 15th Symposium on the Urban Environment*, Boston, MA, USA. January 2020. Oral. (Winner of Student Presentation Award)